Title
Attosecond X-Ray Pulses for Molecular Electronic Dynamics

Author
Abel, Mark Joseph

Publication Date
2010

Peer reviewed|Thesis/dissertation

Attosecond X-Ray Pulses for Molecular Electronic Dynamics

by

Mark Joseph Abel

A dissertation submitted in partial satisfaction of the
requirements for the degree of
Doctor of Philosophy

in

Chemistry

in the

GRADUATE DIVISION
of the
UNIVERSITY OF CALIFORNIA, BERKELEY

Committee in charge:
Professor Daniel M. Neumark, Chair
Professor Stephen R. Leone
Professor Roger Falcone

Spring 2010

Attosecond X-Ray Pulses for Molecular Electronic Dynamics

Abstract

Attosecond X-Ray Pulses for Molecular Electronic Dynamics

by

Mark Joseph Abel
Doctor of Philosophy in Chemistry

University of California, Berkeley

Professor Daniel M. Neumark, Chair

Attosecond pulses are opening a wide new field on the border of chemistry and physics. They offer the opportunity to initiate and probe electronic rearrangement of atoms, molecules, solids and clusters on the natural timescale of the electron motion. This thesis is about making and measuring attosecond pulses, with the ultimate goal of applying attosecond spectroscopy to molecules. In chapter 1, attosecond spectroscopy is reviewed in general. The applications of attosecond pulses to atoms and molecules, including successful experiments and theoretical predictions, are discussed. In chapter 2, techniques for making and measuring attosecond radiation are presented. This chapter focuses on high harmonic generation from tabletop laser sources, since synchrotron- and free-electron laser-based techniques are not yet experimentally demonstrated. Chapters 3 and 4 discuss in detail the laboratory setup for attosecond pulse generation, including the laser source, optical diagnostics, and attosecond delay line. The attosecond control of free electron motion with few-cycle laser pulses is presented in chapter 5. There, the carrier-envelope phase (CEP), and thus the attosecond temporal evolution of the laser field, leads to quantum interferences between free electron wavefunctions and lends control over the direction of electron emission. Attosecond pulse production is achieved in chapter 6 by gating harmonic generation on the leading edge of the driving laser pulse. The gate mechanism is shown to rely on the macroscopic ionization of the harmonic generation medium. This final chapter also demonstrates a new technique for assessing attosecond pulse temporal structure based on the inversion of the driving laser field in the laboratory frame of reference, called CEP-scanning.

To the people who encouraged me to start this project, and then to finish it:
Ken Houle, Joe Nibler, Mark Hollingsworth, Glenn Evans,
and most of all to Triffid.

Contents

List of Figures

Acknowledgements

This thesis is the culmination of many years' work, none of which would have been possible without the kind support of scientific colleagues and the technical expertise many members of the college of chemistry and LBL support staff.

I am especially indebted to Thomas Pfeifer, Lukas Gallmann, Daniel Strasser, and Zhi-Heng Loh for their contributions of scientific expertise.

Jason Jones and Jun Ye designed, built, and installed the carrier-envelope phase locking electronics on the laser system.

Eric Granlund, Phil Simon, and Andrew Mei made one-off parts for me, put up with my poor drafting skills, and taught me the basics of machining, for which I am extremely grateful.

Yanwei Liu, Andy Aquila, Michael Hofstetter, and Ulf Kleineberg made all the reflective x-ray optics used in experiments. Without their help, this work would literally not exist.

Adam Bradford, Michelle Haskins, and Kathleen Fowler made dealing with the Univsersity and LBL easy.

The project was financially supported by a MURI program from the Air Force Office of Scientific Research, contract No. FA9550-04-1-0242. Portions of the laboratory were paid for by the Director, Office Of Science, Office of Basic Energy Sciences, of the U.S. Department of Energy under contract DE-AC02-05CH11231.

Finally, many thanks to Steve and Dan, who are always right–even if their guidance was sometimes hard for me to take.

Chapter 1

Introduction to Attosecond Science

1.1 Introduction

In 1995, Ahmed Zewail won the Nobel prize in chemistry for femtosecond spectroscopy[1], which provided for the first time a direct probe of nuclear motions on their natural timescale. Instead of inferring ultrafast dynamics of molecules from time-averaged measurements, the course of atomic motion became directly accessible through a host of techniques[2]–transient absorption, light scattering, photoelectron spectroscopy, electron diffraction, and more.

The advent of high harmonic generation (HHG), which allowed femtosecond duration extreme ultraviolet pulses (10-100 eV, for references see chapter 2), extended femtochemistry to core levels of atoms and molecules[3–6].

Until recently, achieving electronic spectroscopy on the natural timescale of electron motion was a dream. Indeed, the idea that electrons are "fast" has been enshrined in chemistry for years as the Born-Oppenheimer approximation. Ultimately, this has to do with the small mass of the electron, which makes the level spacings between quantum mechanical bound states quite large–on the order of electron-volts. Molecular electronic level spacings are generally much larger than vibrational spacings, which are typically a fraction of an eV, despite the larger spatial extent of the delocalized valence electronic wavefunction.

How does the electronic wavefunction change with time? This is a central question of attoscience, and quite an interesting question too, since on a fundamental level it is electrons that drive processes from chemical bonding to solar energy conversion. From a more fundamental perspective, how can we understand the collective motions of many-electron systems? This might seem like a trivial question since of course we have the Schrödinger equation to tell us how quantum mechanical systems behave, but in reality there is an unexpected richness to be studied. It is perhaps useful to draw a parallel to the solar system, where multi-body gravitational effects intrinsic—but buried—in Newton's laws lead to gaps in Saturn's rings (figure 1.1), stabilizing and destabilizing resonances between the orbits of heavenly bodies, Lagrange points, and many other intriguing phenomena.

So what are the intrinsic but buried behaviors of electrons and how do these influence chemical properties like reactivity or the fates of excited molecules? It is a question that we are now in a position to answer thanks to the unlikely help of strong-field physics[7], which asks what happens when atoms are exposed to external electric fields so strong as to rival

Figure 1.1: **Gaps in Saturn's rings.** Caused by multibody gravitational interactions between Saturn, its moons, and the rocks and dust which make up the rings, these gaps are a pretty example of the kind of unexpected physics that can result from from simple governing equations.

their own internal ones. These strong fields are so large that they drive significant portions of the electronic population to motion on a sub-optical-cycle, i.e. attosecond, timescale[8]. In turn, the electron motion in the light field creates a dipole oscillating at extremely high frequencies. This is called high harmonic generation (figure 1.2), and it is the basis for attosecond science since it can produce exceedingly large bandwidths of coherent x-ray light. There are other promising approaches to attosecond light pulse production like free electron lasers[9, 10], but none has successfully generated an attosecond pulse yet.

If attosecond pulse production is quite challenging, then attosecond metrology is even more difficult. The main complication is that there are as yet no isolated attosecond sources that are powerful enough to drive multiphoton processes (but nonlinear interactions have been driven by attosecond pulse trains[11–15]). As a result, self-referencing characterization of attosecond x-ray pulses is not possible and cross correlation must be used instead. Nevertheless, there are several techniques of attosecond metrology that allow measurement of the temporal characteristics of pulse trains and of isolated pulses, all of which rely on comparing the attosecond pulse to the driving light pulse that was used to generate it[8, 16–18].

Once attosecond pulses are produced and measured, they can be used to study the ultrafast motions of electrons and nuclei. This chapter will review the successful experimental use of attosecond pulses and also proposed techniques that have yet to be experimentally implemented.

1.2 Applications

1.2.1 Experiments using streaking

The attosecond emission of Auger electrons from krypton atoms was measured in 2002 using an attosecond pulse[19]. The Auger effect, shown in figure 1.3 is a common decay pathway of ions with holes in their inner valence or core levels. Since they have many electrons in higher-energy orbitals, these electrons race to fill the low-energy hole. But the energy they give up in the process has to go somewhere–it is transferred to another electron

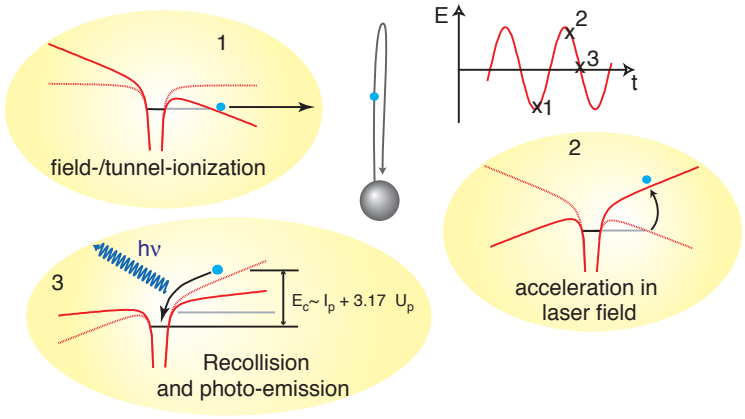

Figure 1.2: **Harmonic generation in a strong field.** Tunnel ionization of an electron by a strong laser field is followed by propagation of the wavefunction through the continuum, where the electron is turned around by the evolving laser field. The electron may recombine with the parent ion to release high-order harmonics of the laser field.

in the cloud, which is then ejected from the atom. The atom ends up with a double positive charge, and two electrons fly off through the vacuum despite the absorption of only one photon. The perturbation that couples the initial high energy ion state with the lower energy doubly-charged state is the Coulomb repulsion between electrons, and so Auger decay is in principle sensitive to electronic correlation: the Auger lifetime is a measure of how strongly electrons "talk" to each other in the atom or molecule.

In fact electrons talk very strongly–typical Auger lifetimes are on the order of a few femtoseconds[20]. (Not to mention that the correction to the He atom ground state energy due to electro-electron interaction is tens of eV!) So in 2002 the direct measurement of an Auger lifetime in the time domain was a huge breakthrough for attosecond science. The experiment was simple: an attosecond pulse ionized Kr atoms and secondary Auger electrons were then ejected from the resulting ions. The Auger electrons were then subjected to a visible laser pulse with which they could interact in a free-free transition (figure 1.4. If the laser light was present while the Auger electron was being born, it could emit a photon into the laser field, arriving at the detector more slowly or quickly, depending on the electron emission time. If the laser was too late, coming long after the Auger lifetime, there was no modification of the Auger electron energy. The decay was measured to be extremely rapid, with a lifetime of only 8 fs[19].

Allowing free electrons to interact with a strong laser field is called "streaking" because of its analogy to the picosecond and nanosecond streak cameras commonly used in x-ray research. It currently forms the basis for attosecond metrology, discussed in detail in section 2.3. But the streaking technique has also been used successfully to study electron emission from metal surfaces[21], where electron emission times vary with the position of the electron

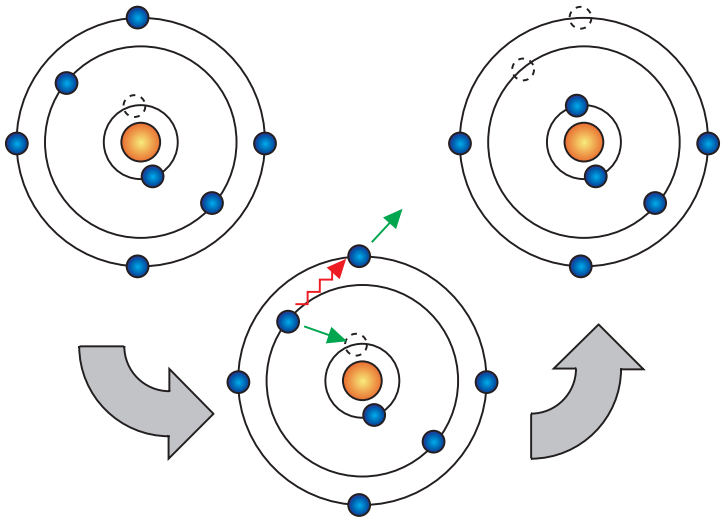

Figure 1.3: **Auger decay.** When an atom or molecule has a core hole, a higher-energy electron can fall to fill it, donating its energy to yet a third electron. This third electron is ejected into the continuum, leaving a doubly-charged ion behind.

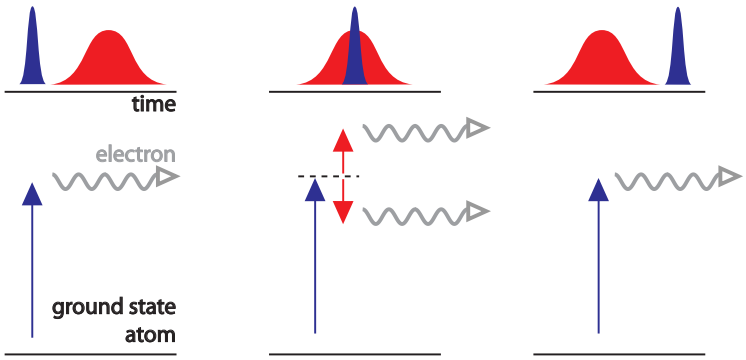

Figure 1.4: **Attosecond measurement of Auger lifetime.** An attosecond pulse stimulates an atom to release an auger electron. If the attosecond pulse is overlapped in time with a strong visible field, the field can exchange energy with the auger electron, leading to different electron kinetic energies. Before the auger decay, or after the decay is over, the infrared field does nothing.

in the metal band structure. The initial explanation for this effect was that the speed of the electrons in the crystal, as well as their escape depth, change with energy and therefore the time at which the electrons emerge into the continuum and begin to interact with the laser field depends on their position in the band structure. However, theoretical work[22–24] following the initial experimental report has opened a debate as to the meaning of the data which is not resolved yet. The time delay between emission from the different bands has been explained by interferences between core-level electrons from neighboring atoms, the group velocity of the bound electrons before interaction with the attosecond pulse, penetration of the streaking field into the first few monolayers of the metal target, and electron-electron scattering in the metal have all been discussed as they pertain to the experimental results, but there does not seem to be a consensus as to the relative importance of these effects for attosecond experiments on metals.

Streaking is in fact not limited to the use of a laser field; it can also be induced by plasmon fields[25, 26]. In that case, a weak laser field can excite a strong plasmon field, which in turn streaks attosecond electron emission from the nanoparticle. This technique has been proposed as a route to the study of plasmon dynamics in real time and also for the implementation of an attosecond photoelectron emission microscope (PEEM)[25], but so far streaking of electrons by a plasmon field has not been experimentally demonstrated.

1.2.2 Attosecond transient absorption

If the electrons under study do not end up in the continuum, streaking is useless. However, the extreme bandwidth of attosecond pulses, coupled with their convenient inner valence and core level photon energies, makes them ideal for use in transient absorption[26]. In a proof of principle experiment, the strong-field ionization of Kr was studied by transient absorption of a ∼100 as x-ray pulse[27]. The results revealed not only the time-dependent populations, but also coherences between quantum levels generated during the ionization.

1.2.3 Fate of highly excited molecules

Not content with single-atom systems, chemists dream of applying attosecond pulses to the study of molecules. All the ultrafast atomic electronic dynamics expected in atoms are also expected in molecules, but with variations caused by the multi-nuclear structure of the molecule. For example, Auger decay occurs in molecules as well as in atoms, but it can occur both *within* one atom or *between* two atoms in the molecule. The latter process is called interatomic Coulombic decay (ICD)[28, 29]. ICD is extremely sensitive to the detailed vibrational motion of the atomic centers involved[30] as well as on the number of electron donors surrounding the initial site of the hole[29]. Experiments have so far been limited to the fs time domain[31–33], but attosecond probing of molecules and large atomic clusters is desirable.

Auger-like relaxation processes are not the only application of attosecond pulses in molecules. In many molecules, ionization of an inner-valence electron leads to an ion with significant two-hole, one-particle character[34]–that is, the orbital picture of ionization breaks down with relatively small amounts of internal energy left in the ion. Femtosecond XUV pump, visible probe experiments have yielded some surprising information on simple

molecules like N_2[35], where the superexcited state lifetime was measured to be less than 25 fs, and predissociation shown to compete with Auger decay. This area of chemical dynamics is a prime application of attosecond pulses.

1.2.4 Charge localization

Many attosecond experimentson molecules discussed in the literature so far have to do with electron localization. For example, attosecond electron localization in the molecular frame in H_2^+ and D_2^+ was demonstrated using only a strong infrared laser[36]. Similar experiments using attosecond pulse trains together with the infrared pulse followed, with the results indicating quantum interference between competing multiphoton pathways as the origin of the localization[37, 38]. Similar experiments have also been carried out on CO[39], a multi-electron molecule, having the added complexity of multiple electronic surfaces.

Strong laser fields can induce localization of electrons, but at lower intensities where the laser-molecule interaction is perturbative, localization of the electron (or hole) wavefunction is also an interesting question. In fact, recent calculations have indicated that electron correlation can be responsible for the migration of an initially localized charge carrier across a molecule[40], an intriguing effect that has not been experimentally demonstrated except indirectly[41, 42]. Electronic reorganization in LiH has also been considered theoretically, and seems to be feasible to study experimentally[43, 44].

1.2.5 Harmonic generation as an attosecond probe

High harmonic generation, to be discussed in detail in chapter 2, can also be used as an attosecond probe of molecular motion. The harmonic generation process can be thought of as consisting of three steps. First, when the driving laser field is at a maximum, it can become so strong as to overwhelm the Coulomb force holding a valence electron in an atom. The electron will tunnel out of the atom through the combined Coulomb/laser potential. Second, the laser field accelerates the electron in the continuum, turning it around as the sign of the laser field changes. Third, if the electron returns to the vicinity of the ion, it can recombine with the ion emitting a short-wavelength photon.

The third step of the harmonic generation process is quite sensitive to the details of nuclear motion on a fs-as timescale and therefore HHG can be used as a probe of ultrafast molecular motion. A simple question is, what happens to a molecule between the time an electron is tunnel ionized and the time it recombines to give harmonic light? The answer is available directly from the harmonic spectrum, since the energy of a harmonic peak is directly related to the duration of the electron trajectory that created it. In fact, the harmonic spectrum indicates ultrafast bond lengthening in H_2 as the electron travels through the continuum and a distortion of tetrahedral methane toward C_{2v} symmetry[45]. These distortions are precisely what would be expected based on the geometry of the ground state structure of the cation. The technique of measuring the proton motion is quite elegant and can be applied to many more molecules. However, the time window is limited to the durations of the harmonic-generating electron trajectories, which spans from about 1 fs to 2 fs in the case of harmonics of 800 nm light. Longer driving laser wavelengths will enable longer probing times.

The harmonics from diatomic molecules are interesting for another reason–when the molecular target is aligned, the harmonic spectrum exhibits a pronounced dip in amplitude in the middle of the spectrum, along with a sharp phase jump[46–49]. This minimum is interpreted as interference between harmonic emission from the two centers of the diatomic molecule, occurring as it does when the internuclear separation equals half the de Broglie wavelength of the re-colliding electron. The fact that the harmonic light encodes information about the wavefunction of the molecule used in HHG has also been exploited for tomographic imaging of the highest occupied orbital of the N_2 molecule[50].

Harmonic generation has also been used to probe polyatomic molecules, in experiments on N_2O_4[51] and SF_6[52, 53]. In these experiments vibrational motions on the fs timescale were monitored using the HHG yield as a probe. The harmonic yield was shown to be sensitive to the vibrational autocorrelation function[54], which can give the technique of HHG-probing an advantage over other femtosecond techniques for elucidating structure, like electron diffraction.

1.2.6 FELs and coherence in attosecond spectroscopy

Now, it is fair to ask at this point whether it is worth all the trouble of obtaining an attosecond pulse, inventing new pump-probe detection schemes using strong laser fields, and ending up with many grey hairs as a result, when the lifetime of the Auger decay in Kr was already known from analysis of the photoelectron lineshape measured at a synchrotron. Firstly, on most systems linewidth analysis is not possible due to, e.g., overlapping and unresolved peaks. But the above question misses a great advantage of time-resolved attosecond science, which is that the attosecond pulse is *coherent* and therefore so is its interaction with the target atoms or molecules[55]. This coherence means that all of the nonlinear optical techniques developed using visible and infrared light–techniques that reveal the couplings between eigenstates, for example, or that make quantum control possible–are in principle available in the x-ray regime as well, and can be used to study core-excited atoms and molecules[56–59].

It is natural to regard attoscience as an extension of femtoscience. There the coherent nature of ultrashort pulses enables the direct measurement of quantum-mechanical populations and coherences on their natural timescale. This is also a grand hope of attoscience: to measure the time-dependent density matrix for the electronic levels of an atom or molecule.

Already there have been many steps in that direction, but the largest hurdle to overcome is the miniscule flux of the attosecond radiation. Experiments are not in principle bound to be linear in the XUV-atom interaction, but successful nonlinear experiments are rare[11–15]. The challenge remains to make the attosecond pulse trains used above into intense isolated attosecond pulses.

The x-ray free-electron laser (XFEL) may provide intense attosecond pulses where laser-based sources cannot. XFELs deliver huge fluxes over large bandwidths, but the emission is of limited temporal coherence. A number of proposals for obtaining attosecond radiation from XFELs have been advanced, including seeding the XFEL with laser-generated harmonic light[10] and microbunching of free electrons using a few-cycle laser pulse[60]. Free-electron lasers with temporal and spatial coherence comparable to HHG sources, but with orders of magnitude higher intensities, will enable major progress nonlinear attosecond science.

1.2.7 Possible attosecond slicing of synchrotron light

Synchrotron radiation is also a possible source of attosecond light pulses. Femtosecond x-ray emission has already been demonstrated by ponderomotive interaction between a laser pulse and a co-propagating electron bunch. The light field leads to a femtosecond modulation in the transverse structure of the electron bunch. The x-rays generated in an undulator are also spatially modulated, with a fs-duration component spatially separated from the "long" multi-picosecond emission from the remainder of the bunch[61].

Potentially the same technique could be applied to make attosecond x-ray pulses tunable over the entire range of the synchrotron emission. The only requirements are that the laser used to slice the electron packet be a few-cycle carrier-envelope phase-stable source, and that the interaction between this laser pulse and the electron bunch occur in an undulator that is resonant across the laser bandwidth.

1.3 Summary

Attosecond science is a wide open field. Besides the applications demonstrated and discussed above, there are many more proposals for experiments on the attosecond behavior of electrons and nuclei, including electron diffraction[62], Fourier transform VUV spectroscopy[15], multiphoton x-ray interactions and double ionization, investigating the system response to the "sudden" removal of an electron[63], ultrafast single particle diffraction experiments on biomolecules, and many more.

If the rewards of attoscience are high, so is the difficulty in achieving them. Attosecond pulse production has been demonstrated by only a few groups around the world. And attosecond metrology is also an extremely demanding task. In the next chapter, a detailed discussion of laser-based high harmonic generation is presented and techniques for making and measuring attosecond pulses are discussed.

Chapter 2

High Harmonic Generation

2.1 Introduction

It has been just over twenty years since the first demonstration of strong field high harmonic generation (HHG) in a noble gas. Over this relatively short time, the theory and technology of harmonic generation and, subsequently, of attosecond pulse production has rapidly advanced and matured. From the early days when there was no adequate theoretical understanding of the HHG process, we can now calculate quite accurately the harmonic spectra, ionization rates, and phase matching behavior for high field processes. Technologically, the ever increasing sophistication of experiments has yielded extremely bright, extremely short, and extremely coherent sources for femtosecond and attosecond physics. It is the aim of this section to provide a history of high harmonic generation and of attosecond pulse production from the first experiments through the present time.

2.2 Attosecond pulse production

2.2.1 Early harmonic generation experiments

The invention of the laser brought a revolution in optical science. It was an extremely bright, extremely coherent source, with unimaginably narrow linewidths or very short pulse duration. Yet, because of the limited number of frequencies available from the various laser gain media, in the 1980s frequency conversion to ever higher photon energies was a major goal in the field of optics. Experiments on frequency conversion in rare gases yielded vacuum ultraviolet radiation, even up to the seventeenth harmonic of the fundamental 248 nm driving laser[64]. Yet, the conversion efficiency in these experiments was very low, on the order of 10^{-9} to 10^{-11}, and it monotonically decreased with increasing harmonic order.

Then in 1988, a breakthrough in frequency conversion occurred. Dubbed multiple-harmonic conversion[65], the 33rd harmonic of the driving Nd:YAG laser was observed, shattering the previous record for harmonic order, while simultaneously using much lower intensity. But that was not the most surprising finding: the harmonic intensity did not plummet with increasing harmonic order, but after a drop at low orders the intensity stayed roughly constant from the 5th all the way through the 33rd harmonic (a plateau structure),

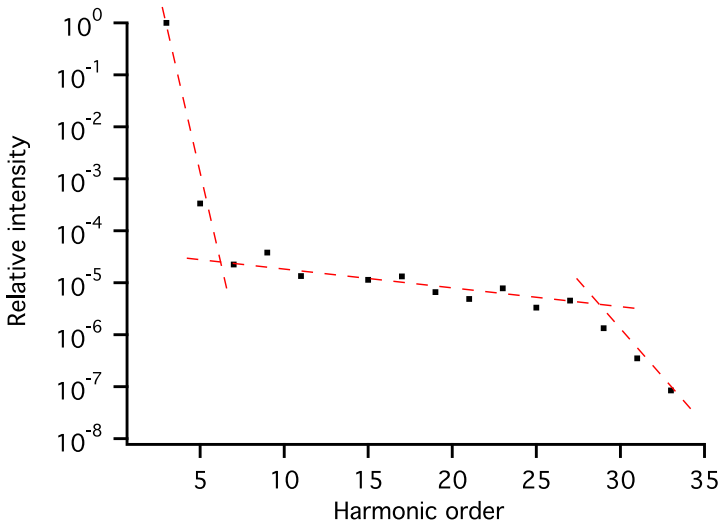

Figure 2.1: **An early HHG experiment.** This harmonic spectrum from ref. [65] was obtained using 3×10^{13} W/cm^2 intensity in a jet of 15 torr Ar gas. The driver laser was the fundamental of a 30 ps Nd:YAG laser. A sharp drop in intensity for the first few harmonic orders, a plateau, and another sharp drop at the harmonic cutoff are clearly visible (red dashed lines).

at which point it disappeared completely in a sharp cutoff (fig. 2.1). Clearly, this was a new regime in frequency conversion.

Experimental progress in the following years was rapid. Many more experiments [66–72] on high-field multiple harmonic conversion confirmed the drop, plateau, and cutoff structure first observed in ref. [65]. The conversion efficiency increased strongly with increasing atomic number, at the cost of reduced cutoff harmonic number. The laser intensity dependence of the conversion efficiency was measured, and again puzzling results were obtained. While the lowest order harmonics (third, fifth, and seventh) varied in intensity with the third, fifth, and seventh powers of the input energy respectively, the 21^{st} harmonic intensity varied roughly as the 8^{th} power of the input power, and the 33^{rd} harmonic varied as the 12^{th} power of the input[66]. This was a strong indication that while perhaps the conversion into low order harmonics could be treated with lowest-order perturbation theory, the conversion to high-order harmonics would require a quite different theoretical description.

Phase matching of the harmonic conversion process presented another mystery. Lowest-order perturbation theory indicated that the phase matching conditions should rapidly deteriorate with increasing harmonic order in the plateau, which (counterintuitively) seemed to imply that the atomic dipole responsible for generating the harmonics must have actually *increased* in magnitude with harmonic order [66, 67]. Here again was more evidence that a non-perturbative theory was needed to describe harmonic generation. But the phase matching experiments also settled some questions. For example, the analysis of phase-matching data in ref. [67] confirmed that the multiple harmonic conversion process created temporally coherent radiation.

The wavelength dependence of the harmonic emission was studied as well[70, 72], and here

was another curious result that a theory of harmonic generation would have to contend with. The cutoff energy in the harmonic spectrum decreased with shorter driver laser wavelength, and yet the conversion efficiency for any individual harmonic was increased.

So there were many challenges for a theory of harmonic generation. Clearly using lowest-order perturbation theory was not accurate. Actually, Pan, Taylor and Clark showed that the outlook for perturbation theory was even worse than the experiments indicated. They proved that the results of higher-order perturbation theory (e.g. using 11^{th}, 13^{th}, 15^{th} etc. order for calculation of the 11^{th} harmonic) that perturbation theory would never converge for the calculation of the plateau harmonics.

2.2.2 Developing a theory of HHG

Integrating the time-dependent Schrödinger equation described the harmonic generation results quite well[73–75]. This approach yielded some important insights. First, good agreement could be obtained between the calculated single atom response and the experimental spectrum, implying that in the experiments the interaction length was shorter than the coherence length and that therefore the harmonic yield could be increased (in principle) by changing the geometry. Secondly, and more importantly, the calculation of xenon harmonics[74] showed good agreement despite using only one electron in an effective potential. This is the single active electron approximation which makes calculation of harmonic spectra much simpler.

But the real breakthroughs in the theory of harmonic generation came in 1993 and 1994. First, in 1993, Corkum published his now famous three-step model of harmonic generation[76], which was introduced briefly in chapter 1. The content of the manuscript was simple. Harmonic generation was essentially described by (1) an electron tunneling out of its orbital in the target atom under the influence of the strong laser field, (2) classical propagation of the electron in the continuum, and finally (3) recollision of the electron with the parent ion, and release of an x-ray photon, figure 2.2. Despite the simplicity of the description, the results were staggering. First, it explained the odd harmonic structure of the HHG spectra. The tunneling step (1) only occurs when the laser field is near its extrema, twice per optical cycle. Therefore in frequency, a $2\omega_{laser}$ spacing would naturally be observed. The model explained not only the existence of a cutoff, but also the cutoff position, simply by tracking the energy of the electron in the continuum. The most energy that the electron can acquire and still recollide with the ion is 3.2 times the ponderomotive energy (U_p, the cycle averaged kinetic energy of the electron in the field), so the cutoff will come at $3.2U_p + I_p$, with I_p the ionization potential of the target atom. The model explained why there was a plateau since, classically, every half cycle generated photons in more or less the same probability up to the cutoff. Since U_p scales as the square of the driver laser wavelength, the model explained the frequency dependence of the HHG experiments. And, implicit in the model, a sub-femtosecond time structure was revealed to exist in the HHG emission. This last point was actually in confirmation of then-recent theoretical work of Farkas and Tóth[77] and of Harris *et al.* [78].

For all its success, the model had its shortcomings. For example, the classical calculation did not predict the phases of the electron wavepackets upon recollision, and therefore the phase of the harmonic light was not available. For this reason, the contribution of

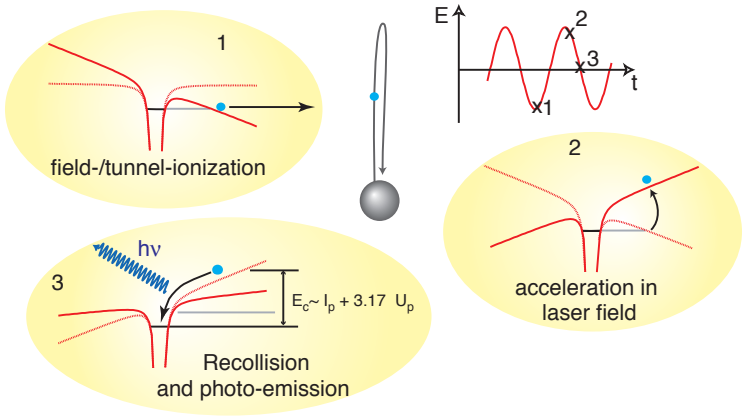

Figure 2.2: **3-step model for high harmonic generation.**At a maximum of the laser electric field, an electron can tunnel out of the distorted Coulomb potential that binds it to its atom (1). When the laser field changes direction (2), the electron is accelerated back toward the ion, gaining kinetic energy. The electron can strike the ion (3) emitting its kinetic energy and binding energy as an x-ray photon.

Lewenstein[79] from 1994 is perhaps the most useful of the theories of HHG. It recasts the three-step model in quantum mechanical language, describing the time-dependent dipole responsible for the radiation in terms of quantum mechanical dipole matrix elements for ionization and recombination of the electron and the motion of the electron in the continuum in terms of the semiclassical action. It also includes a simple description of the transverse spreading of the electron wavepacket at it travels through the continuum, which makes the current density seen by the ion (and therefore the conversion efficiency) lower when longer driver wavelengths (and therefore longer excursions of the electron into the continuum) are employed, in agreement with experiment. Because of its simplicity and accuracy, this theory is still in wide use for the description of harmonic generation, especially by experimentalists.

2.2.3 Attosecond time structure of HHG

It was not long after the first experiment on HHG that the potential for attosecond pulses was proposed[77]. Again, the idea was simple and elegant. The harmonic spectra comes in a series of equidistant lines, just like a laser oscillator. If these lines are phase-locked with respect to each other, then the harmonics will come as a series of pulses with characteristic attosecond character in the time domain, as in fig. 2.3. Since at this time it was already clear that the harmonic radiation was temporally coherent[67], the experimental realization of attosecond x-ray pulses depended on the degree of spatial coherence that could be achieved, and on the as-yet unknown phase structure of the harmonic radiation. Yet it was not clear that either of these constraints would be satisfied in HHG. For example, in ref. [78], the

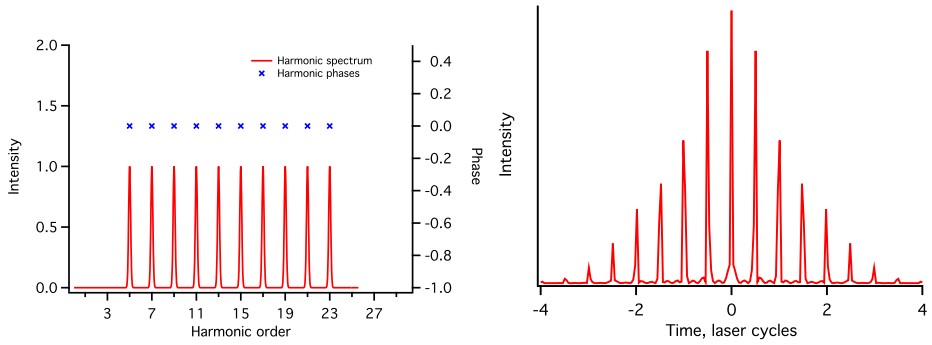

(a) (b)

Figure 2.3: **Hypothetical HHG spectrum and phase (a), and Fourier transform (b).** The transform clearly shows sub-laser-cycle time structure, which for visible lasers implies sub-femtosecond time structure.

authors mention an exchange with Kulander and Schafer regarding the unpredictability of calculations of the harmonic phase.

The first of these questions to be answered was that of spatial coherence. There were indications that the harmonic light was spatially coherent: for example, the far-field mode pattern of the harmonic beam could be adjusted by changing the spatial distribution of atomic dipoles excited in the interaction region[80]. But the natural experiment to do was a two-slit interference experiment, which shortly thereafter showed that the harmonic radiation was indeed at least partially spatially coherent[81]. In fact, the degree of spatial coherence measured by two-slit interference experiments steadily increased[82–85] until perfect coherence was measured using harmonics from a waveguide source. A useful review of the mathematical treatment of coherence in the context of harmonic generation is given in [82].

With temporal and spatial coherence confirmed, the challenge of realizing the attosecond time structure in harmonic sources was to find a way to measure the phases of the harmonics. Because spectral phase measurement techniques like FROG[86] and SPIDER[87] in the visible regime are nonlinear, they cannot be realized with the very low intensity harmonic output. (Not only that, but the beam splitters and combiners routinely used in the visible have no analogue in the XUV.) So, the temporal characterization of the HHG emission relied on visible/XUV two-photon processes from the beginning[88]. After initial indications from Papadogiannis *et al.* that the harmonic emission was coherent[89], Paul *et al.* used a visible/XUV two-photon process in argon gas to conclusively prove that the harmonics were indeed phase locked and that the HHG emission consisted of a series of attosecond x-ray bursts[90].

The essence of their experiment was simple, and bears repeating here. Normally, the photoelectron spectrum of Ar would consist of peaks at the harmonic frequencies, offset by the atomic ionization potential. These peaks are, naturally, spaced by twice the IR laser photon energy. Now, if IR light is present when the photoionization takes place, it can lead to two-photon transitions in which the free electron ends up with not an odd multiple of the

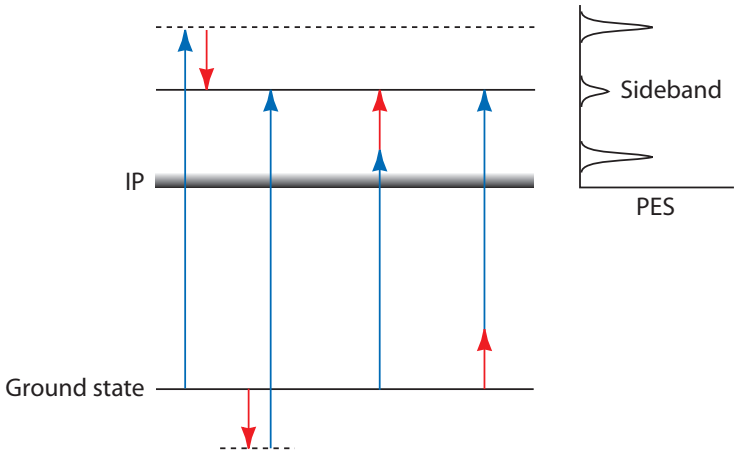

Figure 2.4: **Attosecond pulse train measurement.** Ionization of an atom by an attosecond pulse train leads to photoelectron peaks with spacing twice the driving laser photon energy. If the driving laser light is added to the interaction the ionization may involve the absorption or emission of a visible photon as well, leading to sidebands in the photoelectron spectrum. The sideband quantum state can be accessed by multiple quantum pathways, and the time-dependent sideband interference behavior reveals the time-dependent behavior of the attosecond pulse train.

laser photon energy, but an even multiple. These peaks in the photoelectron spectrum are the result of four interfering quantum pathways, as illustrated in fig. 2.4. From the even-order peak intensity versus IR delay, the phase difference between neighboring harmonics can be deduced. This is similar to the idea of SPIDER[87], where the phase differences between different spectral components of a laser pulse are determined interferometrically. The result in the case of HHG was a train of 250 as bursts, the first ever measurement of sub-fs pulses[90].

2.2.4 Isolated attosecond pulse production

Since each attosecond burst in the pulse train produced in HHG follows the cutoff law $E_c = I_p + 3.2U_p$, there must be one pulse in the train that possesses the high energy photons not produced in other weaker half-cycles of the driving laser field, as illustrated in fig. 2.5. It is not difficult to calculate the duration of the driving laser pulse that is required to produce a *subfemtosecond* high-photon-energy pulse. The minimum bandwidth of the x-rays is determined by the uncertainty principle: $2\pi\Delta\omega\Delta t = 0.44$ (for Gaussian-shaped light pulses) yields $\Delta\omega = 2.76$ fs$^{-1} = 1.82$ eV. This is the amount by which E_c for the strongest harmonic generation event must exceed all the others in the train. Using the cutoff law plus the fact that $U_p = 9.33(\lambda/\mu\text{m})^2(I/10^{14}\text{W cm}^{-2})$ eV, one finds that the half-cycle of the driver that actually generates the unique attosecond pulse must be 10^{13} W/cm^2 higher in intensity than the neighboring half cycles 1.33 fs away (for 800 nm radiation). Then the

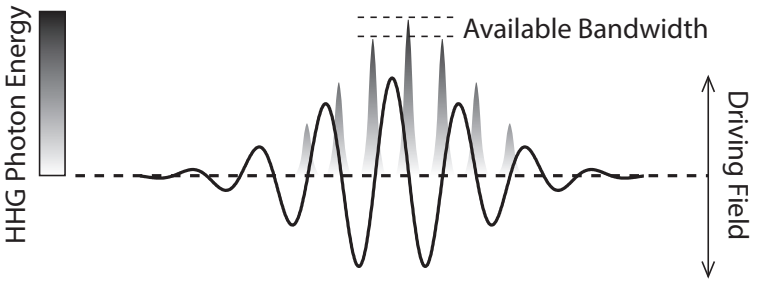

Figure 2.5: **How to obtain an isolated attosecond pulse by shortening the duration of the HHG driver.**The central half-cycle of the driving field must generate photon energies significantly larger than neighboring half-cycles. Thus the pulse intensity must change rapidly–or, equivalently, the pulse must be extremely short.

maximum pulse duration is determined by the peak intensity used, as shown in fig. 2.6. This indicates that a sub-fs x-ray pulse could in principle be obtained using a 7 fs driver at 800 nm wavelength, with peak intensity 4×10^{14} W/cm^2. This simple consideration actually gives remarkable agreement to the generation conditions used to generate the first isolated attosecond pulses[91]: 5 fs and 750 nm, with the peak intensity adjusted to obtain an isolated attosecond pulse at 93 eV.

There is a complication to the above analysis. Shortening the driver pulse of course has its limitations. As the requirement on pulse duration becomes more and more stringent, the spectral width required to support the short pulse–and therefore the difficulties in generating it, compressing it, transporting it, amplifying it, *etc.*–become larger inversely. And a major limitation on attosecond pulse production is that if the HHG conditions are correct to yield an attosecond pulse, but the electric field is phase-shifted with respect to the envelope, two attosecond pulses will be obtained instead of one[17]. Control and manipulation of the phase of the carrier wave with respect to the driver pulse envelope (carrier-envelope phase, CEP)[92] is therefore a requirement for attosecond pulse production. The CEP is the temporal offset between the laser cycle maximum and the pulse envelope maximum, converted to a phase by multiplying by the laser frequency.

Implicit in the above discussion is a useful concept for the science of attosecond pulses: the harmonic emission must be *gated* both temporally and spectrally to achieve isolated, sub-fs x-ray pulses. Because of the ready availability of filters and of mirrors with narrow, defined reflectivity bands in the XUV, the main problem in creating attosecond pulses is that of temporal gating of the harmonic emission. Many ways to temporally gate harmonic emission have been invented, each with their own advantages and drawbacks.

First, we will discuss so-called two-color gating. The concept is simple: if a second color of light is added to the fundamental driving laser pulse, harmonic emission is curtailed every time the two fields destructively interfere and is enhanced when they constructively interfere (once every cycle). This is illustrated in fig. 2.7. In this case, adding some second harmonic field to interfere with the fundamental increases the available bandwidth for attosecond pulse production and also relaxes the constraint on the pulse duration of the fundamental driving field. Not only that, but the second harmonic field can also increase the cutoff considerably

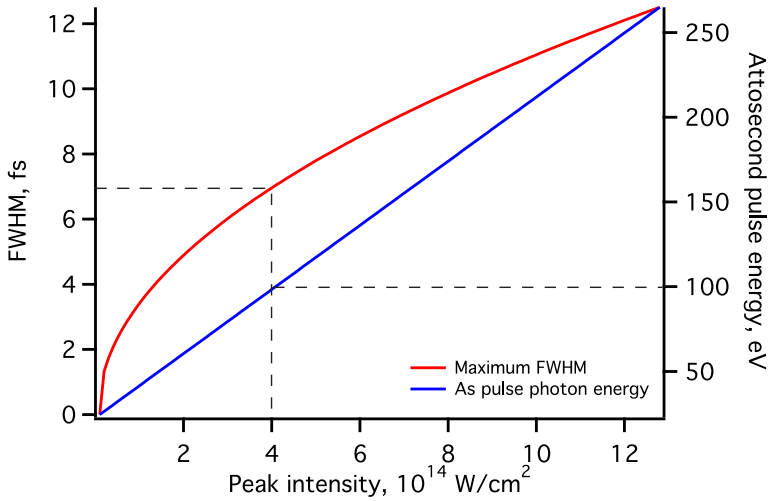

Figure 2.6: **Constraints for sub-fs x-ray pulse production using the intensity variation of a short driver pulse.** Calculated pulse duration required to provide a 1 fs x-ray pulse as a function of intensity (red), and calculated attosecond pulse photon energy as a function of intensity (blue).

beyond the limit of a single-color field[93, 94]. The subharmonic also has been considered for two-color gating[95], with the advantage that high-energy photons are produced only once every two cycles, as opposed to every cycle in the case of a second-harmonic gating field and every half cycle in the case of the fundamental alone. But the subharmonic of 800 nm is 1.6 μm, which is difficult to work with experimentally. Equally interesting is the idea of a gating field that is not commensurate to the driving laser frequency[96]. While this idea has been considered theoretically, it has not been implemented experimentally so far.

While it may seem that the second harmonic scheme is easy to implement experimentally, there is in fact a hidden difficulty. One cannot simply set a nonlinear crystal in the driver beam as it approaches the HHG generation focus–the polarization of the second harmonic field will be orthogonal to the driver laser. To create a collinear polarization, one requires type-II phase matching, which in turn requires a cross-polarized component in the driver field. Thus broadband polarization control becomes necessary for implementation of the multi-color gating methods discussed so far.

Besides assisting multi-color HHG, polarization itself is a valuable tool in gating harmonic generation. The second step of the three-step model for HHG is (quasi-) classical propagation of the electron in the continuum. If the laser field that drives the electron propagation is not perfectly linear, the electron will be dragged sideways and miss the ion, never to recombine[97]. So, a laser pulse that has a short time of linear polarization between circularly polarized segments will generate harmonics only for a brief interval in the middle[98]. This is polarization gating, a very powerful technique for isolated attosecond pulse production. The polarization gate makes extremely broadband XUV pulses, but it suffers from very low flux. There are two reasons for this: one is that the HHG target atoms are ionized during both the linear and the circular portions of the laser pulse. So as a result the system is

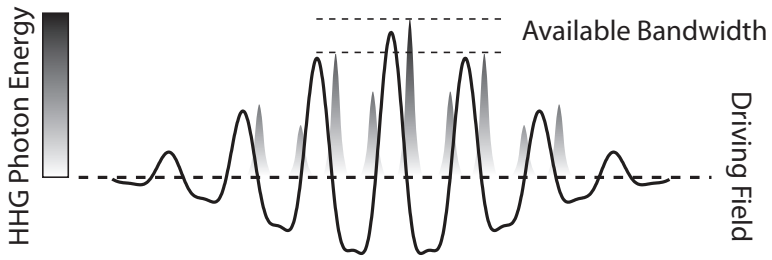

Figure 2.7: **Two-color attosecond pulse production.** Addition of second-harmonic light to the HHG driving field reduces the harmonic yield and photon energy every other half cycle. Therefore, the available bandwidth for attosecond pulse production is increased (or, equivalently, the maximum allowable pulse duration for a 1 fs x-ray pulse is increased).

already strongly ionized after the first (circularly polarized) portion of the pulse, inhibiting HHG in the second (linear) portion. The other reason is that the harmonic generation actually occurs at a local minimum of the driver pulse intensity envelope. The way around this difficulty is the double optical gate, which combines polarization gating and two color gating[99]. Double optical gating allows to have a very strong linearly polarized field during the HHG interaction, producing large x-ray fluxes at high harmonic orders[100].

If plasma formation is the worst enemy of polarization gating it is the best friend of ionization gating[101–103], which capitalizes on the transiently rising plasma density[101] in the HHG interaction region to spoil phase matching halfway through the driver laser pulse and therefore to gate harmonic emission on the leading edge of the driver pulse. Ionization gating will be discussed in detail in chapter 6.

2.3 Attosecond Metrology

2.3.1 Autocorrelation

Having briefly reviewed the history of high harmonic generation and the various kinds of gating used to produce isolated attosecond pulses, we now turn to the characterization of attosecond radiation. As previously mentioned, the conversion efficiency of harmonic generation is extremely low, and as a result two-photon techniques involving two XUV photons are only available with considerable effort (and as yet only in the femtosecond regime)[11–15]. Typically, some hundreds of pJ of harmonic light will be delivered to the interaction region in around 100 as. Combined with typical two-photon cross sections around 10^{-52} cm^4(see chapter 7 in [104]), this would lead to an optimistic estimate of one atom in 10^7 undergoing two-photon excitation, compared with around one in 10^4 undergoing single photon interactions with the field. For an interaction volume of about 10 μm diameter and 500 μm length, with one torr pressure, this is about 1 to 10 molecules, compared with around 1000 linear interactions. Clearly, nonlinear optics in the x-ray regime is possible with advances in attosecond pulse energy, repetition rate, and detection efficiency. But the former two limitations on attosecond experiments have not been overcome yet.

2.3.2 RABBITT

Given that nonlinear x-ray interactions cannot be used for autocorrelation of attosecond pulses, the only option for characterization is comparison of the attosecond emission to the leftover driving infrared radiation. In fact, this was noted very early on in the field of harmonic generation[18]. The nonlinear process used in this attosecond cross correlation is atomic photoionization, where the electrons interact not only with the attosecond field but also with the strong infrared field leftover from the harmonic generation process. The cross correlation of an attosecond pulse train with an infrared field, a technique known as "reconstruction of attosecond beating by interfering two-photon transitions," or RABBITT[90], was already described briefly in section 2.2.3. In RABBITT, the relative phases of individual harmonics are retrieved. The harmonics ionize an atom, leaving an outgoing photoelectron wavepacket with electron energies spaced by the harmonics spacing, namely twice the laser photon energy. Introducing the leftover laser light allows an electron to either gain or lose one infrared photon worth of kinetic energy. Therefore, photoelectron peaks appear in between the energies due to the harmonics alone. Each of these sidebands represents the sum of quantum paths, each involving either emission or absorption of an infrared photon. The relative phase of the harmonics n and $n+1$ is therefore encoded in the sideband intensity. To retrieve the relative phase, one must change the phase of the infrared light in a predictable way and monitor how the sideband intensity changes. This is done by simply changing the time delay of the infrared pulse with respect to the attosecond pulse train.

Once the relative phases of the harmonics are known, it is a simple matter to perform a Fourier transform using the harmonic intensities (obtained from the photoelectron spectrum) and phases to obtain the shape of the attosecond pulses making up the pulse train. It is interesting to note that the harmonics almost always carry a positive chirp, called the attochirp[105], related to the trajectories of the electrons in the continuum during the HHG process. Electrons that spend longer in the continuum are accelerated to higher energies and therefore release higher energy x-rays, so the high energy photons trail the low energy ones in time. This positive chirp can be compensated wholly or partially by inserting some dispersive material into the harmonic path. Since the chirp is positive a material with negative dispersion must be employed, and there are several choices of metals with negative dispersion for selected regions of the soft x-ray spectral region. This approach was successfully used to compress attosecond pulses in a pulse train from 480 as to 170 as duration[106]. Compression can also be achieved using chirped multilayer mirrors[107] (see sections 3.5 and 3.9).

2.3.3 X-SPIDER

The optical technique of "spectral phase interferometry for direct electric-field reconstruction," or SPIDER[87], is an extremely powerful way to characterize light pulses. In SPIDER the pulse to be measured is split into two copies, one copy is frequency shifted slightly compared to the other, and then the two beams are recombined in a spectrometer to measure the fringe pattern that results when they interfere. The small frequency shift means that the phase difference is measured between frequency ω of the first pulse and frequency $\omega + \delta\omega$ of the second pulse. One therefore measures the derivative of the spectral phase, $\partial\phi/\partial\omega$. In practice the frequency shift is accomplished by sum frequency generation of both

pulse copies with two slightly different colors.

Since spectral interference measurements are relatively easy compared to photoelectron measurements, it would seem that SPIDER offers a convenient way to measure the phase–and thus, through a Fourier transform–the temporal structure of an attosecond pulse. But, the complication is the frequency shift. How to obtain two copies of the same attosecond pulse, one slightly frequency shifted with respect to the other? There are no convenient beamsplitters in the soft x-ray region and, as discussed in section 2.3.1, there are no efficient nonlinear optical interactions either.

Yet an x-ray version of SPIDER–X-SPIDER–has been demonstrated for high harmonic beams. One must split the driving pulse in two, frequency shifting one copy slightly. Then the harmonics produced by the two driver pulses have slightly different frequencies and the interference pattern of the two harmonic beams in a spectrometer reveals the harmonic spectral phase. The assumption here is that everything else is the same about the harmonic generation process. Unfortunately, that assumption is not a safe one. The harmonic generation process is extremely sensitive to the wavelength of the driver laser through macroscopic and microscopic effects. Macroscopically, the wavelength determines the spot size and therefore affects the intensity. Microscopically, the intensity determines not only the (highly nonlinear) ionization rate in the first step of the HHG process, but also changes the electron trajectories, and the atomic phase contribution to the macroscopic phase matching. In short, X-SPIDER has many more phase contributions than visible-SPIDER, the results must be taken with a (large) grain of salt. Fortunately, there is another very general method for determining the spectral phase, and therefore the attosecond temporal structure, of harmonic pulses.

2.3.4 FROG-CRAB

The most general way of characterizing attosecond radiation is through streaking of the photoelectrons generated by the XUV pulse. The reconstruction of the electron emission times is accomplished through a technique called FROG-CRAB, or "frequency-resolved optical gating for coherent reconstruction of attosecond bursts." It is an extension of the RABBITT technique in which the attosecond radiation is overlapped with a visible or infrared laser pulse in gas target. The gas is ionized by the XUV light, but instead of using one quantum-mechanical photon of infrared light, in FROG-CRAB the field is large enough to be "classical" in nature–the electrons are dragged around by the smoothly changing electric field as they exit the atom and fly towards the detector (figure 2.8). The light field thus changes the momentum of the electrons continuously, and the interaction can in fact be written as a phase applied to the electron wavepacket in the momentum domain. For example, an electron wavepacket with wavefunction Ψ at frequency ω ($\Psi \sim \exp(-i\omega t)$) can be upshifted in frequency–or, alternatively, in momentum–by applying a phase shift that varies linearly in time: $\Psi \times \exp(-i(\delta\omega)t) = \exp(-i(\omega + \delta\omega)t)$.

It is precisely this time-varying phase shift that the laser field provides. The field applies a gating function to the electron wavepacket, whose effect depends on the shape of the electric field, and the output of which encodes both the field and the shape of the original wavepacket[108–110]. The momentum-space wavefunction of the electron released by the XUV pulse is[109]:

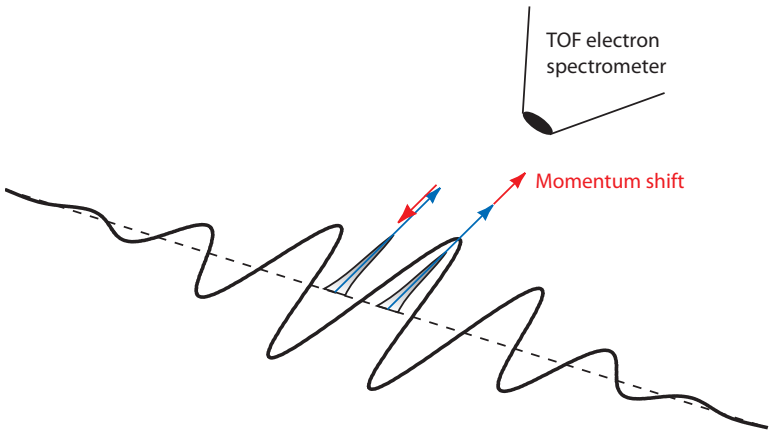

Figure 2.8: **FROG characterization of an attosecond pulse.** As the time delay between the visible field and the attosecond field changes, electrons released by the attosecond pulse experience different momentum shifts due to the laser pulse. A time-resolved momentum distribution of the photoelectrons contains enough information to unambiguously reconstruct both the x-ray and visible pulses.

$$\Psi(p,\tau) = \int_{-\infty}^{\infty} E_{XUV}(t) d(p + A(t+\tau)) e^{-i\varphi(p,t+\tau)} e^{i(p^2/2 - \Omega_{XUV} + W)t} dt \tag{2.1}$$

Here, p is the final momentum of the electron, Ω_{XUV} is the central photon energy of the XUV pulse, W is the ionization potential of the atom, τ is the delay time between the the XUV and infrared pulses, $A(t)$ is the vector potential of the infrared field, $d(p)$ is the dipole transition matrix element between the bound state and the continuum state of the electron at momentum p, $E_{XUV}(t)$ is the complex-valued envelope of the XUV pulse, and $\varphi(p,t)$ is the quantum phase shift experienced by the electron due to the field. This phase shift can be calculated from the vector potential[109]:

$$\varphi(p,t) = \int_{t}^{\infty} \left(pA(t') + \frac{A^2(t')}{2} \right) dt' \tag{2.2}$$

One can see that the laser light is essentially applying a delay-time dependent phase to the electrons emitted by the XUV pulse. Collecting the photoelectron spectrum for many time delays yields enough information to reconstruct both the attosecond pulse shape and the gating function (the infrared pulse vector potential)[86]. One may use the FROG-CRAB technique to reconstruct the attosecond pulse shape if the electron emission is considered instantaneous (see chapter **??**). But it is also useful for reconstructing emission times of electrons that are not emitted instantaneously, as in the experiments described in section 1.2.1.

Chapter 3

Experimental Setup

3.1 Overview

Briefly, the experimental system consists of a 25 fs, 0.8 mJ titanium:sapphire laser amplifier operating at 3 kHz which is temporally compressed to 6 fs duration, carrier-envelope phase (CEP) locked, and used to drive high harmonic generation in neon gas. The harmonic pulses can either be directed into a homebuilt spectrometer based on a 10,000 line/mm (100 nm spacing) transmission grating, or reflected together with the leftover driving light back to the interaction region of a photoelectron spectrometer. A schematic of the entire system is shown in figure 3.1. In the following sections, the various parts of the experimental apparatus will be described in detail.

3.2 Oscillator

The laser system is seeded by a Rainbow oscillator from Femtolasers. The optical layout of the oscillator is shown in figure 3.2. At a pump power of 3.0 W, the output power of the oscillator in CW operation is about 410 mW. The mode-locked power is generally not a useful number on a day-to-day basis; only the beatnote signal used to lock the oscillator CEP is valuable (see section 3.3). The repetition rate of the oscillator is 78.58 MHz. The dispersion of the oscillator cavity is balanced by chirped mirrors and a pair of fused silica wedges so that a very broad spectrum is coupled out of the cavity during mode-locked operation, shown in figure 3.3.

The oscillator is a confocal cavity with Ti:Sapphire gain medium. Mode locking is achieved by self-focusing of the oscillator beam in the Ti:Sapphire crystal. As a result, the effective focal length of the cavity focusing mirror is decreased slightly in mode locked operation as compared to continuous wave (CW) operation. To mode lock the oscillator, therefore, one must pre-adjust the cavity to overlap the *effective mode-locked focus* with the gain region in the crystal. Then mode locking can proceed. To achieve this overlap, the oscillator focusing mirror can be translated along the beam axis using a screw, referred to as the stability range adjustment. The stability range position for optimal mode-locked operation is shifted significantly inwards toward the crystal (stability range screw turned clockwise) versus the optimal position for CW operation.

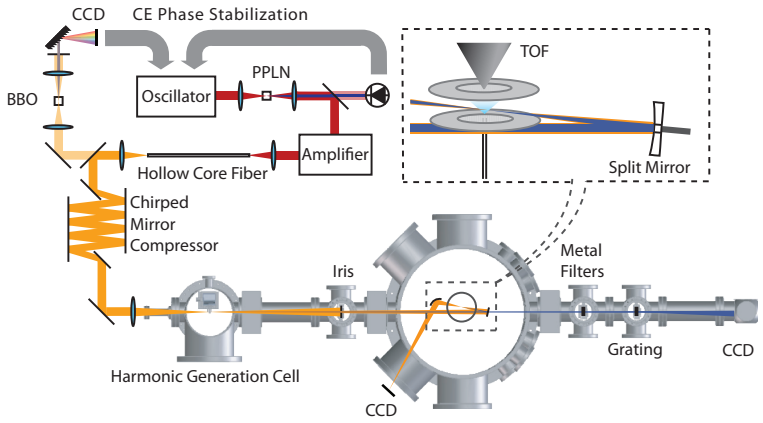

Figure 3.1: **Overview of the experimental apparatus.** The laser system is composed of a Rainbow oscillator, which seeds a Femtopower amplifier. The CEP of the oscillator is controlled by two feedback loops, one high-bandwidth loop using difference frequency generation in a periodically poled lithium niobate crystal (PPLN) and a low-bandwidth loop after the amplifier based on second harmonic generation in a β-barium borate (BBO) crystal. The amplifier output is spectrally broadened in a hollow core fiber and temporally recompressed using a chirped mirror compressor. After the harmonic generation cell, the beam can be reflected back to the interaction region of a time of flight (TOF) spectrometer, or sent to a homebuild soft x-ray spectrometer.

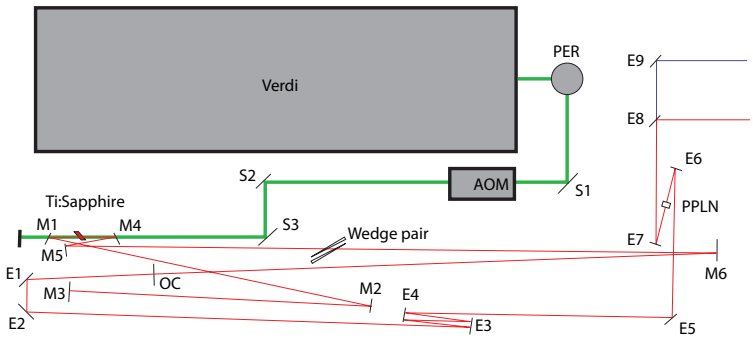

Figure 3.2: **Oscillator optical layout.** The oscillator is pumped by a Verdi v-6 laser. Cavity mirrors are marked with an M. The cavity end mirrors are labelled OC and M3. Extra-cavity mirrors are labelled with an E. E3 and E4 are chirped mirrors which correct the dispersion of the output coupler. A periodically poled lithium niobate (PPLN) crystal is located between E6 and E7, which generates difference-frequency light. The leak through E8 is used for CEP stabilization. E8 directs the oscillator output into the stretcher.

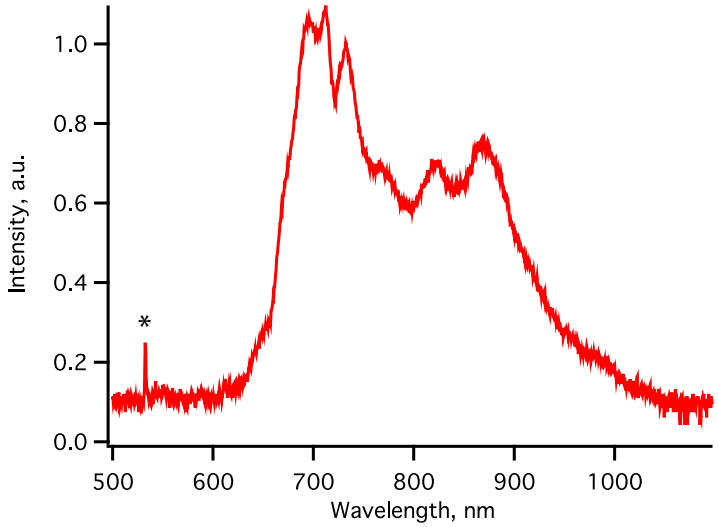

Figure 3.3: **Oscillator spectrum.** The oscillator output spectrum is extremely broad, supporting a ∼10 fs pulse. The peak marked with a star at 527 nm is scattered pump laser light.

Optimization of the oscillator performance is done in the following way, referring to figure 3.2.

Optimize CW power The oscillator can be made to operate in CW mode by turning the stability range screw counterclockwise. Place the power meter after mirror E5. Optimize the stability range by turning the screw anti-clockwise. Now, for 3 W input power the output should be over 400 mW. If it is not, clean the crystal with solvent and check the power again. If this does not bring the system to the required power, clean the other optics in the cavity one by one, checking the output power after each one. If the power is not improved, or is not improved enough, gently tune the cavity end mirrors. First turn M3 then OC in the vertical direction, then turn them in the horizontal direction. Iterate this a few times to make sure you have the best output. As you are working in the cavity, it is good practice to periodically check the stability range, as adjustments you make elsewhere can change the optimal stability range setting.

Optimize mode locking Now that the single-mode power is high, turn the stability range screw clockwise until the power reaches about 180 mW and push the mode lock button. If you are lucky the laser will mode lock immediately. Generally, this is the case because alignment of the cavity for maximum CW power also favors easy mode locking. If the laser will not mode lock, try other stability range positions near the one you were using. If it still will not mode lock, remove some glass from the cavity by turning the wedge control to the "minus" direction for several seconds. The oscillator should mode lock easily over a wide range of glass insertion. If it does not, there is an instability in the cavity still. Go back to the previous step.

Optimize beat note When the oscillator is mode locked, the output pulses are very short and undergo both self-phase modulation and difference frequency generation in the periodically poled lithium niobate (PPLN) crystal between focusing mirrors E6 and E7. The leak through turning mirror E8 is picked up by E9 and directed through a filter onto a photodiode. Make sure that the 78 MHz component of the diode signal is maximized by turning mirror E9. At that time, a beat signal should also appear in the FFT trace. The peaks corresponding to the beat note should be at least 30 dBm above the noise floor, if not higher. If the mode-locked operation of the oscillator is good but there is not enough beat signal, likely the nonlinear conversion in the PPLN crystal is the culprit. When viewed from above, the PPLN should have a white streak starting at the front face and trailing off toward the back face. This is scattered continuum light from self-phase modulation. Move the PPLN slightly along the beam axis and see if it increases the beat signal. If that does not work, check the mode of the beam before and after the PPLN. If it is dramatically changed, the beam is focused on a damage spot in the crystal. Steer the beam sideways a bit using E6 until the beam is off the damage. If you do this you will have to compensate the pointing of the oscillator into the stretcher. To do that, make sure that the beam is centered on the entrance of the Faraday isolator using E7. Then use E8 to put the beam on the iris after the stretcher. You will likely need to iterate between those two mirrors.

In order for the carrier-envelope phase of the oscillator pulses seeding the amplifier to be stabilized, the carrier-envelope offset (CEO) frequency must be stabilized. In order to measure the CEO frequency, the short pulses from the oscillator are focused into a PPLN crystal optimized for difference frequency generation. The spectrum of the oscillator beam simultaneously broadens by self-phase modulation in the PPLN and also generates difference frequency light. The overlapping portion of the spectrum, near 1100 nm, is filtered out with a dichroic mirror and the beam is focused on a fast photodiode, the output of which is shown in figure 3.4. The Fourier transform of the time-dependent diode signal consists mainly of harmonics of the 78.58 MHz repetition rate of the oscillator. However, there are also weaker components in the Fourier spectrum originating from beating between the difference frequency light and the fundamental spectrum of the oscillator, figure 3.5. This beat signal should be 30 dBm or more above the noise floor when the oscillator is working properly (dBm represents decibels referenced to a signal of 1 mW average power).

The beat signal frequency is the carrier-envelope offset frequency, as illustrated in figure 3.6. A homebuilt feedback loop locks the carrier-envelope offset frequency to 29.45 MHz by varying the oscillator pump power with an acousto-optic modulator (AOM). The constant carrier-envelope offset frequency means that every 8th oscillator pulse has identical CEP.

3.3 Fast loop CEP-locking

In order to lock the CE-phase of the laser, f_{ceo} must be stabilized with respect to f_{rep}. In order to do this, f_{rep} and f_{ceo} are both measured in the oscillator. The measurement of f_{rep} is straightforward: a photodiode monitors the light leaking through the retroreflector in the stretcher (see section 3.4). The output of this diode (labelled “MHz trigger out” on the laser

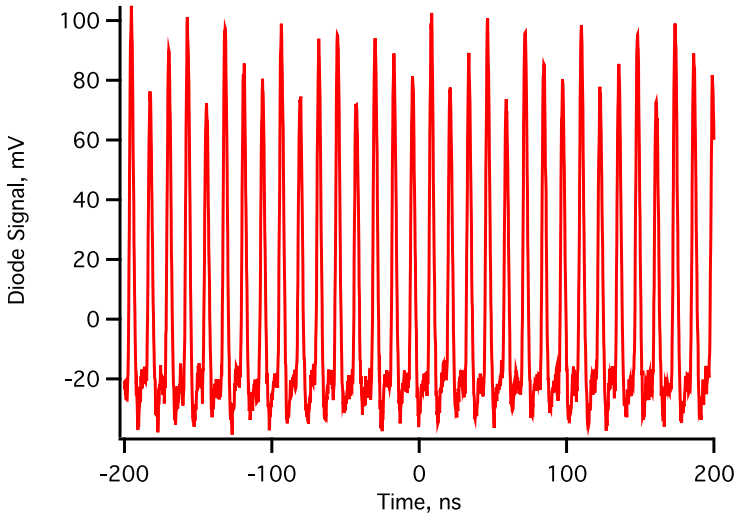

Figure 3.4: **Oscillator pulse train.** The leak through mirror E8 is put through a bandpass filter at 1100 nm and recorded using a fast photodiode. The oscillation of the peak height is due to interference between light generated by self-phase modulation and light generated by difference frequency generation in the PPLN crystal.

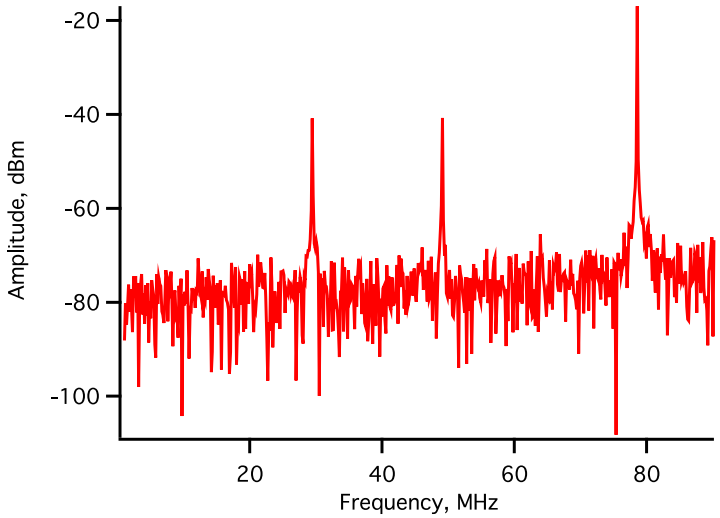

Figure 3.5: **Fourier components of the oscillator pulse train.** The repetition rate f_{rep} of the oscillator comes at about 78 MHz. The other two components are the carrier-envelope offset frequency f_{ceo} (see firgure 3.6) at around 30 MHz and $f_{rep} - f_{ceo}$ at around 50 MHz. These latter Fourier components should be at least 30 dBm above the noise floor.

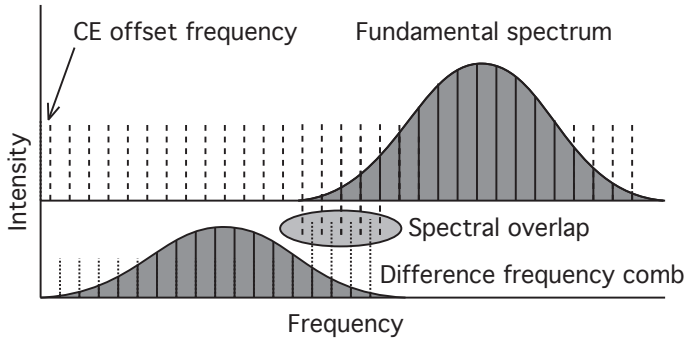

Figure 3.6: **Frequency components of the oscillator comb structure, showing the carrier-envelope offset frequency measurement.** The fundamental spectrum of the oscillator is composed of a series of lines equally spaced by f_{rep}. When extrapolated back to the radio frequency range, this comb is offset from zero frequency by the carrier-envelope offset frequency f_{ceo}. By contrast, a difference frequency comb generated from the oscillator comb has zero f_{ceo}. The combined field in the region of spectral overlap has a temporal modulation at f_{ceo} which can be detected by a Fourier transform (see figure 3.5).

body) is shown in figure 3.7. The diode output is sent to the "OSC" on the timing unit used to trigger the amplifier pump laser. The "MON" output on the timing unit reproduces the "OSC" input. This output is filtered by both a low- and high-pass RF filter to remove all components other than at 78 MHz, then sent to the JILA phase detector box "f_{beat}" input (figure 3.8).

The JILA phase detector box also requires a signal at frequency f_{ceo}. This is accomplished by taking the output of another photodiode, the one measuring the leak through oscillator mirror E8. This signal has Fourier components at both f_{rep} and f_{ceo}; f_{ceo} is selected by filtering the RF signal.

The phase detector (also referred to as the divider box) divides f_{rep} by 32 and divides f_{ceo} by 12. The two signals are now both close to 2.4 MHz and are multiplied together in a mixer to form a new signal with a beat frequency equal to the difference between the divided inputs. The phase of this sine wave is output on the "PHASE MON OUT" terminal of the divider box. When the CEP is locked this signal is a flat line (figure 3.10), but when the CEP is unlocked this ranges quickly from $-\pi$ to π radians (figure 3.11). A schematic of the divider box circuit is shown in figure 3.12.

The error signal provided by the divider box is fed to the input of the loop filter box. The loop filter box is essentially a PID controller with variable gain, sign, and frequency response. Its output of the PID loop is fed to a fast summing circuit (called the fast summer), which adds the feedback signal provided by the loop filter box with a bias set by hand using a knob on the fast summer. The output of the fast summer is fed directly to the AOM (acousto-optic modulator) driver, which is in turn connected to an AOM inserted in the oscillator pump beam. Varying the power of the pump laser allows tuning of f_{ceo}, which is the feedback

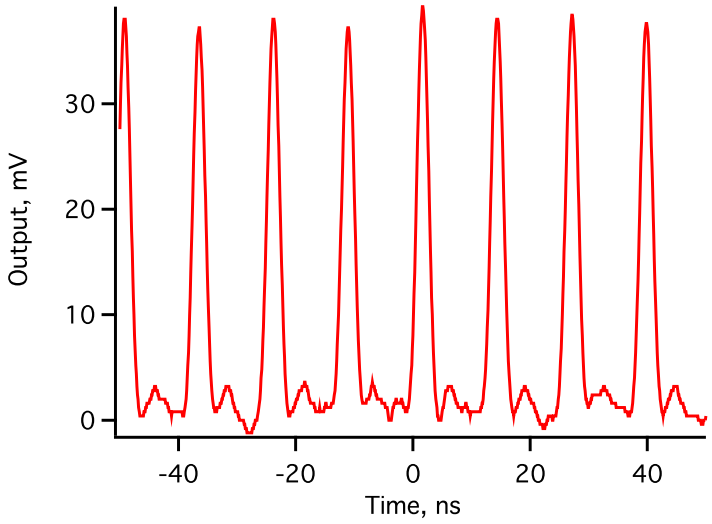

Figure 3.7: **Oscillator pulse train for measurement of f_{rep}.** The measurement of f_{rep} is accomplished by measuring the pulse train, then filtering it to remove all components other than that at 78 MHz.

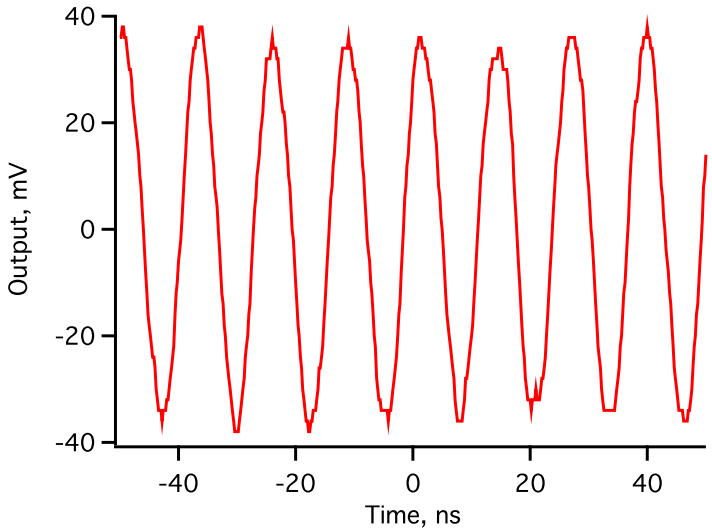

Figure 3.8: **Measurement of f_{rep}.** The filtered oscillator pulse train signal, having only one Fourier component at f_{rep}.

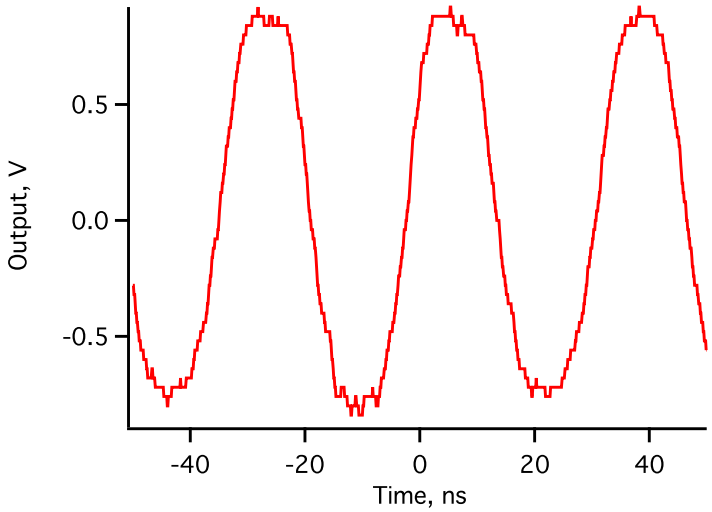

Figure 3.9: **Measurement of f_{ceo}.** The filtered oscillator pulse train signal, having only one Fourier component at f_{ceo}. Note that the horizontal scale is the same as figure 3.8.

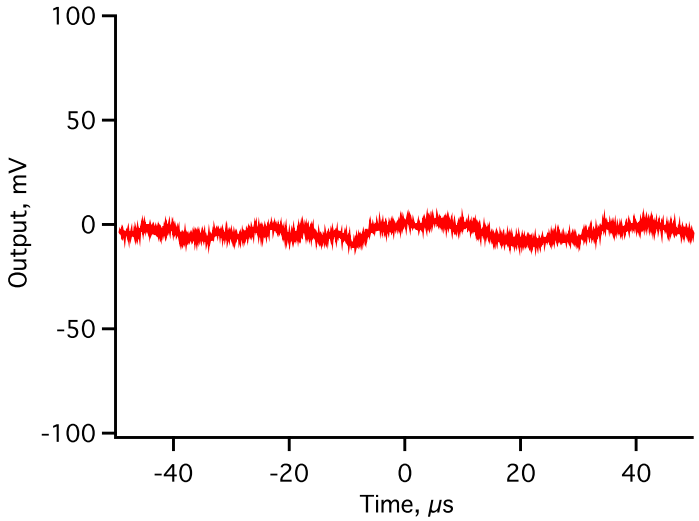

Figure 3.10: **Phase monitor when CEP is locked.** The phase monitor output of the divider box shows the phase error accumulated by f_{ceo} with respect to f_{rep}. When the CEP is locked, there is no cumulative phase error so the output averages to zero. The deviations about zero represent the phase noise of the oscillator.

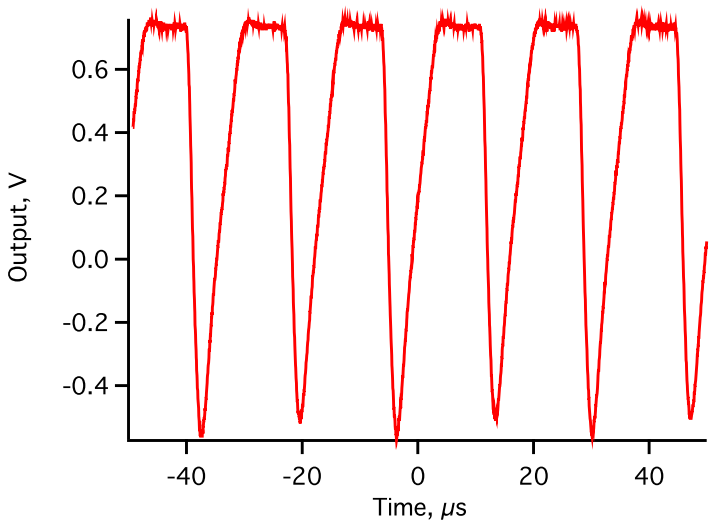

Figure 3.11: **Phase monitor when CEP is unlocked.** When the CEP is unlocked, f_{ceo} is either greater or smaller than f_{rep}, and therefore phase is accumulated linearly with time.

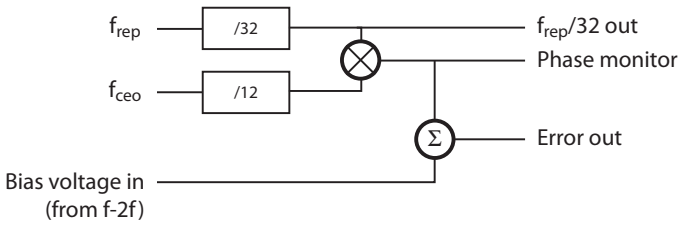

Figure 3.12: **Schematic of phase detector box circuitry.** The two MHz signals from the oscillator are divided down and compared. A bias voltage may be summed with the phase error, which is how the slow CEP locking signal from the f-2f interferometer (see section 3.6) feeds back to the oscillator.

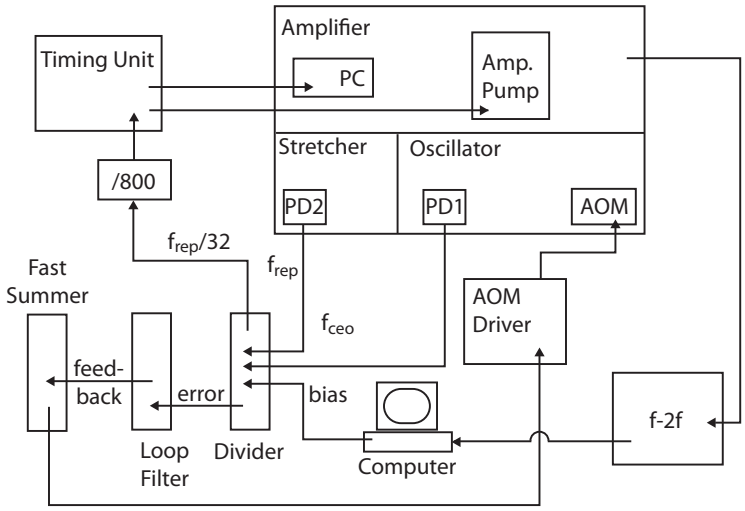

Figure 3.13: **Schematic of the feedback loops stabilizing the CEP.**

required to stabilize the CEP of the oscillator output.

With f_{ceo} locked to $12/32 \times f_{rep}$, every 8^{th} oscillator pulse has exactly the same carrier-envelope phase. To make the pump laser and Pockels cell for the amplifier fire at the right time, they are synchronized to an oscillator-derived TTL signal near 3 kHz. The actual frequency is $f_{rep}/32/800 = 3070\ Hz$, derived by dividing the $f_{rep}/32$ output of the divider box by a factor of 800. This frequency automatically selects every $25,600^{th}$ oscillator pulse, which is a perfect multiple of 8. Alternatively the amplifier may be triggered using a quartz oscillator in the timing box. The timing box also provides the trigger signal to start the time-of-flight detection electronics, discussed in section 3.11.

A schematic of the entire laser control electronics is shown in figure 3.13. The oscillator CEP is stabilized by the fast feedback loop based on the divider box, loop filter, and fast summer as described above. The amplifier CEP drifts more slowly, as discussed in section 3.6, and this drift is corrected by measuring the relative change of the CEP using an f-2f interferometer whose output is fed back to the AOM driver by means of the bias control on the phase detector box.

3.4 Amplifier

The phase-locked oscillator pulses seed a chirped-pulse multipass amplifier (Femtopower Pro) built by Femtolasers, consisting of a stretcher, amplifier, and compressor. The stretcher consists of a glass block, with the third-order dispersion (TOD) compensated using chirped mirrors, shown in figure 3.14. The pulses exit the stretcher with a duration of several picosecond and are injected into the multipass amplifier, where they experience a gain of $\sim$2000 after two passes, and a total gain of $\sim$6000 after 4 passes. A pulse is chosen from the train by a Pockel's cell to be amplified further. The Pockel's cell is triggered so as to

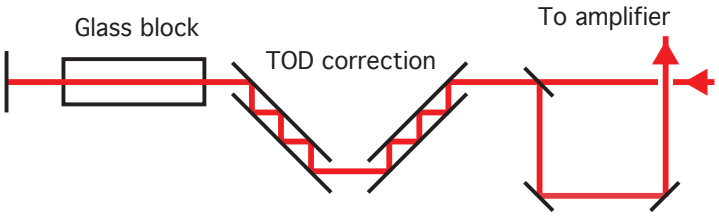

Figure 3.14: **Schematic of the stretcher.** The oscillator output is reflected off E8 and enters the stretcher. The stretcher is composed of two pairs of chirped mirrors and a glass block. As the pulse travels through the glass block, it is stretched by the group delay dispersion of the glass. The glass also contributes unwanted third-order dispersion (TOD), which is corrected by the chirped mirrors.

always pass oscillator pulses having the same CEP. This new CEP-stable 3 kHz pulse train will have a power of ∼800 mW after 8 passes through the amplifier crystal. After the 9^{th} pass, the average power should be no more than 3 W to avoid self-phase modulation and possible damage in the compressor.

The amplified pulses are sent through a prism compressor before exiting the laser. The pulse duration at the exit of the laser is 27 fs, as shown by the interferometric autocorrelation (IAC) trace in figure 3.15. The spectral width—and therefore the duration—is limited by gain narrowing in the amplifier.

Optimization of the amplifier is often much easier than optimization of the oscillator. A schematic of the amplifier is shown in figure 3.16. To align it, use the following steps.

Inject oscillator beam into the first pass The oscillator beam should be steered with the turning mirror after the stretcher so that it is transmitted through the middle hole in the aperture plate A1.

Two-pass gain Insert the mirror into the second pass output and direct this beam off the glass plate into the photodiode. View the diode output on the scope. Iterate changing the turning mirror after the compressor, the injection mirror I1 in the amplifier box, and then the first roof mirror R1 to optimize the signal.

Four-pass gain Move the mirror slightly back until it sends the fourth-pass beam into the photodiode. Optimize the four-pass signal by changing the three mirrors as before, plus the second roof R2. The gain should be a factor of at least 2000, or preferably more like 5000. Remove the mirror from the fourth pass.

Eight-pass gain The power after 8 passes can be monitored by inserting a pick-off mirror before the 9th pass and directing the beam onto a power meter. The power should be optimized using the injection mirror into the first pass I1, the first roof R1, the second roof R2, and the injection mirror into the fifth pass I5, iterating in that order. The power measured should be at least 700 mW. If you can't reach 700 mW, something is wrong with the seed. Check that the mode is good and the divergence is correct.

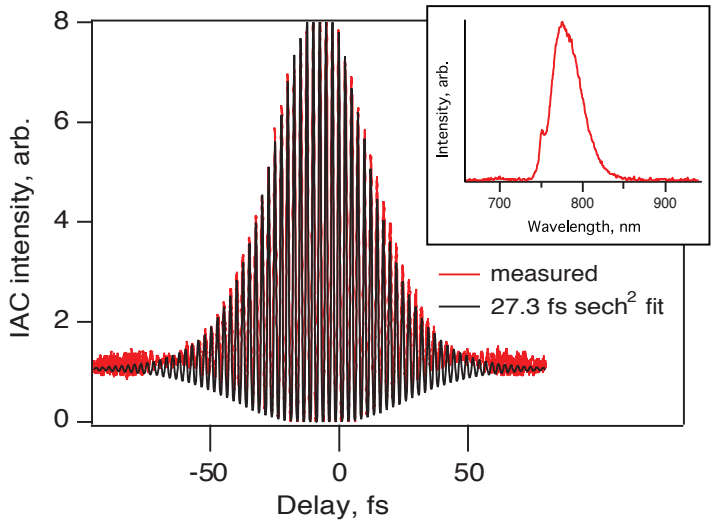

Figure 3.15: **Interferometric autocorrelation of the amplifier output pulse.** The red line shows the measured interferometric autocorrelation of the amplifier output. The black line is a fit to the measured trace, using a 27.3 fs duration sech^2 pulse shape. The inset shows the laser pulse spectrum.

Optimize total output Check the total power. The only adjustment left that you haven't touched is the injection into the 9^{th} pass, I9. Optimize that mirror now.

3.5 External Pulse Compression

The many-cycle pulses provided by the amplifier are shortened to ∼6 fs before harmonic generation. The required bandwidth is achieved by self-phase modulation of the 25 fs laser pulses in a hollow-core glass fiber of 250 μm inner diameter filled with neon gas to a pressure of 2 bar. The fiber is provided by Femtolasers and made of fused silica. The outer diameter is roughly 2 mm. It sits in a triangular groove machined into a 1 m long aluminum bar. The groove depth is approximately 3 mm, so that the fiber entrance sits at the level of the top of the aluminum bar (see figure 3.17). To couple the maximum amount of light into the fiber in the lowest order spatial mode, it is important that the laser focus be located exactly at the entrance to the fiber, and the spot size at the entrance to the fiber be 2/3 the inner diameter of the fiber. To achieve the requisite spot size, the output of the amplifier is focused using an $f = 1.35$ m mirror.

In the fiber, there are two indices of refraction of the neon gas that affect the laser pulse. The first is the usual frequency-dependent index of refraction, which disperses the light. The dispersion of neon at 800 nm is small, but not negligible. The second index by which the laser interacts with the gas is the nonlinear Kerr index, which is an intensity-dependent addition to the regular index of refraction.

The Kerr effect generates a time-varying index of refraction $n(t) = n_0 + n_{kerr} I_0 e^{-(t/\tau)^2}$

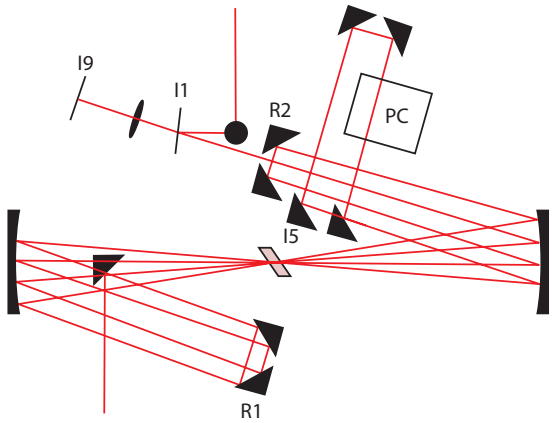

Figure 3.16: **Schematic layout of the amplifier.** The stretched seed pulse from the oscillator is injected into the amplifier from the top of the figure. It travels through a periscope and to mirror I1, the injection mirror for the first pass. after the first pass through the crystal, the pulse is reflected by retroreflector R1 and sent back for another pass. After four passes in this manner, the beam is picked off and sent through the Pockels cell PC, after which it is injected into the fifth pass by mirror I5. The remaining passes are vertically displaced from the first four passes. After the eighth pass, the beam goes under I1, through a telescope, and off I9 for injection into the ninth and final pass through the crystal. The fully amplified beam is then picked off and sent to the compressor.

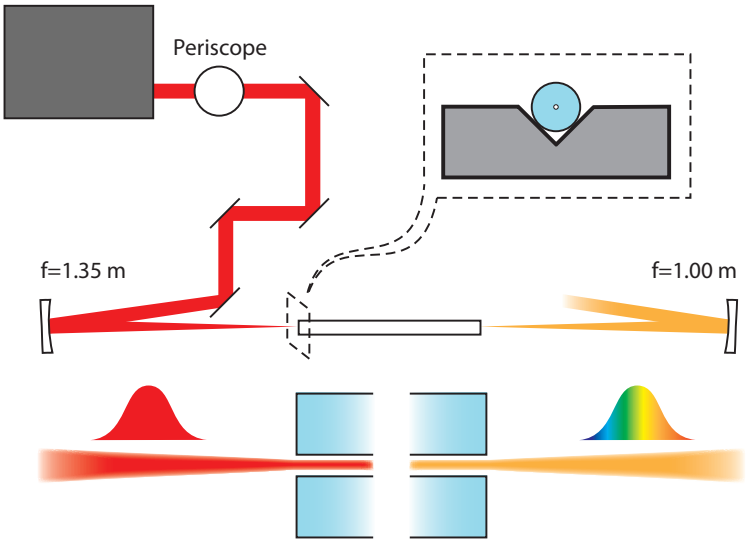

Figure 3.17: **Capillary setup.** The amplified laser output is focused into a 250 μm inner-diameter capillary waveguide, which is supported in a groove milled into an aluminum bar. The capillary and bar are supported in a vacuum-tight lexan tube. The tube is pressurized with $\sim$2 bar of neon gas. The output of the capillary diverges, and is collimated by a focusing mirror.

for a Gaussian pulse. The instantaneous phase of the pulse is then $\phi(t) = \omega_0 t - 2\pi n(t) L/\lambda_0$, with λ_0 the wavelength of the pulse and L the length of the capillary. The frequency is $\omega(t) = \phi'(t)$, which is not simply equal to ω_0, but has a strong component proportional to the time derivative of the intensity envelope of the pulse. Since a Gaussian pulse can be approximated as quadratic near the center of the pulse, the time derivative (and therefore the instantaneous frequency) is approximately linear–the pulse exiting the capillary is both spectrally broadened and positively chirped. The positive chirp is increased slightly by the ordinary index of refraction of the neon gas.

To set up the capillary from scratch, use the following steps.

Establish a beam path Remove the capillary and holder from its mounts. Set it aside on the table or lab bench. Making sure that the alignment helium-neon laser (HeNe) beam is nicely collinear with the infrared, put the HeNe (and therefore the IR beam) on a path that is straight down the table and 4 inches high everywhere. Use an iris to mark the axis of the beam downstream of the intended capillary position.

Insert the capillary Place the capillary tube back in the beam path. The entrance of the capillary should be near the focus of the HeNe. Adjust the capillary mount (NOT the focusing mirror!) so that the HeNe light goes into the capillary. You will see that there is some light coming out the far end of the capillary. This light will disappear if you move the entrance by half a turn on either micrometer screw in either direction. The mode will be terrible but don't worry about that yet.

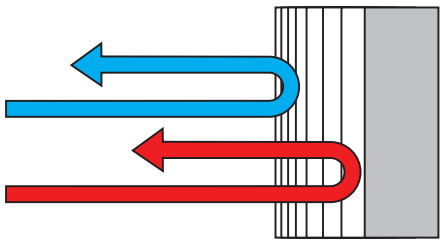

Figure 3.18: **Operation of a chirped mirror.** To provide negative dispersion, a coating is applied to the chirped mirror substrate that is reflective to red light. Then, it is coated over with a coating that transmits the red light but is reflective for blue light. This combination provides a temporal delay between the phase fronts associated with the two colors, thus reshaping the temporal envelope of an incident laser pulse while leaving its spectrum unchanged.

Align capillary axis Use the adjustment micrometers to make the beam exiting the capillary go through the iris you inserted two steps ago, while keeping the light focused into the entrance of the fiber. (The motions of the two X-Y stages that move the capillary are not completely independent, so you will have to move both.)

Maximize throughput Now that the capillary is roughly aligned, you have to optimize it. Again, DO NOT touch the focusing mirror or any optics upstream of the capillary while you are doing this. Take turns walking the micrometers near the rear and then the front so that the throughput is maximum. You will have to use a power meter and the lower-power IR output from the Femtopower to do so. Typical throughput is 50-60%, so if the maximum thorughput you obtain is lower, you will have to move the capillary along the beam axis.

Move capillary along beam axis Since the confocal parameter of the laser focus is about 5 cm, you can move the capillary by 5 mm at a time along the beam axis, then return to the previous step. If the maximum throughput you get decreases, move the other way. When the entrance of the capillary is positioned correctly along the beam axis, the mode of the output should be nice and round and the throughput should be around 60%. Remember that the laser self-focuses in the neon gas when the power is high, which effectively moves the optimal capillary position upstream by a couple of millimeters for the high-power laser beam.

The output of the capillary diverges from a focus the size of the confined beam in the waveguide. It is collimated by an $f = 1$ m mirror and sent to the chirped mirror compressor. This compressor is made from dispersive dielectric mirrors. The operating principle of the mirrors (figure 3.18) can be thought of in the following way: red light arrives at the mirror surface first, since the pulse exiting the capillary is positively chirped. The layers of dielectric

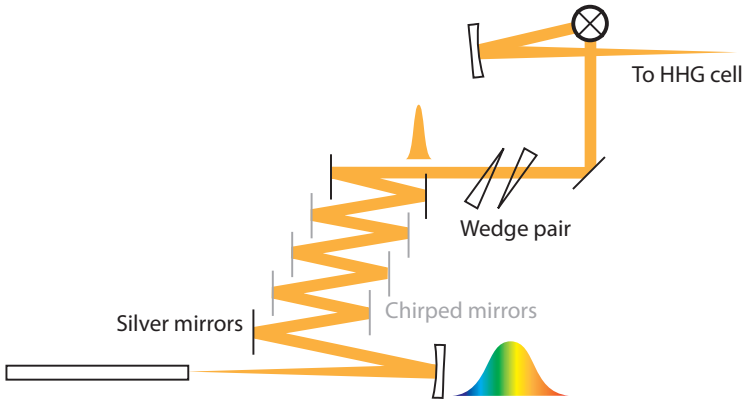

Figure 3.19: **Layout of the optical table after the capillary.** The collimated capillary output is strongly positively chirped, so it is directed to a series of three matched pairs of chirped mirrors. These slightly overcompensate the chirp, so a pair of glass wedges are inserted after the chirped mirror compressor to fine-tune the dispersion. A periscope brings the beam height up to that of the harmonic generation cell and a focusing mirror directs the laser into the cell.

coating that reflect red light are buried deep in the mirror, so that the red light takes a long round trip into the mirror surface and back out. By contrast, the layers that reflect blue light are on the surface of the mirror, so blue light takes a short path off the mirror. Thus the trailing blue light catches up with the red light after several bounces off of chirped mirror surfaces. It is important to always use matched pairs of chirped mirrors, because the spectral phase imprinted on the laser pulse by one chirped mirror is not exactly quadratic–it has ripples about the overall quadratic shape. The matching mirror in the pair is manufactured to have ripples in the opposite sense, so that the ripples of the pair cancel and pure negative dispersion is the result.

The layout of the optical table between the capillary exit and the harmonic generation cell is shown in figure 3.19. Compensation of the phase of the laser light using chirped mirrors provides a few-cycle pulse, as shown by autocorrelation (figure 3.20).

3.6 Slow-loop CEP locking

The broadened spectrum of the few-cycle pulses generated in this manner allows easy implementation of an f-2f interferometer to monitor and correct the CEP of the pulses exiting the amplifier. A leak through the first chirped mirror is focused into a BBO crystal where the long-wavelength portion of the spectrum generates second harmonic light. The spectral interference pattern between this SHG light and the short wavelength region of the

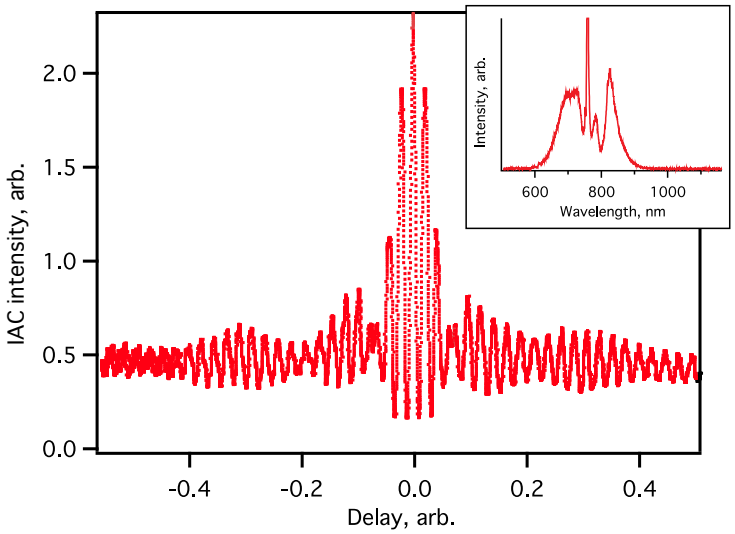

Figure 3.20: **Interferometric autocorrelation of the HHG driver pulse.** The harmonic generation driving pulse is about 6 fs long, as shown by the interferometric autocorrelation. The inset shows the spectrum of the pulse.

fundamental indicates the CEP.

More specifically, consider a fundamental field with spectral phase $\phi(\omega) + \phi_{CEP}$. When this fundamental field is doubled, the spectral phase of the blue light has a new spectral phase function $\phi'(\omega) + 2\phi_{CEP}$. If there is overlap between the two spectra, the combined spectral intensity contains a cross term proportional to the cosine of the phase difference: $I(\omega) \propto const. + cos(\phi'(\omega) - \phi(\omega) + \phi_{CEP})$. The fringe pattern in the spectrum will be sensitive to both the spectral phase of the fundamental pulse and the CEP. If the CEP changes while the spectral phase of the fundamental stays constant, it is evidenced by a shifting of the fringe pattern in the spectrum.

The spectrum is read out by a computer at approximately 25 Hz. The relative CEP is extracted using a Fourier transform and reverse transform–the inverse transform yields the amplitude and phase–the relative CEP–of the cosinusoidal signal in the spectrum. This is the input for a PID loop, whose control parameter is an offset voltage sent via a digital-to-analog converter to the divider box (see section 3.3), and from there to the oscillator AOM driver. Since the readout rate for the CCD camera is about 25 Hz, the bandwidth of the loop is somewhat less–around 10 Hz. When the loop is switched off, the variations of the relative CEP fall below roughly 1 Hz. Therefore the bandwidth provided by the video-framerate camera is more than sufficient.

There are two ways to extract light from the amplifier beam to read out the relative CEP. The first, described above, is to use the output of the hollow core fiber, which is octave-spanning and therefore simply needs to be focused into a BBO and the output light analyzed. Since the chirped mirrors do not have perfect reflectivity, the leak through the first one can be used as the input for a simple f-2f interferometer. This technique is convenient because light is not wasted–the power sent to the interferometer was lost anyway. But it

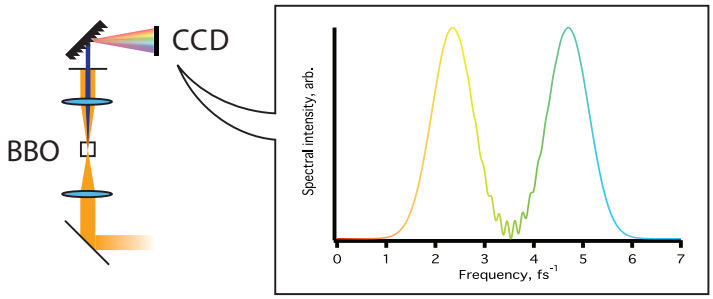

Figure 3.21: **f-2f interferometer.** Some broadened light from the capillary output or from self-phase modulationin a sapphire plate is focused in a BBO crystal to generate second harmonic light and the output recorded by a spectrometer. At the region of spectral overlap, the two pulses interfere with a fringe pattern whose offset corresponds to the carrier-envelope phase of the input pulse. The absolute carrier-envelope phase cannot be determined in this way, because the fringe pattern is also sensitive to the spectral phase of the input pulse. However, relative changes in the carrier-envelope phase can be measured.

has a major downside as well. Since the fringe pattern depends not only on the CEP but also on the spectral phase of the input pulse, changes in the capillary output phase are indistinguishable from changes in the CEP, which can lead to spurious "corrections" sent to the AOM driver. The problem is not only power fluctuations of the amplifier but also pointing fluctuations influence the amount of light coupled into the capillary and therefore determine the spectral phase noise and apparent CEP drift. These fluctuations need not be fast; they occur within the loop bandwidth as well.

To avoid using the capillary output for the input of the f-2f, a portion of the fundamental beam is split off using a glass plate that is anti-reflection coated on one side. The plate is mounted near Brewster's angle since no more than 1% of the full beam power is required for the f-2f interferomenter. The light is focused into a sapphire plate, the resulting spectral continuum collimated, and this is used for the input of the f-2f. While this technique still relies on self phase modulation and therefore is still sensitive to power fluctuations, it is insensitive to pointing fluctuations (as long as they are not so big as to move the beam clean off the sapphire plate). It has the disadvantage that ∼1% of the fundamental light is lost before the capillary.

3.7 HHG

The CEP-locked, few-cycle pulses are used to generated high-order harmonics by focusing them with an $f = 50$ cm mirror into a 1/8 inch gas cell filled with rare gas, either neon or argon.

In harmonic generation, an intense laser pulse ionizes the target atoms by field ioniza-

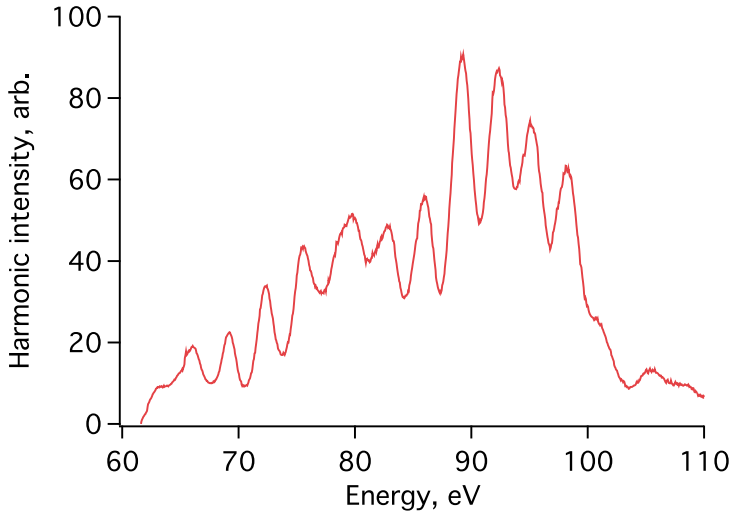

Figure 3.22: **Typical HHG spectrum.** In this harmonic spectrum the separation of peaks by twice the laser photon energy is clearly visible. This spacing results from the periodicity of the harmonic generation process. This spectrum was generated in neon gas with a 6 fs driver pulse. The peak intensity of the driver pulse was $7{\times}10^{14}$ W/cm^2.

tion, then accelerates the resulting free electrons through the continuum. The electrons can recombine with the parent ions when the laser field direction reverses, releasing x-rays. This process repeats every half cycle of the laser pulse, so there is a modulation in the HHG spectrum at twice the laser frequency. This ∼3 eV spacing is clearly resolved in a typical experimental HHG spectrum shown in figure 3.22.

The geometry of the harmonic generation cell is critical to the performance of the x-ray conversion process. The cell used in the experiments here is a 1/8 inch (3.2 mm) inner diameter. It has milled flats on the entrance and exit sides, so that the external width of the cell is 3.5 mm. The outer diameter of the tube is 1/4 inch, and it is connected to the gas supply by a swagelok ocnnector and a polyethylene tube. The cell has two ∼400 μm holes drilled in it (#78 drill bit), exactly opposite each other, to let the driving laser beam through. Figure 3.23 shows a drawing of the cell.

The cell is positioned by an x-y-z stage in the vacuum chamber several millimeters after the focus position of the laser, to select the short trajectory harmonics. The cell position relative to the focus of the laser is not routinely measured; rather, the relative cell position along the z-axis of the three-axis stage is measured by a ruler glued to the stage.

The peak intensity on axis in the harmonic cell is about 7×10^{14} W/cm^2. The pulse duration, as mentioned above, is about 6 fs. Therefore, the ionization of the neutral neon gas reaches the few-percent range by the end of the laser pulse. Phase matching of the harmonic conversion process demands that the pressure of the neutral gas be tuned so that its positive dispersion balances the negative dispersion of the plasma. The geometry of the cell also affects the phase matching; see chapter 6 for more details on phase matching. In any case, typical pressures for phase matching harmonic generation in argon are around 7 torr,

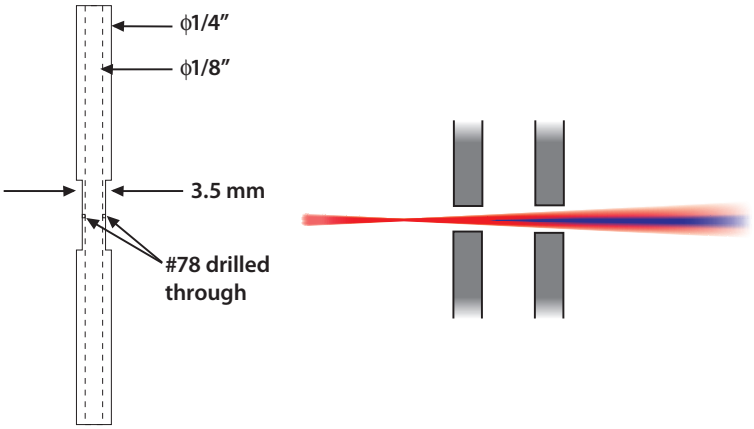

Figure 3.23: **harmonic generation cell.** The cell is made from a length of stainless steel tubing of 1/4 inch outer diameter and 1/8 inch inner diameter. The bottom of the cell is glued shut and the top is connected to a gas supply line with a swage connector. Two flats are milled in opposite sides of the cell so that the thickness is 3.5 mm. Holes are drilled with a #78 drill bit to allow the laser beam to pass through. The cell is placed slightly after the focus, as shown on the right, so that the driver laser is slightly diverging as it travels through the cell.

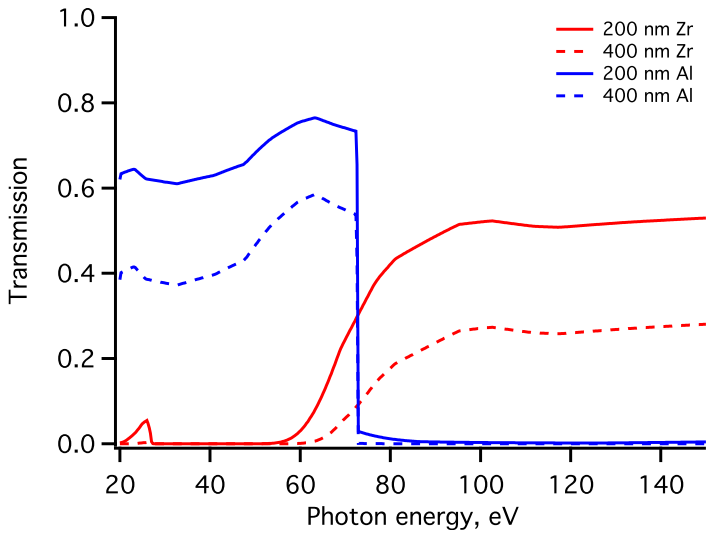

Figure 3.24: **Metal filter transmission.** The solid lines correspond to 200 nm thickness metal foil, the dashed lines to 400 nm thickness. Red lines show the transmission of zirconium filters while blue lines show the transmission of aluminum filters.

while for neon the pressure should be around 40 torr. The pressure in the harmonic cell is determined by a leak valve inserted in the line directly from the regulator on a 5000 L tank. The regulator pressure is just over 1 atm absolute pressure, or just above zero gauge pressure.

3.8 XUV Spectrometer

The first element of the spectrometer is a movable filter holder, which can hold four different combinations of metallic foil filters. These are typically Al foil for harmonics from argon (20 to 70 eV range) and Zr for harmonics from neon (60 to 150 eV range). The 200 nm thick filters are purchased from Lebow Company and come pre-mounted on metal support rings. The transmission curves for the various filters are shown in figure 3.24. 30 cm downstream from the filters is a 500 μm wide slit through which the x-ray beam passes, followed by a transmission grating of 10,000 lines/mm provided by nm^2 llc. The transmission grating material is 100 nm thick Si_3N_4, which transmits as shown in figure 3.25.

The dispersed light from the grating travels to a Princeton Instruments x-ray CCD camera (Pixis XO 400B) 25 cm downstream. The chip is 26.8 mm wide, so the full dispersed spectrum is not available at one camera position. Therefore, the camera is mounted on a bellows so that it can be moved between zero order and first order positions by displacing it laterally. For measuring the harmonic spectra produced with argon gas, the grating is tilted at an angle of $\alpha = 10°$ to the incoming x-ray beam to move the argon harmonic positions onto the chip. The grating equation $\lambda/d = sin(\theta) + sin(\alpha)$, with d the grating spacing, predicts the harmonic positions on the CCD. Coupled with the slit width, the resolution can also be calculated. The harmonic position and wavelength-dependent resolution are shown in figures

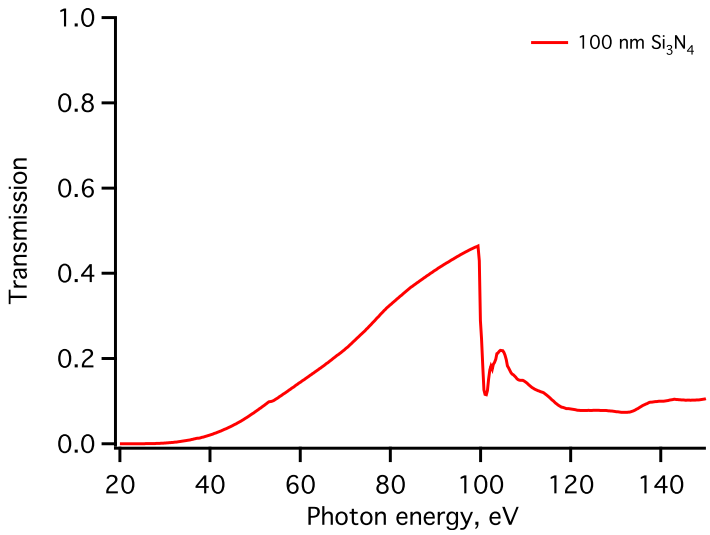

Figure 3.25: **Grating material transmission.** The transmission of 100 n thickness of silicon nitride is shown as a function of photon energy. The pronounced dip near 100 eV is a result of the silicon L edge, and is visible in harmonic spectra generated with neon gas. It can be used for calibration along with the Al filter cutoff near 70 eV.

3.26 and 3.27 for the cases of neon ($\alpha = 0°$) and argon ($\alpha = 10°$) harmonics, respectively. The spectrometer geometry is illustrated in figure 3.28.

3.9 Multilayer mirrors

The x-ray beam may be reflected back into the interaction region of a time-of-flight mass spectrometer by an x-ray mirror. In the soft x-ray region of the spectrum, absorption is very strong and refraction is almost nonexistent. As a result, there are basically three types of x-ray mirrors: reflective, operating at grazing incidence; diffractive (crystalline); and multilayer mirrors, which are also diffractive. For operation at normal incidence, diffractive optics are the only choice. Since diffraction requires a structure with spacing similar to the wavelength of the light, atomic crystals do not work for the soft x-rays generated by high harmonic generation (wavelength >10 nm). However, structures composed of thin, stacked layers of material can effectively diffract an incoming soft x-ray beam. These are called multilayer mirrors, and they are typically composed of alternating layers of dielectric and metal. Each interface backscatters some light, and if the wavelength matches the multilayer period, the individual scattered beams interfere constructively. Reflectivities on the order of tens of percent may be achieved in this manner, using layers of Mo and Si, Mg and SiC, or Al and Zr.

Figure 3.29 shows how the reflectivity of a mirror composed of 9 nm layers of Mo and Si varies with the number of layers. It is seen that the smaller the number of backscattering periods, the lower the peak reflectivity and the broader the wavelength response. Since the layer thickness is 9 nm, the peak reflectivity occurs near the multilayer period, or 18 nm.

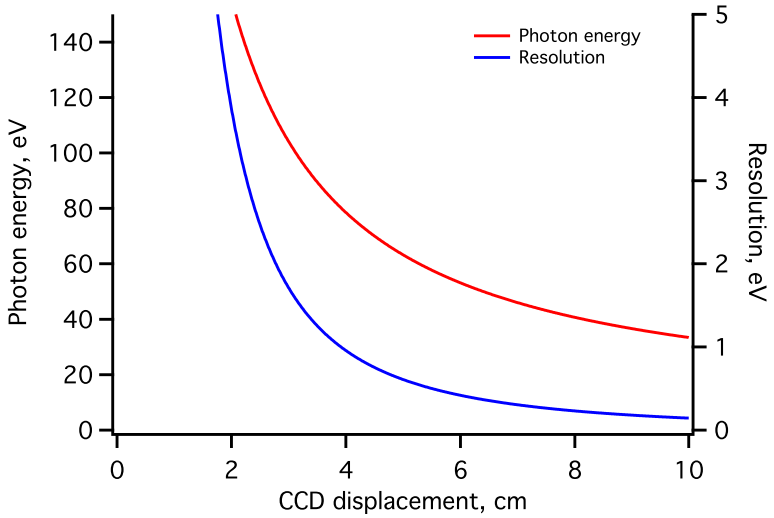

Figure 3.26: **Calculated spectrometer performance for high harmonic generation in neon.** The grating is oriented normal to the incoming harmonic beam. The resolution (blue) is calculated by multiplying the slope of the dispersion curve (red) by the slit width of 500 μm.

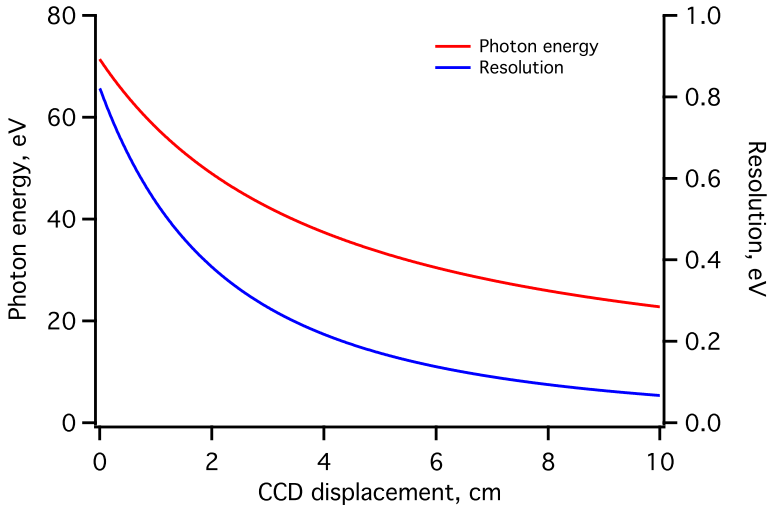

Figure 3.27: **Calculated spectrometer performance for high harmonic generation in argon.** When the grating is tilted by 10° with respect to the incoming harmonic beam, the lower-order harmonics are brought nearer the beam axis (red). The resolution (blue) is calculated as for figure 3.26.

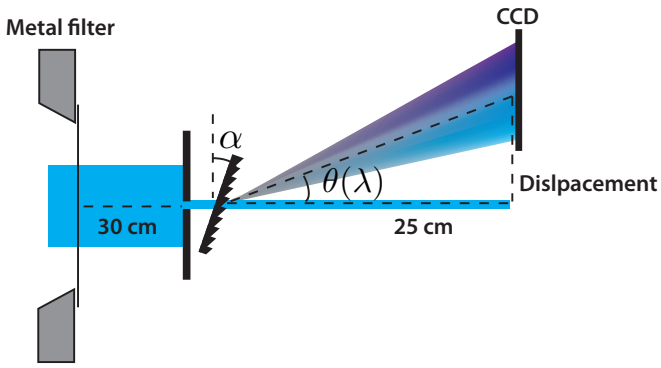

Figure 3.28: **Geometry of the x-ray spectrometer.** The x-ray beam enters the spectrometer where residual driver laser light is filtered out by a metal foil. 30 cm downstream, the beam is clipped by a 500 μm wide slit, mounted vertically. 5 mm after the slit, the beam is diffracted from a transmission grating which is oriented at a variable angle α to the incoming beam axis. α is generally zero for neon harmonics and 10° for argon harmonics. The wavelength-dependent diffraction angle $\theta(\lambda)$ is determined by the grating equation. 25 cm past the grating is an x-ray CCD camera mounted on a bellows. It can be displaced horizontally by up to several centimeters to observe the diffracted x-ray light.

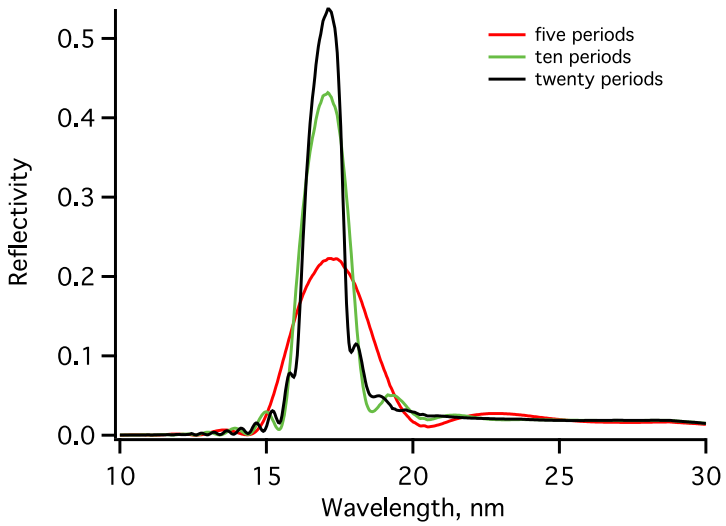

Figure 3.29: **Calculated MoSi mirror reflectivity** The reflectivity of a molybdenum/silicon multilayer mirror versus wavelength for three numbers of Mo:Si periods: five, ten, and twenty. As the number of periods increases, so increases the number of coherent backscattered waves that interfere constructively. The reflectivity increases, but so does the wavelength discrimination.

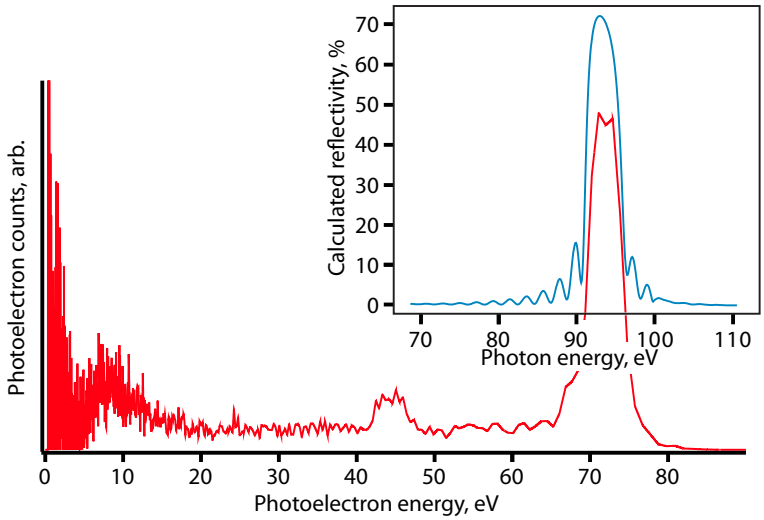

Figure 3.30: **Calculated MoSi mirror reflectivity and experimental photoelectron spectrum** The experimental photoelectron spectrum of Ne shows strong emission from the $2p$ level at about 72 eV and weaker emission from the $2s$ level at 45 eV. When corrected for the ionization potential of neon, 21.6 eV, the experimental photoelectron kinetic energy is precisely as expected for the x-ray mirror employed, which is reflective at 93 eV with a 4 eV bandwidth (calculated reflectivity, inset).

The calculated reflectivity curve and a photoelectron spectrum for the mirror used in the chapter 6 is shown in figure 3.30. The mirror has a nearly 70% peak reflectivity centered at 93 eV with a 4 eV bandwidth. The shortest attosecond pulse this mirror can support is therefore 450 as.

Multilayer mirrors are also reflective in the visible region of the spectrum. The reflectivity and phase of the mirror are shown in figure 3.31 as a function of visible wavelength. The reflectivity is above 50% across the entire spectrum. Since there are no absorption resonances in the visible or UV region, we expect that the phase is flat across the visible region. This expectation is borne out by the reconstruction of the laser pulse electric field in chapter 6. Therefore the multilayer mirrors are also very useful in vacuum for steering and focusing the visible light left over from the HHG process without inducing phase distortions.

The surface quality of the multilayer mirror substrates is critical to their performance. Substrates must be superpolished to 1 Å root-mean-square surface roughness to avoid scattering much of the reflected x-ray light. Scattered x-rays on paths near the interaction region of the time-of-flight spectrometer are a major problem since they decrease the effective spatial overlap of the x-ray beam and the probe infrared beam. 10 Å RMS roughness mirrors scatter 10% or more of the incoming radiation, while optical substrates intended for visible light are totally unusable. By contrast, the surface figure is not as critical, but still important. The common specification for surface figure of $\lambda/20$ at 632 nm corresponds to a displacement of the mirror surface of about 200 attoseconds, roughly ten times the spherical

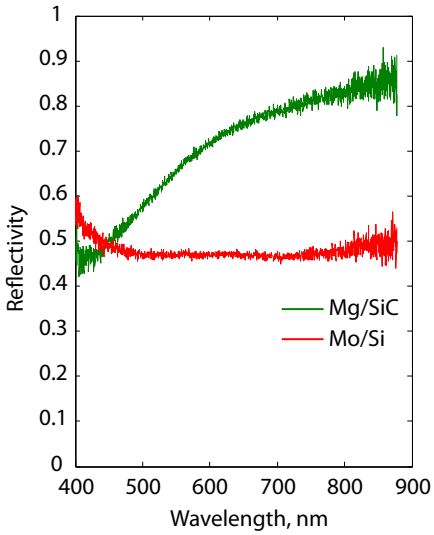

Figure 3.31: **Measured reflectivity of multilayer mirrors in the visible region.** The reflectivity was determined by comparison of the spectra reflected white lamp light from a silver mirror and from the multilayer structure.

aberration experienced by a 1 cm wide beam falling on our 12.5 cm focal length optics.

3.10 Separation of pump and probe beams

For a time-resolved experiment the pump and probe beams must be delayed with respect to one another. Since there are no refractive optics in the XUV region, and the overall number of reflections of the harmonic beam should be minimized to maintain as high a flux as possible in the interaction region, the spatial separation of the harmonic and infrared light after the harmonic generation cell must take advantage of the relatively low divergence of the harmonic beam. This is generally a few mrad compared to the infrared divergence angle of about 20 mrad. The temporally overlapped infrared and XUV pulses travel coaxially to a metal filter glued to the middle of a 5 μm thick nitrocellulose pellicle supplied by National Photocolor. The pellicle transmits the infrared with an index of refraction of 1.5, while blocking any harmonic light that falls on it. The harmonic light is transmitted through the metal filter (which can be Al or Zr) in the middle of the pellicle, while the infrared light is blocked. The arrangement is illustrated in figure 3.32.

The inner beam, consisting of harmonic light transmitted by the metal filter, proceeds to a multilayer mirror of 3 mm diameter. The outer beam travels to a donut-shaped mirror of inner diameter 3.5 mm and outer diameter 1 inch, mounted coaxially with the small inner mirror. As mentioned above, the focal length of both mirrors is 12.5 cm. The mirrors focus the light pulses into the interaction region of a time-of flight spectrometer. The inner mirror is mounted on a piezoelectric translation stage giving nanometer control over its displacement along the optical axis and therefore attosecond delay control. Turning of the outer mirror,

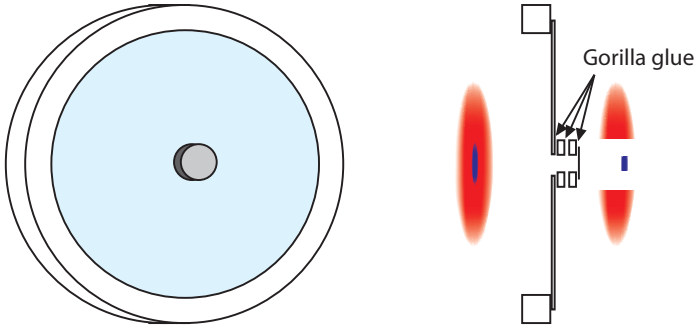

Figure 3.32: **Pellicle used to separate IR and XUV light.** The nitrocellulose pellicle will dissolve in most glues; therefore gorilla glue is used to affix a washer to the pellicle. A second washer with a metal foil glued on is then fixed to the pellicle.

and turning of the entire split mirror assembly, is achieved by picomotors.

After the experiments in chapters 5 and 6 were performed, the beam splitter was re-designed to eliminate the split mirror assembly. The beam splitter and delay apparatus is now based on mirrors with holes drilled in them.

The laser beam comes first to a 45° turning mirror with a 9 mm hole drilled through the center. The middle portion of the beam is transmitted, while the annular outer portion is reflected. The inner portion is used for harmonic generation, while the outer portion is preserved for use as the probe beam in the interaction region. The HHG driver beam is put through 1 mm of glass to give it approximately a 1 ps delay relative to the probe beam. The delay is fine-tuned by a piezoelectrically actuated retroreflector in the HHG driver arm of the interferometer. The probe and HHG driver beams are recombined by another 45° turning mirror with an identical 9 mm hole. The probe pulse is transmitted through the harmonic cell first, when there is as yet no plasma, thus preserving its temporal and spatial structure. The delayed HHG driver pulse follows 1 ps later, generating plasma and harmonic light.

The pellicle is now replaced by a 1 mm glass plate, so after the harmonic cell the probe beam suffers a 1 ps delay to overlap it in time with the harmonic pulse. The HHG beam is blocked by a thin metal foil (200 nm of Al for argon harmonics, and 200 nm of Zr for neon harmonics) while the x-ray light is transmitted. Downstream of the filter is a multilayer mirror that is reflective for the x-rays and the visible light. The relative positions of the two foci are controlled externally to the vacuum by fine adjustment of the recombination mirror. The overall interferometer setup is shown in figure 3.33 along with a schematic showing the timing of the various pulses as they travel through the setup.

The jitter of the interferometer is measured to be 150 mrad RMS at 632 nm, or about 50 as.

Alignment of the interferometer is accomplished in the following way.

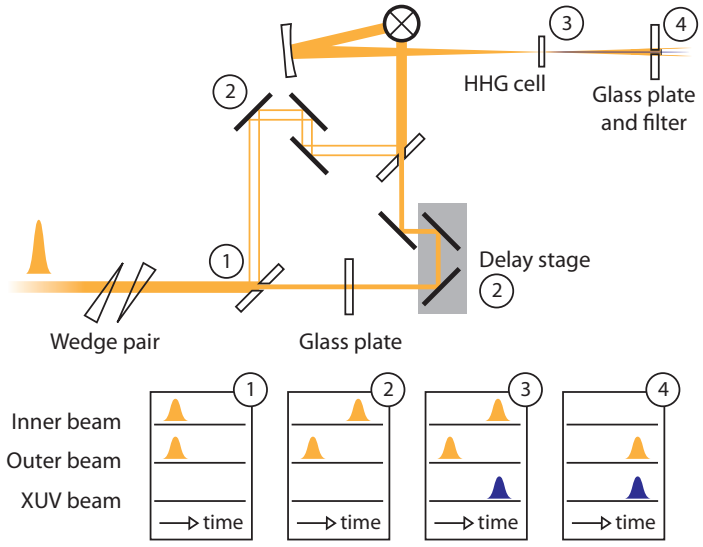

Figure 3.33: **Interferometer based on drilled mirrors.** The incoming laser beam is split into inner and outer portions with a hole-mirror (1). Both portions of the pulse are still synchronized. The HHG arm of the interferometer has a glass plate in it, delaying the HHG driver pulse with respect to the probe pulse (2). The beams are recombined and sent through the HHG cell, where harmonics are generated from the HHG driver beam (3). The HHG driver beam is blocked by a metal foil filter which transmits the harmonic light with negligible group delay. The outer probe beam is transmitted by the glass support for the foil, which delays it to be in time with the harmonic pulse (4). The relative timing can be adjusted by a delay stage in the HHG arm of the interferometer.

Bring laser onto hole-mirrors Walk the laser so that the spot is centered on both the hole-mirror holes. You can check the beam profile of the reflected beam from the first hole-mirror to make sure that it is circularly symmetric.

Match beam axes Using a card on the second hole mirror, double check that the inner beam comes through the middle of the drilled hole. Make sure that the outer beam is centered about the hole by adjusting the first turning mirror in the outer beam path. This will result in a rotationally symmetric beam profile after the mirror. Check the beam profile near the harmonic focusing mirror–the two beams should be coaxial here too. If they are not, adjust the second drilled mirror to make sure they are. Now the beams are close to coaxial.

Find spatial overlap The easiest way to find spatial overlap is to place a video camera in the focus of the low power laser beam and adjust the steering of the second hole mirror to make the two foci overlap. To do this, first attenuate the low power amplifier output by placing an OD4 neutral density filter in the beam. Insert a turning mirror after the harmonic focusing mirror directing the beam away from the vacuum chamber. Place a video camera in the focus and overlap the two spots, adjusting the position of the outer beam focus by turning the second hole mirror. An alternative method for finding spatial overlap is to place a piece of tinfoil in the focus of the outer beam (you will hear it whine at 3 kHz as you move it close to the intense focus) and use the laser to burn a pinhole there. Without moving the tinfoil, send the outer beam through the hole using the second hole mirror. Because the inner beam focus is much smaller than the outer beam focus, this technique significantly clips the outer beam in the focus and as a result the outer beam leaving the tinfoil is no longer annular, but more-or-less Gaussian.

Find temporal overlap Finding temporal overlap is most easily achieved by placing a fiber-optic spectrometer probe (from the Ocean Optics HR4000 spectrometer) in the beam after the pinhole drilled in the previous step. You should see the total power in the spectrum dip as you block the two arms of the interferometer one by one. Make sure the group delay is balanced between the two arms–you will have to remove the glass plate. Now, adjust the micrometer to coarsely tune the interferometer delay. When you see fine fringes start to appear in the spectrum, you are close. Move the micrometer to minimize the fringe period (maximize the spacing). This is time zero, to within several fs. Now if you put the glass back in and observe the spectrum again, the fringe spacing decreases dramatically. That's why you take the glass out to find overlap: If you don't, you'll be a picosecond off.

3.11 TOF spectrometer

The harmonic and leftover visible light are refocused to the interaction region of a time of flight (TOF) photoelectron spectrometer by a split multilayer mirror consisting of a circular 3 mm diameter inner mirror and an annular outer mirror with inner diameter 3.5 mm and outer diameter of one inch. The focal length of the mirrors is 12.5 cm. The foci of the

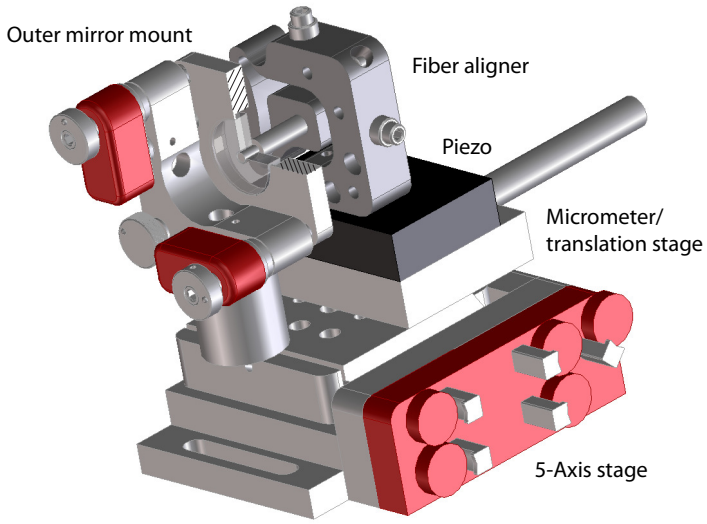

Figure 3.34: **Split mirror setup in vacuum, with cutaway view.** The interferometer consists of two concentric mirrors, one round and one annular (shown cutaway to reveal the inner round mirror). The round inner mirror is mounted by means of a fiber aligner and piezo-electric translation stage, while the outer annular mirror is mounted using a motorized 1" mirror mount (also shown with cutaway view). The delay can be coarsely adjusted using a micrometer-driven translation stage, while the piezo stage controls the fine (attosecond) delay. The outer mirror may be steered relative to the inner mirror using the motorized mirror mount, while both foci may be moved together by adjusting the 5-axis tip/tilt/translation stage.

mirrors can be moved independently using the controls for the mirror stack shown in figure 3.34.

With the foci in the interaction region, photoelectrons are generated in a target gas and detected by the TOF spectrometer. Those photoelectrons going upwards into a solid angle of 2.4×10^{-4} sr hit a multichannel plate detector. The detector has an active area of 40 mm diameter and the flight tube is 650 mm long. The raw output of the detector is capacitively coupled out and passed through a 10x preamplifier. After the amplifier, the negative-going pulses vary in amplitude roughly from 10 mV to over 200 mV. The pulse height distribution $p(h)$ from 30 mV onward is shown in figure 3.35, and it fits an exponential function

$$p(h)dh \propto exp(-h/\tau)H(h-T)dh \tag{3.1}$$

with h in mV, $\tau = 33$ mV and H the Heaviside function shifted by the detection electronics threshold T. Using a Gaussian voltage pulse shape with standard deviation σ, the probability of the voltage crossing the threshold T (and therefore of a particle being detected) at an apparent time t can be calculated. It is:

$$p(t)dt \propto exp(-h(t)/\tau)H(h(t)-T)h(t)tdt, \tag{3.2}$$

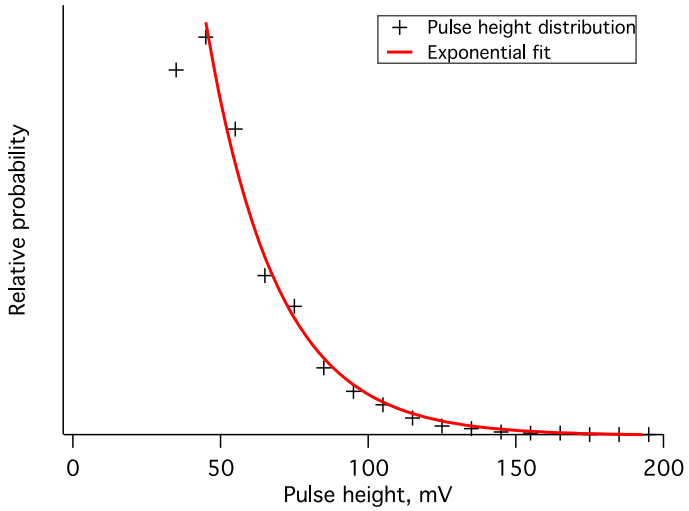

Figure 3.35: **Pulse height distribution of the MCP detector.** The relative probability $p(h)dh$ that an electron hit on the detector will register a voltage pulse of height h is plotted (crosses) along with an exponential fit (red line).

or, since

$$h(t) = \frac{T}{exp(\frac{-t^2}{2\sigma^2})}, \tag{3.3}$$

$$p(t)dt \propto exp(-T/exp(\frac{-t^2}{2\sigma^2})\tau)H(\frac{T}{exp(\frac{-t^2}{2\sigma^2})} - T)\frac{T}{exp(\frac{-t^2}{2\sigma^2})}tdt. \tag{3.4}$$

The distribution of arrival times is plotted in figure 3.36 using the experimental pulse shape to extract $\sigma \simeq 1.7$ ns and using a threshold of $T = 30$ mV.

Not only do the pulse heights vary widely, but the temporal structure of the pulse varies from hit to hit. This is illustrated in figure 3.37, showing two oscilloscope traces of individual electron hits. The sometimes-poor structure of the voltage pulse may be a result of imperfect impedance matching in the detection electronics.

A constant fraction discriminator (CFD)after the preamplifier makes the pulse height a uniform -2 V p-p, and the dead time of the CFD also makes it possible to lower the detection threshold so that all the hits are counted without worry of counting a double hit as a result of a particularly poor peak structure. Finally, the CFD removes the (up to) 3 ns jitter in apparent electron arrival times caused by the pulse height distribution of the MCP. This is particularly important given that the flight time for a 70 eV electron is only about 130 ns. A block diagram of the signal recovery electronics is shown in figure 3.38.

The overall experimental setup is designed to deliver sub-fs x-ray pulses, and to detect their effects on gas-phase atoms and molecules. Performance of the experimental setup is strongly dependent on the performance of the laser, and therefore laser pulse diagnostics are also an integral component of the lab's operation. The techniques used for characterizing visible laser pulses are discussed in chapter 4.

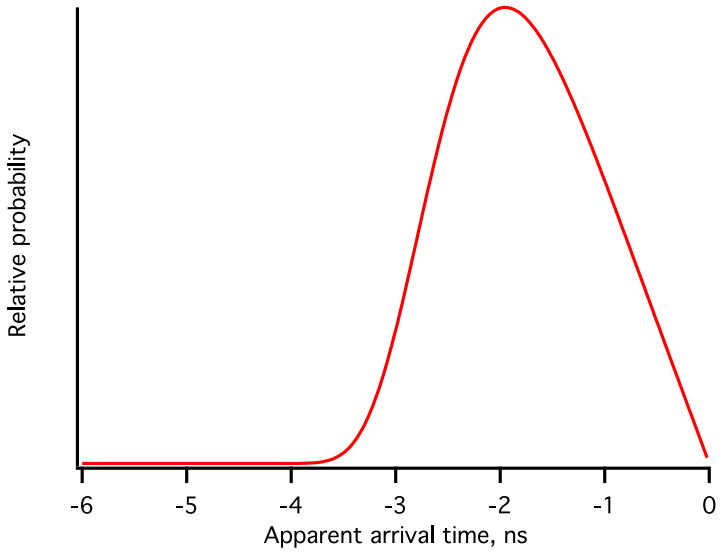

Figure 3.36: **Apparent arrival time distribution given the experimental parameters.** Since pulses with higher peak height seem to arrive early, the distribution of apparent arrival times is not simply a delta function centered at the actual arrival time. It is instead a function of the threshold used to detect the pulses, the pulse height distribution, and the pulse duration.

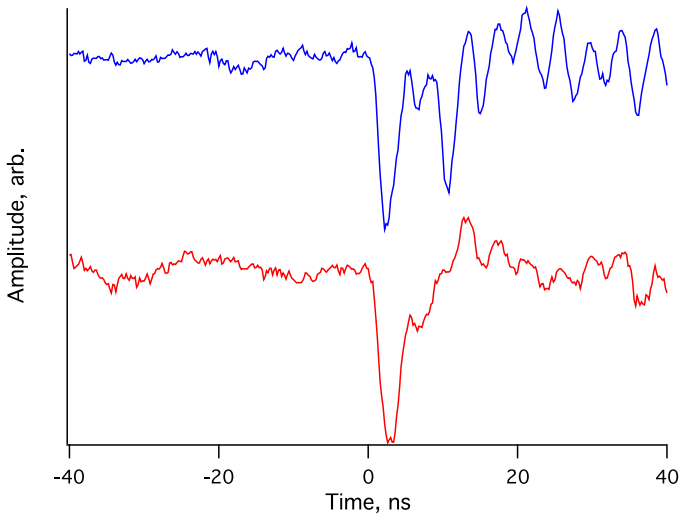

Figure 3.37: **Two typical electron hits recorded by the MCP.** The structure of the voltage pulses coming from electron hits on the MCP is highly variable.

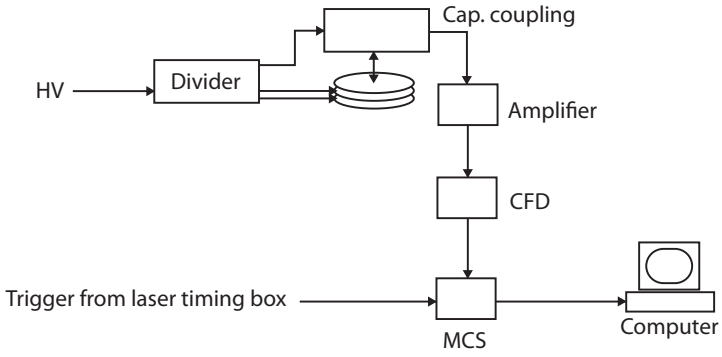

Figure 3.38: **Schematic of signal recovery electronics.** Electronics for operation of the time-of-flight detector.

Chapter 4

Visible Pulse Characterization

4.1 Introduction to pulse characterization

As demonstrated in chapter 2, the requirements on the HHG driver pulse are quite severe if one desires to generate an isolated attosecond pulse. The duration of the driver must be very short and the intensity must be very high. Ionizing pre- and post pulses cannot be tolerated. As a result, accurate characterization of the driver pulses is a requirement for successfully implementing attosecond pulse production.

Since there is no detector fast enough to directly capture the ultrafast evolution of the driver pulse intensity, we rather compare the pulse to be measured *to itself*. There are many such self-referencing techniques for ultrafast laser pulse characterization. The easiest and most common is interferometric autocorrelation (IAC), which is used as a routine check on the pulse duration. Despite (or perhaps, because of) its simplicity, the utility of IAC is limited and for precise and detailed characterization of few-cycle laser pulses SPIDER is used instead. SPIDER is much harder to use, but gives much more detailed information about the temporal structure of the laser pulse. Both these techniques are addressed in order below.

4.2 Interferometric autocorrelation principle of operation

In IAC, the pulse to be measured is split into two copies with variable delay, and then focused into a nonlinear crystal. The second harmonic amplitude produced is proportional to the square of the combined field of the two pulse copies, and the intensity is proportional to the square of the amplitude. The detector measures the total amount of blue light: it effectively integrates over time. Therefore, $I(\tau) \propto \int |(E(t) + E(t-\tau))^2|^2 dt$. This output is shown in figure 4.2 for a 5 fs pulse with 800 nm wavelength. The output $I(\tau)$ is an even function of τ. This means that the autocorrelation trace can be quite poorly reflective of the actual pulse shape in the event that there are significant distortions from the pulse's transform limit.

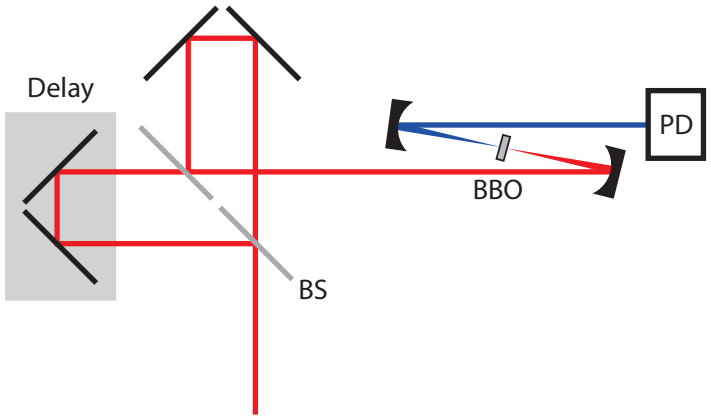

Figure 4.1: **Autocorrelator.** BS: beamsplitter. BBO: nonlinear crystal. PD: photodetector. Delay: piezoelectric delay stage.

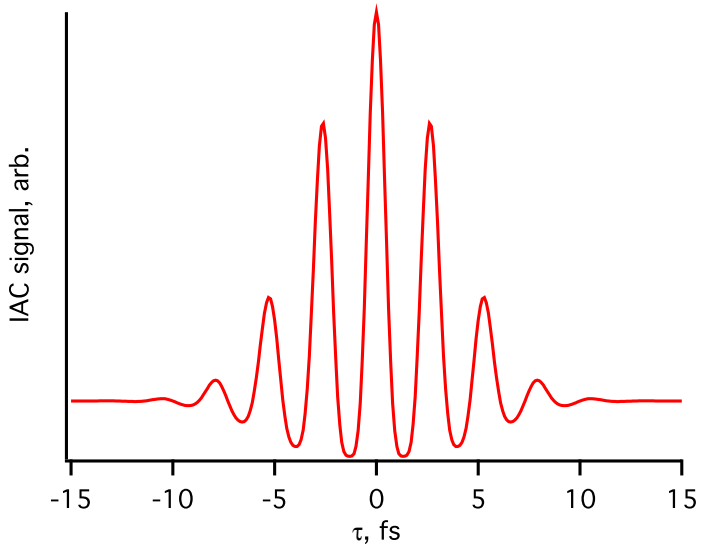

Figure 4.2: **Calculated IAC of a 5 fs, 800 nm pulse.**

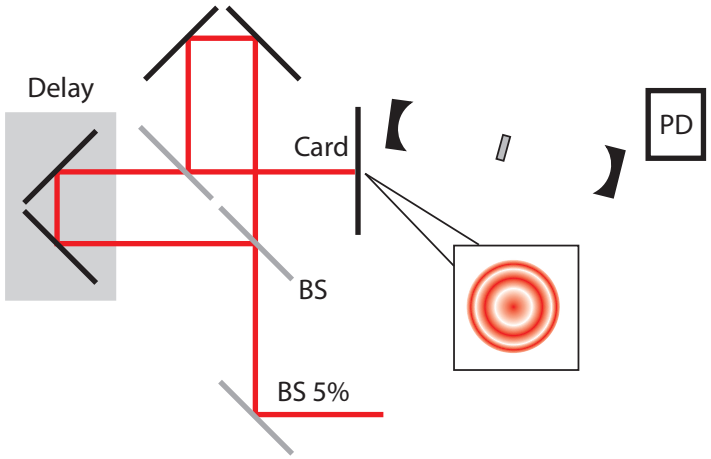

Figure 4.3: **Autocorrelator.** BS: beamsplitter. BBO: nonlinear crystal. PD: photodetector. Delay: piezoelectric delay stage.

4.3 Autocorrelator instructions

The alignment of the autocorrelator from scratch is simple.

Initial alignment. Split 5% off of the beam to be measured (more and the nonlinear crystal in the autocorrelator could burn) and direct it into the autocorrelator at normal incidence. Now switch to a HeNe beam that is perfectly following the beam you wish to measure.

Spatial overlap Open the top of the autocorrelator and observe the interferometer output using a card before the parabolic mirror. Using an allen key align the interferometer turning mirror so that the two beams overlap on the card. You should see spatial fringes. If you don't, take the parabolic mirror out and observe the HeNe beams farther from the interferometer. Make them overlap at a point several feet away then replace the parabolic mirror and check again for fringes there. Fine-tune the alignment so that the fringe pattern is round and centered in the middle of the beam. If the fringes look like they are oriented vertically, change the horizontal pointing of the mirror slightly, and if they look like they are oriented horizontally, change the vertical position of the mirror. You should be able to observe large areas of extinction due to destructive interference, as in fig. 4.3. Ideally the whole beam would be extinguished at once, but this does not occur in our autocorrelator because of wave-front errors in the optics comprising the interferometer.

Temporal overlap Now that the beams are aligned spatially, you must find temporal overlap. To accomplish this, let the short pulse into the autocorrelator and observe the spectrum after the interferometer using a fiber-optic spectrometer probe (fig. 4.4). If there are fringes in the spectrum, adjust the time delay to maximize the fringe period.

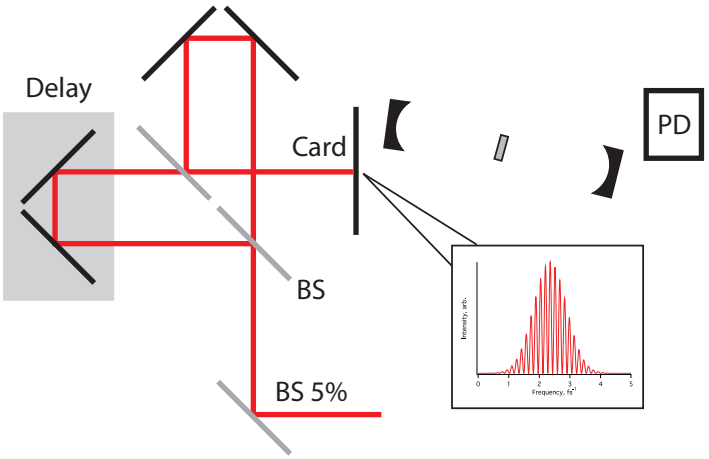

Figure 4.4: **Autocorrelator.** BS: beamsplitter. BBO: nonlinear crystal. PD: photodetector. Delay: piezoelectric delay stage.

If there are no fringes, search by tuning the delay slowly until you see them. Now that spatial and temporal overlap are achieved, turn on the piezo controller and start the acquisition software. You will have a nice IAC trace waiting for you. The trace can be optimized by slightly changing the alignment of the autocorrelator while watching the trace output on the computer.

4.4 SPIDER principle of operation

Like FROG and interferometric autocorrelation, SPIDER is a self-referencing method for laser pulse characterization. In SPIDER, two copies of the pulse to be measured are upshifted in frequency by slightly different amounts, and allowed to interfere in a spectrometer. The interference fringe pattern reflects the spectral phase of the laser pulse. In practice, the frequency shift is provided by sum frequency generation using a third copy of the same pulse. The optical layout of the SPIDER is represented in figure 4.5.

Two copies of the short pulse are obtained by reflection of the pulse off the surface of an SF10 glass block. The reflection travels through a Mach-Zehnder interferometer, where it is split into two copies with variable delay. The main portion of the pulse, referred to as the shearing beam, travels through the glass block which chirps it substantially. To a first approximation, it is a CW beam over the timescale of the short pulse. The three pulses overlap in a BBO crystal and the sum frequency light is directed into a spectrometer.

In the case of no shearing beam, the interferogram between the two pulses reveals the delay of the Mach-Zehnder interferometer only. This delay imprints a linear spectral phase $\phi(\omega) = \omega\tau$, and so the delay can be measured. When the pulses are upconverted by the shearing beam, the slight time delay τ implies that they are upshifted in frequency by slightly different amounts, according to τ and the dispersion of the SF10 block. Now at

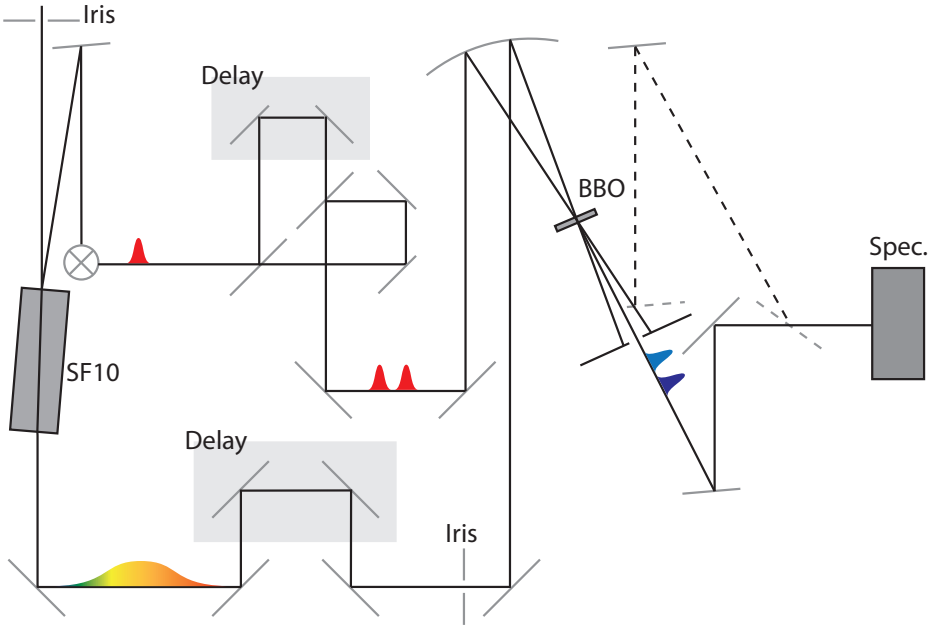

Figure 4.5: Optical layout of the SPIDER.

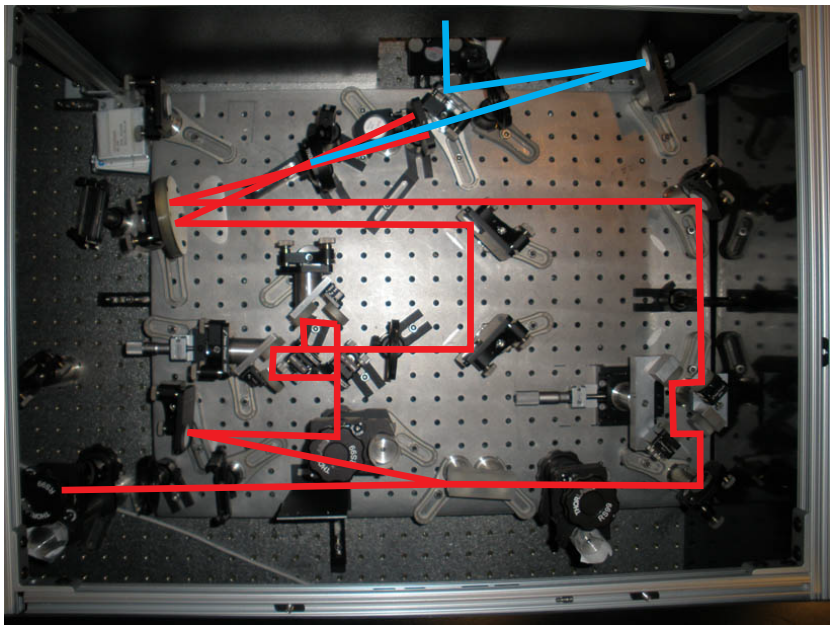

Figure 4.6: Optical layout of the SPIDER.

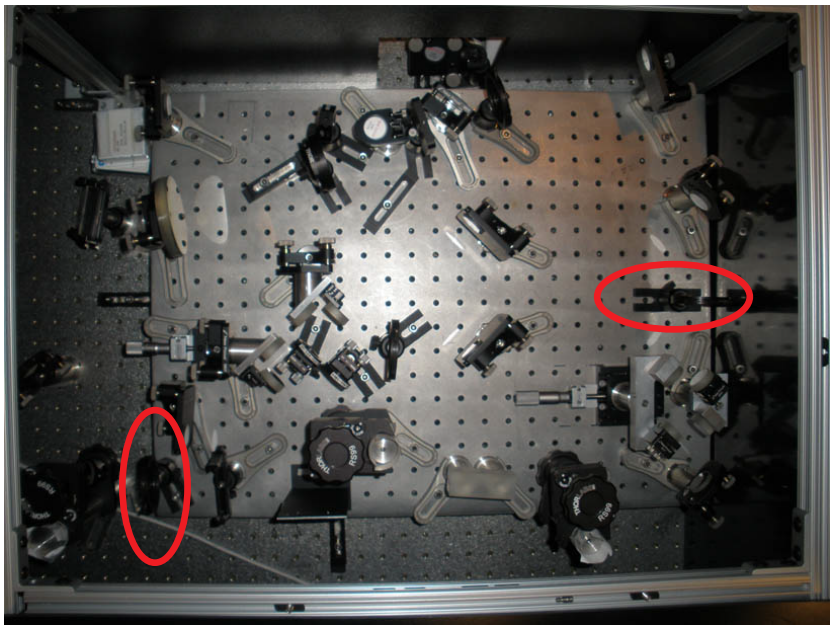

Figure 4.7: Align the beam to these two irises.

any particular wavelength in the spectrometer, there is a phase difference between the two short pulses equal to $\omega\tau$ *plus the phase difference between the the two neighboring frequency components of the short pulse.* This is the key to SPIDER: it allows to measure directly the spectral phase *difference* at two neighboring frequencies, or equivalently, the *derivative* of the spectral phase.

For more information on the mathematics of SPIDER, see Lukas Gallmann's thesis, which should be floating around, or Iaconis and Walmsley, *Opt. Lett.* **23** 792. [87]

4.5 Instructions

To use the SPIDER, follow these instructions.

Initial alignment. First, the incoming beam must be perfectly centered on the iris at the entrance and the iris after the glass and delay in the shearing arm (figure 4.7). If it is not, walk it so that it is. Satisfying this condition will automatically send the output of the Mach-Zehnder interferometer through the interferometer iris.

Interferometer alignment. The alignment of the Mach-Zehnder interferometer is critical, and depends sensitively on the direction of the input beam. Once the input beam is through the irises, observe the output of the Mach-Zehnder interferometer in the spectrometer at 800 nm. This requires turning up the two flipper mirrors (dashed lines in fig. 4.5, or figure 4.8). The fringe contrast should be at least 25%. If it is not, adjust the pointing of the beam splitter *nearest the focusing mirror* to optimize

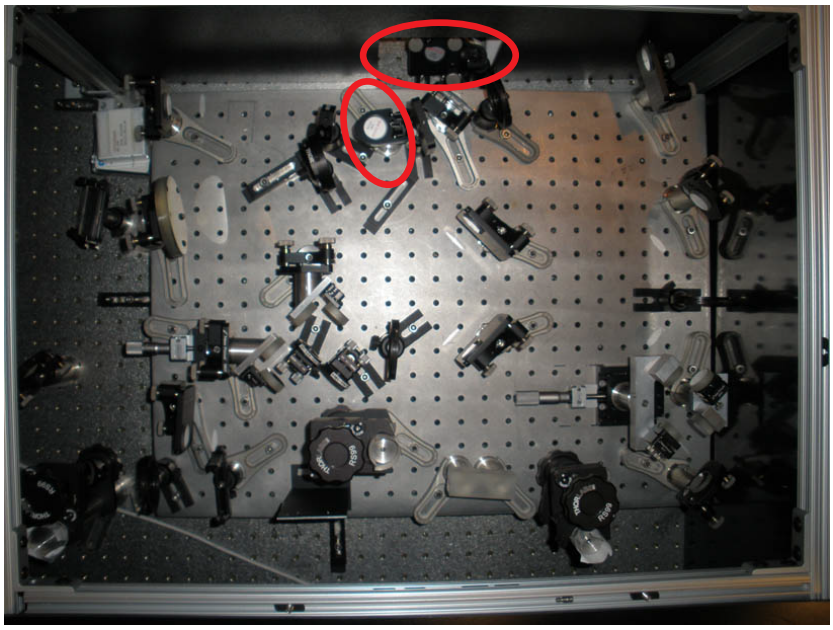

Figure 4.8: To observe the output of the interferometer with no shearing interaction, flip up these two mirrors.

the fringe contrast. *Never* move the other beamsplitter or the turning mirrors in the interferometer.

Measuring the fundamental spectrum. Now, the fundamental spectrum needs to be measured. Block the input and hit "acquire background" in the SPIDER program. Open the input, but block one arm of the interferometer. Hit "Measure fundamental spectrum." This will store the fundamental spectrum in the memory of the SPIDER program. A calculated example fundamental spectrum is shown in figure 4.10.

Move the grating. Block the input of the SPIDER. Using the monochromator control software, switch to the 600 l/mm grating. This will move the spectrometer to zero order, so if the input is not blocked, you can easily damage the camera. Move the grating position to 390 nm and acquire a new background.

Measure the spectral shear. This number is critical to obtain accurate results. There is a type I BBO in the SPIDER at the moment, so there should be some blue light generated that travels collinearly with the short pulses from the interferometer. This blue light, a calculated example of which is shown in figure 4.11, is used to measure the shear. Direct it into the spectrometer and observe the FFT of the spectrometer signal. It should have a cleanly separated peak at positive frequency. If it does not, *slightly* adjust the delay of the interferometer. Note the peak position: it might be around 600. Subtract 512 from that number and enter that in the field "center" on the delay calibration portion of the program. Hit "take delay calibration" to acquire the spectrum. The FFT of the spectrum should have a peak centered under the red

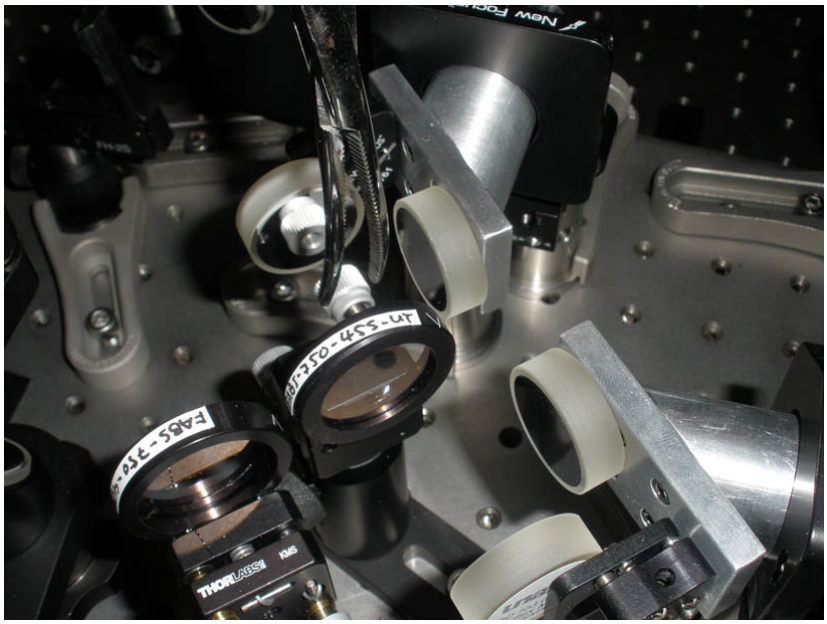

Figure 4.9: Adjust the beamsplitter with a hemostat.

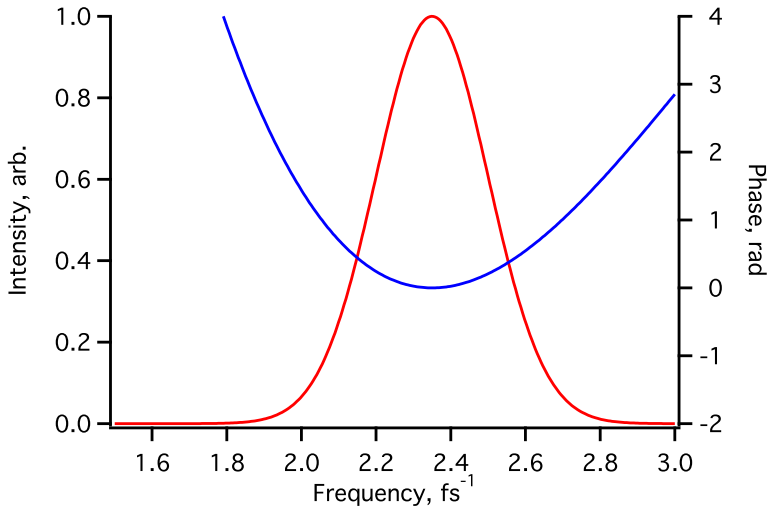

Figure 4.10: **Fundamental spectrum and phase.** The red fundamental spectrum can easily be measured using the spectrometer, but the blue spectral phase must be determined by SPIDER.

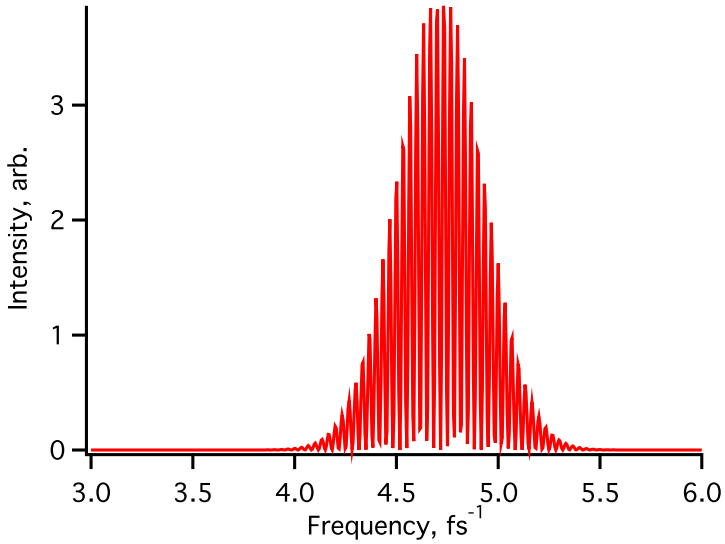

Figure 4.11: **Interferogram of two second-harmonic pulses.** This interferogram, generated by doubling the two pulses output from the Mach-Zehnder interferometer, reveals the delay between the two pulses. The delay is calculated from the interferogram using the fact that the phase difference between the two beams is simply $\omega\tau$, where ω is the frequency and τ is the time delay. The time delay also gives the spectral shear, which is equal to τ divided by the dispersion of the glass block: 10,341 fs^2.

supergaussian windowing function in the delay calibration FFT window. The SPIDER program automatically calculates the shear and updates the "shear" field. Note that if the shear field is 0 or NaN, the program will not run. Stop it, update the field manually to some small number like 0.001, and restart the program. Unfortunately, you will also have to start over in this list.

Note: To avoid communication errors with the camera, always use the square "STOP" button, not the stopsign-shaped abort button provided by LabVIEW.

Generate SPIDER signal. Now, the overlap between the shearing beam and the short pulses should be pretty good in the BBO. Look for the blue light generated by SFG that goes through the iris after the BBO. This blue light should be directed into the spectrometer (calculated example: figure 4.12). The yield can be optimized by adjusting the turning mirror that puts the shearing beam onto the focusing mirror. The FFT of the SPIDER trace (a calculated example of which is shown in figure 4.13) should have a peak in the same place as when you measured the spectral shear. The program filters out this peak and back-transforms it, leaving you with the phase. The phase has a strong linear component, shown for the calculated example in figure 4.14. Once the linear component is removed by the program, the phase and spectrum are shown in the upper left display, and the time-dependent pulse envelope is in the upper right display. Hit "save" to save your data.

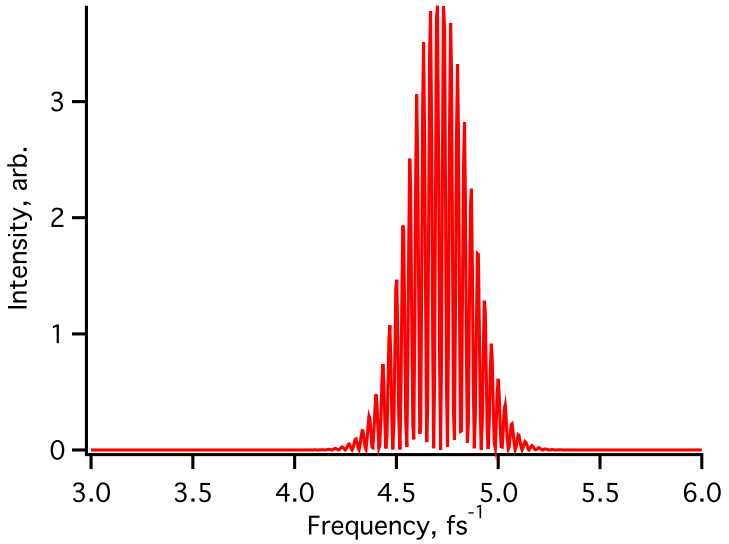

Figure 4.12: **Example SPIDER trace.** Even though it looks remarkably similar to the interference of the two arms of the interferometer, this calculated interferogram contains the spectral phase variation of the pulse to be measured.

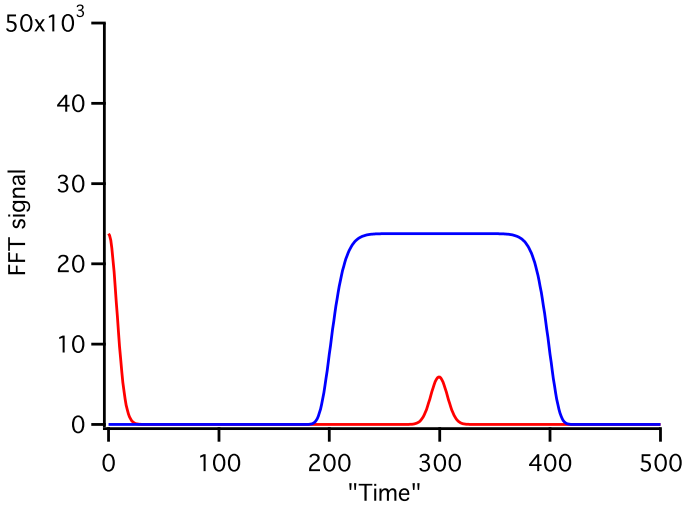

Figure 4.13: **Example FFT of a SPIDER trace.** The FFT of the spider trace (red) shows one peak cleanly separated from the DC component. This peak contains the phase information we are interested in, so it is filtered out by multiplying by a supergaussian function (blue) ten back-transformed.

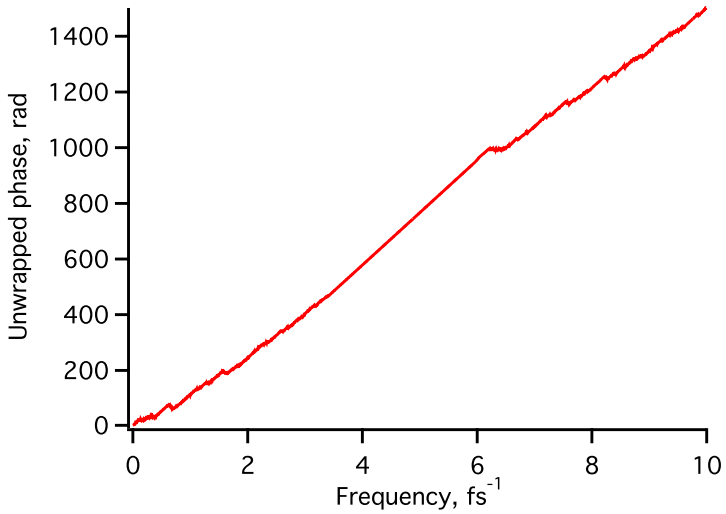

Figure 4.14: **Example phase retrieved from SPIDER trace.** The phase of the back-transformed signal is shown here. The strong linear component is due to the time delay between the two pulses coming from the Mach-Zehnder interferometer. When the linear component is removed and the signal is integrated, the result is the spectral phase. This is implemented in the SPIDER program so you do not have to do it by hand.

More notes. You may need to adjust the horizontal pointing of the turning mirrors that direct the beams into the spectrometer to get good signal.

Do not adjust the delay of the shearing beam. This changes the upconversion frequency, so the "2.27" listed in the program will not be accurate anymore. While the upconversion frequency is important, small variations will not cause large errors in the retrieved phase. This is not the case for the shear, however, where precision on the level of 4 digits or more is required.

To measure the shearing frequency, compare the fundamental spectrum to the upconverted spectrum of one arm of the Mach-Zehnder interferometer.

There is now a type I BBO in the setup, but the shearing beam is orthogonally polarized to the short pulses. Therefore, the BBO is rotated 45 degrees. The thickness of the BBO is only 0.1 mm so that phase matching can be achieved across the entire spectral bandwidth.

How to tell if your results are OK. Always check that your results make sense. You should be able to put a piece of glass in the input beam and observe the quadratic change in the spectral phase. If you are getting nonsensical results, there are a few things to check. First, make sure that the program knows the monochromator settings (600 l/mm, 390 nm). Next, check that the fringe spacing is small compared to the fastest variations in the fundamental spectrum. You can do this by measuring the FFT of the fundamental spectrum spectrum using only one arm of the interferometer. You should see a place in the FFT at large frequencies where the baseline is zero. Adjust

the interferometer delay to put the FFT peak from the fringes there and recalculate the shear. Next, check that there is no contamination of the FFT peak that the supergaussian windowing function is filtering out. Play with the center and width of the supergaussian to do that.

Chapter 5

Carrier-Envelope Phase Dependent Multiphoton Ionization of Xe

The contents of this chapter have been published in J. Phys. B: At. Mol. Opt. Phys., **42**, 075601 (2009)*, reference [111].*

5.1 Introduction

The carrier-envelope phase of few-cycle laser pulses is a very important quantity for atomic and molecular physics because of the attosecond electric-field response of electrons. it is one of the key quantities of attosecond pulse production, in fact, as it can determine the number [112] or wavelength [102] of attosecond light pulses produced in high harmonic generation. It also influences the angular distributions of photoelectrons in strong-field tunneling ionization [113], the localization of electrons in molecular dissociation [114], and the direction of photocurrent in semiconductors [115]. In this chapter, experimental data is presented showing how the CEP affects the angular distribution of photoelectrons generated at electric field strengths in the multiphoton regime.

Even though the CEP appears in the single-photon dipole transition amplitude in perturbation theory, it does not necessarily affect the transition probability, which is the squared modulus of the amplitude. As a result, CEP effects are not extensively explored. Equally importantly from an experimental point of view, the frequency comb techniques required to stabilize the CEP [92, 116] were not available until recently. The combination of few-cycle ultrabroadband laser pulses [117], extension of the laser frequency comb all the way to zero frequency [92, 118], and a growing realization that many process are determined by the laser field and not just the intensity envelope of light pulses have stimulated growing interest in the role of the CEP.

Because of the importance of CEP stabilization in the creation of isolated attosecond x-ray pulses by few-cycle driver pulses [112], much effort to date has focused on the role of the CEP in strong-field processes driven by fields comparable to the Coulomb field that binds valence electrons to atoms and molecules. In this regime, electrons react nearly adiabatically [119, 120] to the oscillating laser field, and processes like tunneling [119] and photoemission [121] occur on a sub-cycle (attosecond) timescale. Some work has addressed non-adiabatic

dynamics in tunneling ionization [3, 122], but relatively little research has been directed towards discovering the role of the CEP in the weak-field, perturbative regime, where the laser field is small compared to intra-atomic field strengths. A few experiments have confirmed a role for the CEP in perturbative laser-atom interactions [115, 123, 124] but these works have emphasized CEP stabilization.

Nakajima and Watanabe recently obtained intriguing theoretical results [125] showing a CEP effect in the perturbative regime. They solved the time-dependent Schrödinger equation (TDSE) for cesium atoms exposed to very short perturbative laser fields and found that excited state populations after the laser pulse depend on the CEP; in some cases the populations vary by a factor of 2 or more. Comparing the atom to a 3-level system, they formally solved the perturbation-theoretical differential equations governing the time-dependent state amplitudes. The amplitude for the uppermost state is the sum of four terms, one of which dominates the population in the case of long driving laser pulses. The authors suggested that the CEP effect present in the TDSE results may be due to the other three terms in the overall amplitude, which contribute for very short driving laser pulses.

Recent theoretical work on CEP effects [126] emphasized the role of interferences between distinct multiphoton pathways as the key to understanding CEP effects in both the strong- and weak-field regimes. The multiphoton picture is particularly relevant to the experimental intensity regime here, and we follow the example in reference [126], interpreting the experimental results in terms of a multiphoton interference picture in which the absolute spectral phase of the laser pulse–CEP and chirp–plays a key role.

Above threshold ionization (ATI) using short laser pulses in the non-perturbative, strong-field regime has been systematically explored by Kling *et al.* [127]. This paper focused on high-energy photoelectrons (kinetic energy $\gtrsim$10 eV) and did not discuss in detail the asymmetry in the distributions of low-energy photoelectrons. We experimentally visit a lower regime of laser field strength, using 750 nm, 7 fs CEP-stabilized pulses at an intensity of $\sim$3x10^{13} W/cm^2 to photoionize xenon atoms while collecting the full 3-dimensional photoelectron momentum distribution, concentrating our analysis on photoelectrons with energies below $\sim$5 eV. When the CE phase ϕ is varied, the angular distribution of photoelectrons changes so that the relative number of photoelectrons going in one direction along the laser polarization versus those going in the opposite direction varies sinusoidally from perfect symmetry. This up-down asymmetry is a function of both the CEP and photoelectron energy and also depends on the chirp of the laser pulse. The asymmetry distribution is interpreted using a simple model that invokes interferences between different quantum pathways leading to the same final photoelectron kinetic energy, resulting from absorption of either N or N+1 photons from opposite ends of the broadband laser spectrum by the atom.

5.2 Experimental Setup

The experimental setup was described in detail in chapter 3, but the relevant portions will be described briefly again here. The experiment makes use of a 0.8 mJ, 25 fs, multipass Ti:sapphire amplifier system operating at 3 kHz (Figure 5.1). The output, initially centered at 800 nm wavelength, is spectrally broadened and slightly blue-shifted in a hollow-core fiber filled with about 2 bar of neon gas before temporal compression using chirped mirrors. The

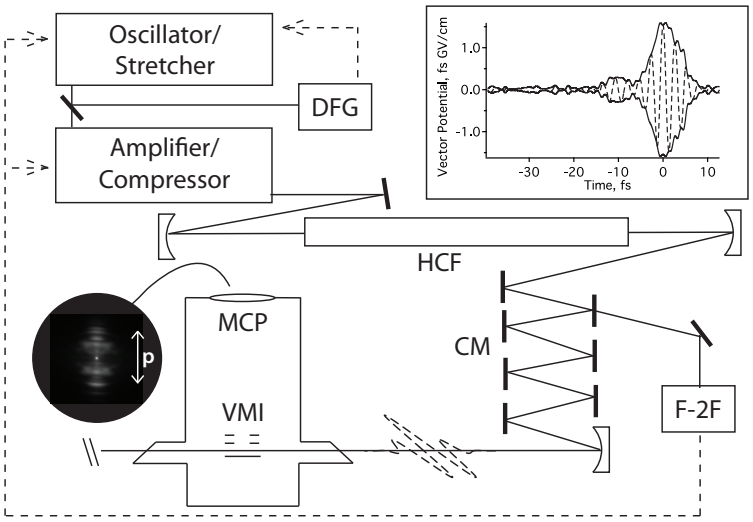

Figure 5.1: **Experimental setup.** Shown looking down onto the laser table, the polarization direction is out of the plane of the paper. DFG, difference frequency generation and feedback loop for oscillator CEP locking. HCF, hollow-core fiber. CM, chirped mirror compressor. F-2F, f-2f interferometer and feedback loop for amplifier CEP locking. VMI, electrostatic lenses for velocity-map imaging. MCP, multichannel plate electron detector with detector face parallel to the laser polarization direction, p. **Inset.** Pulse envelope measured by attosecond streaking in neon (solid line), and an example vector potential to illustrate the relative durations of the carrier wave period and the envelope (dashed line).

resulting pulse is ∼7 fs in duration with 750 nm central wavelength. The compression is adjusted using a pair of fused silica wedges to produce the highest ionization rate in the target gas sample. The strongest ionization, corresponding to the highest peak intensity, is not necessarily coincident with flat spectral phase at the central frequency in the case of current few-cycle pulse generation technology. Therefore, some residual chirp is expected to remain in the pulse at the interaction region. In a separate experiment the temporal profile of the vector potential was measured using attosecond streaking [128] in neon. At the time of these measurements, the individual cycles of the laser pulse were not resolved. The measured pulse envelope is shown in the inset in figure 5.1. The streaking data reveal the envelope of the vector potential and indicate that the pulse compression scheme works well, leaving only a small prepulse. The full results of a cycle-resolved streaking experiment described in chapter 6 agree with the envelope measurement presented here. The oscillator carrier-envelope offset frequency is detected using difference frequency generation and stabilized using a feedback loop that controls the pump laser power. Long-term drifts in the CEP of the amplifier are corrected using f-2f interferometry [92] after the hollow-core fiber and a feedback loop that varies both the oscillator pump laser power and the prism insertion in the laser compressor. The CEP jitter of the overall system is measured over a ∼5 s sliding time window by the f-2f interferometer at a spectrometer acquisition rate of ∼30 Hz, with 30 ms exposure time. It ranges from 100 mrad to 300 mrad RMS depending on the day-to-day performance of the amplifier and the spectral broadening.

The photoelectrons generated by multiphoton above-threshold ionization are acceler-

ated toward a 2-dimensional position-sensitive detector using velocity map imaging (VMI) [129, 130]. In VMI, all the photoelectrons leaving the interaction region with the same initial velocity vector will be focused to the same spot on the detector, regardless of their initial position. Because of this convenient property of VMI and the cylindrical symmetry of photoemission about the laser polarization axis, the output of the position sensitive detector can be easily inverted to yield the laboratory frame momentum distribution by mathematically taking into account the multiple velocity vectors that can all lead tot he same spot on the detector. This is the essence of the basis set expansion (BASEX) [131] method used here.

5.3 Results

Since we are interested in CEP effects in the multiphoton regime, we reduce the beam diameter and therefore the peak intensity using an adjustable iris aperture to achieve a photoelectron kinetic energy spectrum with only a few peaks and with the first peak the most intense. For above threshold ionization (ATI) with strong laser pulses, the photoelectron kinetic energy corresponding to the maximum intensity in the photoelectron spectrum is roughly equal to the ponderomotive energy U_p [132] of the laser field, and a cutoff exists at $2U_p$ beyond which direct photoemission no longer contributes to the spectrum. Also, the direct photoemission peaks are offset by an amount equal to U_p. The shape of the photoelectron spectrum (Figure 5.2 (a)) implies that, in this case, the ponderomotive energy is equal to or less than 1.6 eV, the energy of a single laser photon. Since U_p in eV is equal to $9.33\lambda^2(I/10^{14})$ with λ in microns and I in W/cm^2, an upper limit to the intensity is about 3x10^{13} W/cm^2. In fact, a ponderomotive shift of 1.6 eV and the ionization potential of Xe (which is 12.1 eV) reproduce the position of the first ATI peak. Since the peak position estimate and the estimate of U_p from the maximum photoelectron intensity agree, they together serve as an estimate for the laser intensity in the interaction region.

Defining the asymmetry $A(\epsilon)$ as the difference in signal between the top and bottom half of the momentum distribution at a particular photoelectron energy ϵ,

$$A(\epsilon) = \frac{n_{up}(\epsilon) - n_{down}(\epsilon)}{n_{up}(\epsilon) + n_{down}(\epsilon)}, \tag{5.1}$$

the result shown in Figure 5.2 panel (b) is obtained. The uppermost asymmetry trace corresponds to an arbitrary and unknown CEP. The CEP is changed by $\pi/10$ for each new measurement, over a total range of 2π. Note that there are certain special photoelectron energies for which the asymmetry is zero regardless of CEP. These energies are spaced by one laser photon energy and correspond to the tops of the peaks in the photoelectron spectrum. They are marked with arrows in Figure 5.2 (b). Notice also that the pattern between the first and second peaks repeats itself between the second and third peaks, and so on.

Checks are made to ensure that the observed asymmetry is a real effect of the CEP. First, a CEP offset of 2π is equivalent to an offset of 0 so ideally these two asymmetry traces would be perfectly correlated with each other. As shown in panel (a) of Figure 5.3, the correlation between each pair of 0 and 2π points is pronounced when the kinetic energy ϵ <4.6 eV. The scatter of the data reflects the CEP jitter, which in this experiment was less than 150 mrad,

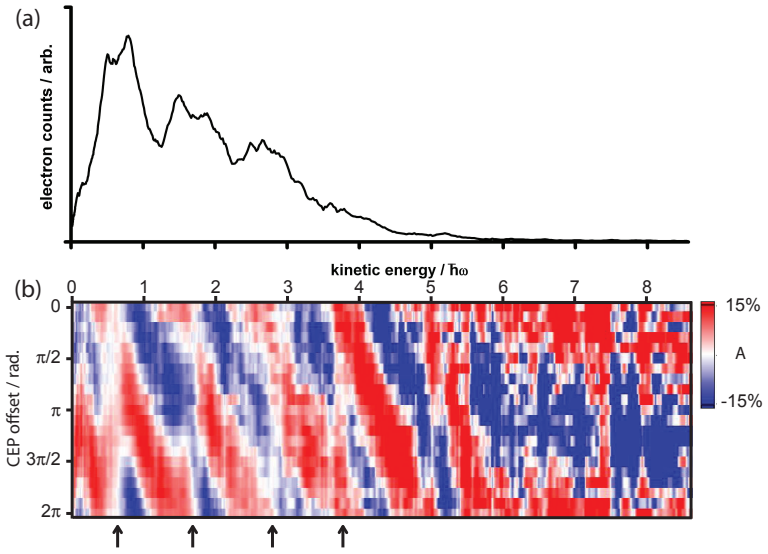

Figure 5.2: **(a)** A typical photoelectron momentum spectrum. **(b)**: The up/down asymmetry in the photoelectron spectrum as a function of CEP offset ϕ and electron kinetic energy. Blue fill corresponds to more electrons going upwards in the lab frame (parallel to the laser polarization vector) while red fill corresponds to more electrons going downwards (anti-parallel to the laser polarization vector). The arrows point to kinetic energies where the asymmetry is close to zero independent of CEP. These regions fall at the same kinetic energies as the tops of the peaks in the photoelectron spectrum.

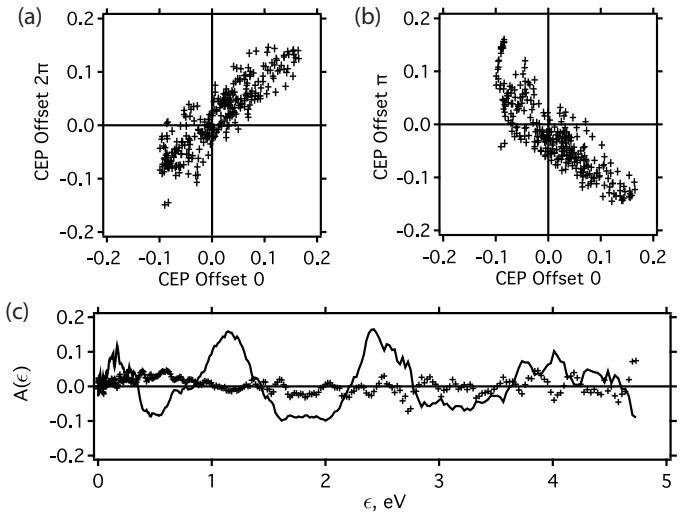

Figure 5.3: **(a)** $A(\epsilon)$ for CEP offset set to 2π plotted vs. $A(\epsilon)$ for CEP offset set to 0. **(b)**: $A(\epsilon)$ for CEP offset set to π plotted vs. $A(\epsilon)$ for CEP offset set to 0. **(c)**: $A(\epsilon)$ for CEP offset 0 (line) and averaged over all CEP values (crosses). The CEP-averaged data would be equivalent to the case of short pulses with no CEP stabilization—the asymmetry is nearly zero for all photoelectron energies.

plus the noise accumulated in the data collection and processing. Similarly, because changing the CEP by π corresponds to flipping the laser electric field vertically in the lab frame, one would expect that the asymmetry traces corresponding to any two CEP offsets separated by π radians should be perfectly anticorrelated. This is the case, as illustrated for CEP offset 0 and CEP offset π in panel (b) of Figure 5.3. Finally, when all the asymmetry traces are averaged, corresponding to the case of no CEP stabilization, the resulting asymmetry trace is flat as shown in panel (c) of Figure 5.3.

At intermediate intensities of a few 10^{13} W/cm^2, the instantaneous ionization rate is a combination of field-dependent (tunneling) and intensity-envelope-dependent (multiphoton) ionization, the relative contributions of which can be estimated analytically using the theory of Yudin and Ivanov [122]. The theory is constructed in such a way as to agree with the well-accepted Ammosov-Delone-Krainov (ADK) result in the case of strong fields and to agree with the multiphoton result in the limit of weak fields. Calculating the ionization rate as a function of time for the laser pulse parameters (7 fs duration, I = 3x10^{13} W/cm^2) and averaging over the intensity variation in the interaction region indicates that the multiphoton contribution is about half the signal. This is in contrast to the intensity of the short pulses used by Kling *et al.* [127] to study CEP effects in the Xe atom, where the multiphoton contribution to the ionization was only about 10%.

5.4 Multiphoton Model

Although the experiment was performed in a regime between pure multiphoton and pure tunneling ionization, the observed experimental results can be interpreted qualitatively in

terms of a multiphoton model based on interference between indistinguishable quantum paths. Amending the model to incorporate tunneling effects may increase the quantitative agreement, but the essential physics is described by the multiphoton model.

Since the laser pulse has a very large bandwidth, there are multiple combinations of photons, all of different colors, that when ionizing a xenon atom in its ground state would lead to the same continuum kinetic energy for the photoelectron. Each combination of photons carries a characteristic phase, the sum of the spectral phases of the individual frequencies involved. The relative weights of the different pathways are influenced by the details of the energy level scheme of the particular target atom–for example, pathways with intermediate resonances or near-resonances will be more favorable than non-resonant pathways. All these different pathways add coherently to give the final probability for finding the outgoing electron at a particular outgoing energy and angle. But different combinations of wavelengths do not on their own generate asymmetry along the laser polarization direction in the photoelectron distribution. It requires interference between wavefunctions having different parity, or equivalently, mixing between quantum pathways involving different numbers of photons. Ionization of an odd-parity p-electron in Xe by 8 photons from the blue end of the spectrum will lead to an odd-parity continuum state, while ionization by 9 photons from the red end of the spectrum leads to an even-parity state of the same energy. This is similar to the principle of the f-2f interferometer [92], where the blue region of the laser spectrum interferes with the second harmonic of the red region.

Ignoring interactions with the ion core, the CEP-dependent wavefunction $\Psi(\phi)$ of the outgoing electron can be written as a sum of angular momentum eigenfunctions $Y_{l,m} = P_{l,m}(\theta)e^{im\varphi}/\sqrt{2\pi}$ weighted with complex amplitudes $c_{l,m}(\epsilon,\phi)$. Instead of three spatial coordinates, it is convenient to choose the electron energy ϵ and the two angles θ and φ (written together as Ω) as coordinates for Ψ. At any particular value of ϵ quantum pathways with one of two photon numbers are contributing to the photoelectron emission. Grouping the even parity functions with angular momentum quantum numbers (l,m) separately from the odd parity functions with angular momentum quantum numbers (l',m'),

$$\Psi(\epsilon,\Omega,\phi) = \sum_{l\,even,m} c_{l,m}(\epsilon,\phi)Y_{l,m}(\Omega) + \sum_{l'\,odd,m'} c_{l',m'}(\epsilon,\phi)Y_{l',m'}(\Omega) \tag{5.2}$$

The asymmetry as a function of photoelectron energy ϵ and CEP ϕ can be expressed in terms of Ψ; it is the difference between the probability of finding an electron going up and the probability of finding one going down in the lab frame, divided by the total probability of finding a photoelectron at that energy:

$$A(\epsilon,\phi) = \frac{\int_{up}|\Psi(\epsilon,\Omega,\phi)|^2 d\Omega - \int_{down}|\Psi(\epsilon,\Omega,\phi)|^2 d\Omega}{\int_{up}|\Psi(\epsilon,\Omega,\phi)|^2 d\Omega + \int_{down}|\Psi(\epsilon,\Omega,\phi)|^2 d\Omega} \tag{5.3}$$

Normalization of Ψ means that the denominator in Equation 5.3 is equal to unity. Inserting Ψ from Equation 5.2 and expanding the sums, the cross terms in each integral cancel unless the functions have non-zero overlap ($m = m'$). Since $m = m'$, the azimuthal contribution to the integrals is simply 2π and the polar integral over pairs of (real-valued) Legendre

functions $P_{l,m}$ is all that remains:

$$\begin{aligned} A(\epsilon,\phi) &= 2\sum_{l,l',m}\{c_{l,m}(\epsilon,\phi)c^{*}_{l',m}(\epsilon,\phi)+conj.\} \\ &\quad\times\int_0^{\pi/2} d\theta sin(\theta)P_{l,m}(\theta)P_{l',m}(\theta) \end{aligned} \tag{5.4}$$

Each of the amplitude terms contains $e^{i\phi}+e^{-i\phi}$ and so the asymmetry is cosinusoidal with CEP. We note that the amplitudes c may contain phase contributions other than the CEP; for example, they depend on the laser pulse chirp and on the atomic phase intrinsic to photoionization. These phase contributions may vary with energy, but they do not change the CEP-dependence of the asymmetry at fixed energy.

To simplify Equation 5.4, assume the example of an outgoing wavefunction at a particular energy ϵ_o between the N^{th} and $(N+1)^{st}$ ATI peaks that is composed of an s-wave (N photons absorbed) and a p-wave (N+1 photons absorbed) with equal weights. The p-wave corresponds to absorption of one extra photon compared to the s-wave, giving it an extra phse contribution equal to the CEP. For this example, also assume that the laser pulse has a perfectly flat spectral phase so there is no chirp, and there are no intrinsic atomic contributions to the phase difference between the two partial waves. Then the only phase difference between the two waves is caused by the extra contribution of the carrier-envelope phase, ϕ, caused by the different number of photons required to reach the even- and odd-parity states. In this case, the wavefunction consists of a sum of two spherical harmonics, separated in phase by the CEP, and each normalized by multiplying by $1/\sqrt{2}$. The wavefunction and asymmetry are:

$$\Psi(\epsilon_o,\Omega) = \frac{1}{\sqrt{2}}\left(\frac{1}{\sqrt{4\pi}}\right)+\frac{e^{i\phi}}{\sqrt{2}}\left(\frac{\sqrt{3}cos(\theta)}{\sqrt{4\pi}}\right) \tag{5.5}$$

$$A(\epsilon_o,\phi) = \left(\frac{e^{-i\phi}}{2}+\frac{e^{i\phi}}{2}\right)\int_0^{\pi/2} d\theta\sqrt{3}sin(\theta)cos(\theta) \tag{5.6}$$

$$= \frac{\sqrt{3}}{2}cos(\phi) \tag{5.7}$$

The asymmetry in Equation 5.7 varies cosinusoidally with the CEP, which directly matches the experimental observation for CEP variation at fixed energy. Figure 5.4 shows a cut through the experimental asymmetry plot at a photoelectron kinetic energy of 1.6 eV. The asymmetry does indeed vary as a phase-shifted cosinusoidal function of the CEP offset. This simplified analysis does not take experimental details like spatial averaging of the laser intensity in to account. Spatial averaging of the laser intensity in the interaction region does not change the CEP-dependence of the asymmetry, but can affect the yields of photoelectrons into different multiphoton pathways. Thus the spatial averaging does not affect the main conclusions of this paper, namely that the CEP effects in multiphoton ionization are a result of quantum interferences between different multiphoton pathways.

The current model can be understood as a special case of the work of Roudnev and

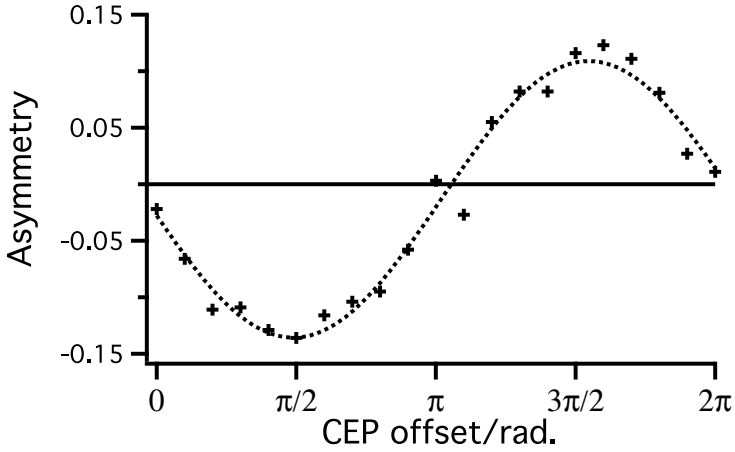

Figure 5.4: The CEP response of the asymmetry at constant ϵ is sinusoidal in agreement with Equation 5.4. A cut through the experimental data at ϵ=1.6 eV is marked by the crosses, and the dotted line is a sinusoidal fit to the data.

Esry [126]. It is intended to straightforwardly illuminate the principle of CEP effects by interference between quantum pathways, with special application to the case of multiphoton ionization of atoms. While it lacks the generality of their work, it describes the experimental data in an illustrative way.

There are other possible contributions to the phases of the partial waves that enter into the angular distribution: specifically, the spectral phase of the laser pulse and an intrinsic atomic phase arising from the (in general multi-electron) interaction between the ion core and the photoelectron after ionization. If the laser pulse is chirped the outgoing photoelectrons will be chirped as well, reflecting the laser pulse that ionizes the atom. However, the chirp of the photoelectron wavepacket for a particular photon number N will not be identical to that of the laser pulse because there are many combinations of N photons, each of different wavelengths, that lead to the same photoelectron energy. The phase contribution due to the chirp, then, is a weighted average of all the possible N-photon pathways, each pathway having its own spectral phase contribution. This is shown schematically in Figure 5.5 (a), where the quadratic spectral phase of a linearly chirped laser pulse is mapped onto each outgoing photoelectron wavepacket of alternating parity. The spectral phase curve for each successive photoelectron peak is offset vertically by the CEP, so that there are some photoelectron energies where the curves intersect and total constructive interference occurs.

When the CEP increases, as shown by the dotted phase curve, the intersections of the spectral phase curves change in energy and the positions of maximal constructive interference in the photoelectron spectrum move toward higher energy. In order to calculate the effect of the CEP and laser spectral phase, the "weighted average" of multiphoton pathways can be approximated by an autoconvolution of the laser pulse. That is, neglecting the atomic phase and any resonances, the complex spectrum (amplitude and phase) of the N-photon absorption peak is the complex laser spectrum convoluted with itself N times. Numerical

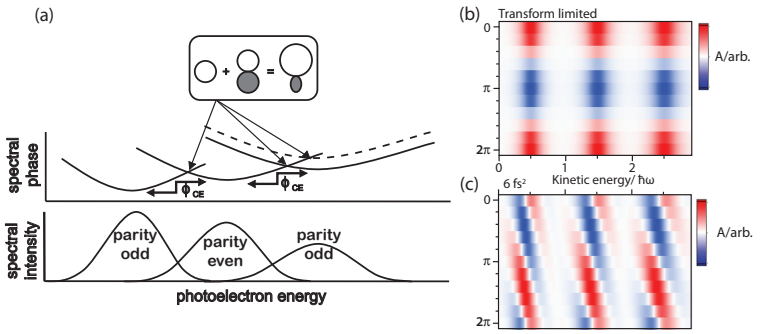

Figure 5.5: Schematic and simulation of the multiphoton mechanism for CEP effects. **(a)** The spectral phase of outgoing photoelectron wavepackets of different parity depends on the laser pulse spectral phase. The curves are offset by the CEP, because of the absorption of an additional photon in each case. When the phase difference (mod 2π) vanishes, constructive interference occurs. Tuning the CEP changes the relative offset of the curves, as in the case of the dashed phase curve, and the energies where maximum asymmetry occurs change correspondingly. In this sketch, the photoelectron peaks are drawn wider with increasing energy reflecting the larger spectral width available for excitation with higher numbers of photons. **(b)** Simulation of the asymmetry as a function of CEP and energy is accomplished by calculating higher order autoconvolutions of the experimental spectrum, assuming flat spectral phase. The asymmetry is then calculated from the amplitudes assuming interference between s waves (even parity states) and p waves (odd parity states). In this case the regions of maximal asymmetry vs. CEP are stationary in energy. **(c)** Adding 6 fs^2 of chirp to the pulse tilts the regions of maximal asymmetry so that they move to higher energy with increasing CEP (adding -6 fs^2 of chirp would make them move to lower kinetic energy).

predictions for the case of the measured laser spectrum both as a transform-limited pulse and with a small chirp of 6 fs^2 are shown in Figures 5.5 (b) and (c), respectively. The positive chirp on the laser pulse makes the regions of maximal asymmetry move to higher energy with higher CEP. Now it is also clear why there are certain special photoelectron energies in Figure 5.2 with no asymmetry in the photoelectron distribution, regardless of the CEP. These are places in the spectrum at the tops of the photoelectron peaks, where for the laser pulse bandwidth used, there are quantum paths with only one photon number that contribute significantly to the photoionization amplitude. With no contribution from opposite parity partial waves there is no interference, regardless of the CEP or chirp, as in panels (b) and (c) of Figure 5.5. Thus, long pulses with narrow bandwidths would lead to zero asymmetry in the photoelectron spectrum even if the CEP were stabilized.

5.5 Chirp Dependence

The preceding model confirms that some residual chirp remains on the pulse used for the experiment presented in Figure 5.2. Figure 5.6 (b) shows raw asymmetry data that indicates that after optimizing the laser pulse to reduce the chirp (at the cost of lower peak intensity and therefore count rate), the linear CEP-dependence of the positions of maximum

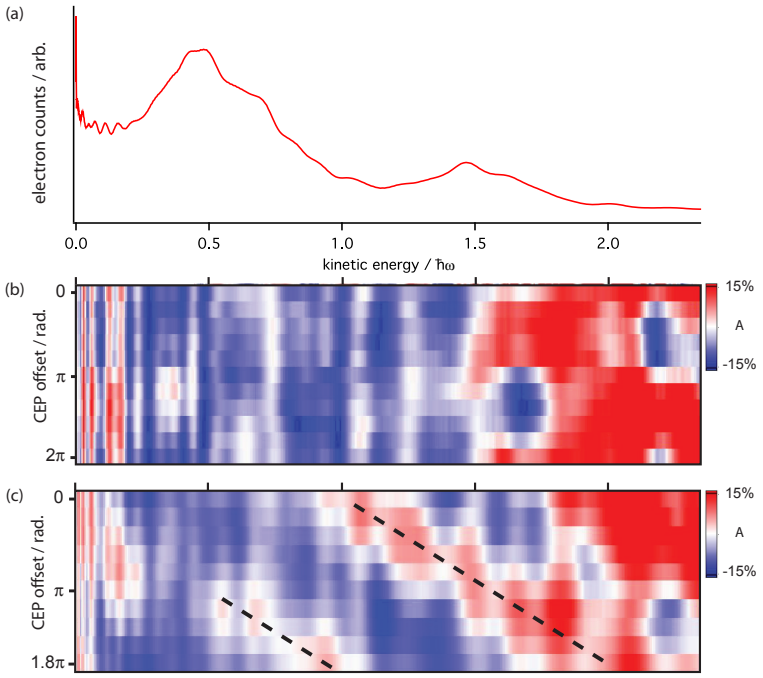

Figure 5.6: Chirp dependence of the asymmetry. **a.** A typical photoelectron spectrum for the chirp-dependence measurements, showing two photoelectron peaks separated by the laser photon energy. **b.** When the laser pulse is carefully optimized for flat spectral phase, the regions of maximum asymmetry do not move in energy with varying CEP. **c.** After propagation through 160 μm of fused silica, the regions of maximum asymmetry, emphasized by the dotted lines, move with CEP in qualitative agreement with the prediction in Figure 5.5 (c).

constructive and destructive interference disappears. Some CEP-dependent asymmetry variations persist, possibly a result of higher-order spectral phase contributions from the laser pulse and spatial inhomogeneity in the detector dark count rate. Upon chirping the pulse by propagation through an extra 160 μm of fused silica, which imparts approximately 6.4 fs^2 of chirp, the linear pattern of Figure 5.2 (c) returns (Figure 5.6 (c)), qualitatively supporting the multiphoton model.

As a final note, we would like to point out that because ionization is a bound-free transition, the variation of the signal with CEP repeats every 2π radians. If a bound-bound transition like absorption were instead employed, the same multiphoton model would apply but the result would be a π-periodicity in the CEP measurement because in that case the parity selection rule only allows N-photon pathways to interfere with N+2-photon pathways. So, moving away from photoelectron spectroscopy to absorption or fluorescence measurements in atoms could enable single-pulse determination not of ϕ_{CEP} but rather of ϕ_{CEP} mod π.

5.6 Summary

When Xe atoms are ionized with 7 fs, CEP-stabilized laser pulses with peak intensity in the perturbative regime, the resulting photoelectron angular distributions are asymmetric along the polarization direction of the laser. The asymmetry depends on the energy of the photoelectron and the CEP of the laser pulse. The underlying mechanism for the observed asymmetry is quantum interference between equivalent pathways involving different numbers of photons. This mechanism is general to processes driven by perturbative laser pulses, including absorption, nonlinear optical frequency conversion, and even coherent control. Indeed, the mechanism can be thought of as the basis for strong-field CEP effects as well, though in that regime more than just two quantum pathways lead to the same final state. This mechanism also opens the way to single-pulse determination of the CEP using perturbative fields as well as absolute phase spectroscopy of atoms for the investigation of scattering processes.

The response of electrons to the attosecond variation of a laser pulse electric field is the subject of the next chapter as well. In the case of ATI, the response is microscopic in nature–there is no influence of the extended sample gas medium on the results. But in fact macroscopic behavior is important for attosecond science as well, as demonstrated by measurements in chapter 6 showing the ultrafast evolution of phase-matching during high harmonic generation.

Chapter 6

Isolated Attosecond Pulse Generation

The contents of this chapter have been published in Chem. Phys., **366**, 9 (2009)*, reference [103].*

6.1 Introduction

The unprecedented temporal resolution offered by isolated attosecond pulses (IAPs) is opening a new field of physics and chemistry. Electronic motion in atoms[133], molecules, nanoparticles[26], and solids[21] can be probed in real time by using attosecond pulses overlapped with a phase-locked visible field. To achieve isolated attosecond pulses, soft x-ray light is generated by high-harmonic generation. The quasi-classical 3-step model[76] of the microscopic process of HHG enables intuitive understanding and control over the harmonic generation process in the tunneling regime, ignoring the quantum mechanical interferences that determine electron dynamics in experiments with weaker driving laser fields [111, 134, 135].

Indeed, controlling the three steps of high-harmonic generation on a single-atom scale offers opportunities to generate isolated attosecond pulses, as discussed in chapter 2. For example, IAPs have been produced by varying the kinetic energy of the returning electron using the intensity variation of a few-cycle driving pulse[128], as well as by guiding the electrons' continuum motion by modulating the polarization of the driving pulse[98, 136]. Two-color (heterodyne) schemes[94, 137–140], in which the time-dependent intensity of the driving laser is modulated by mixing it with light of another color, appear quite promising but so far have not been directly proven to yield IAPs. Finally, combinations of the above methods have been investigated theoretically[141, 142] and experimentally[99, 100].

These methods of IAP production are generally interpreted in terms of the microscopic response of individual atoms in the generation medium. In this chapter a somewhat different approach, ionization gating, is presented. Ionization gating offers the possibility of producing IAPs under less stringent conditions than other methods[102]. Moreover, it allows the attosecond pulse to be tuned over a large frequency range merely by varying the CEP. Ionization gating has a macroscopic origin, relying on a sub-femtosecond loss of phase matching during the leading edge of the driving pulse[101]. In ionization gating, which is illustrated schematically in Figure 6.1(b), the intensity of the driving laser pulse is increased so that during the leading edge of the driving pulse the time-dependent ionization of the harmonic

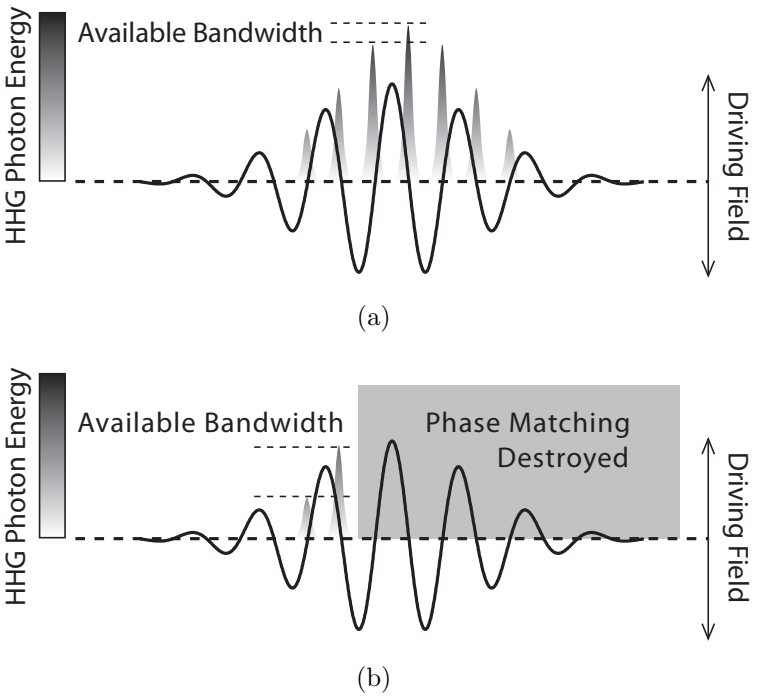

Figure 6.1: **Traditional vs. ionization-gated IAP production.** In early experiments with isolated attosecond pulses, the harmonic pulse corresponding to the strongest half-optical cycle of the visible driver pulse was isolated using a spectral filter. The available bandwidth is determined by the intensity difference between adjacent half-cycles near the peak of the driver pulse. In the ionization gating method, the intensity difference (and therefore the attosecond pulse bandwidth) can be much larger because of the rapid variation of the driver pulse intensity on the leading edge of the driver pulse.

generation medium rises above the critical ionization level. At this plasma density, the negative dispersion due to free electrons cannot be compensated by the positive dispersion of the remaining neutral generation gas[143]. As a consequence, phase matching of the harmonic emission is no longer possible, thereby gating the harmonic emission on the leading edge of the driving laser pulse.

In the following sections, we first verify ionization gating conditions in the harmonic emission process using half-cycle cutoff (HCO) analysis[144], which allows the highest photon energies associated with individual bursts in the attosecond pulse train to be measured. As can be seen in Figure 6.1(a), for the non-gated case an attosecond pulse can be obtained at the very peak of the driving laser intensity envelope. In that case, the half-cycle cutoff energies will show a roughly Gaussian dependence on emission time, corresponding to the intensity envelope of the driving pulse. However, if the ionization gate closes before the peak of the pulse (Figure 6.1(b)), the HCO energy depends nearly linearly on emission time. Previous HCO analyses[101, 102] showed that broadband x-ray emission that is strongly indicative of IAPs could be obtained by the ionization gating method, but the temporal structure of the pulses was not measured. Here, we present a measurement of the contrast ratio of the IAPs, defined as the energy in the main IAP compared to the energy in any adjacent satellite pulses.

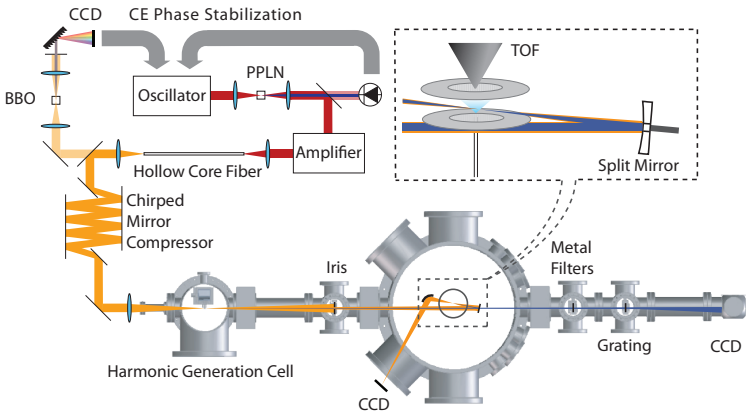

Figure 6.2: **Apparatus.** The output of the amplifier is spectrally broadened and temporally recompressed before HHG in the vacuum chamber. In vacuum, an iris varies the amount of 730 nm light reaching the interaction region. A metal filter on a pellicle passes only x-rays on the beam axis, reducing the visible beam to an annular shape. The pulses are focused into the interaction region by a split mirror, the inner portion of which is mounted on a piezoelectric translation stage and reflects the x-rays, while the outer portion reflects the visible light. Photoelectrons generated in the interaction region are analyzed by a time-of-flight detector.

Also, time-resolved optical streaking using a direct atomic ionization process is carried out to further confirm the isolated nature of the ionization-gated harmonic emission and to measure the duration of the attosecond pulse.

6.2 Experimental Details

The apparatus was discussed in detail in chapter 3, so only the relevant portions are reiterated here. At the heart of the experimental apparatus (Figure 6.2) is a 25 fs, 0.8 mJ Ti:Sapphire laser system operating at 3 kHz, with central wavelength 800 nm. The carrier–envelope phase is locked (0.3 rad RMS error) using a home-built feedback loop. Difference frequency mixing of the oscillator output in a PPLN crystal provides a second pulse train with zero carrier–envelope offset frequency to which the oscillator output is compared[92, 116, 145].

The laser output is focused into a capillary waveguide filled with neon gas at a pressure of 2 bar, where self-phase modulation broadens the spectrum and simultaneously shifts the central wavelength to about 730 nm[146–148]. The broadened capillary output is temporally compressed to ∼7 fs by a set of chirped mirrors. The light transmitted through the first chirped mirror is sent to an f-2f interferometer to monitor and correct CEP drifts in the amplifier[149]. The chirped mirrors also precompensate for the dispersion caused by propagation through air and glass between the compressor and the HHG cell. The remainder of the compressed pulse is focused into the harmonic generation cell by a $f = 50$ cm mirror. The Rayleigh range is approximately 9 mm.

High-harmonic light is generated in a 2 mm path-length cell with pinholes drilled for the laser entrance and exit. The pressure in the HHG cell is ∼100 mbar. For the half-cycle cutoff

measurements, the 730 nm light is filtered out of the combined beam path by two 200 nm thick zirconium filters and the remaining harmonic light is dispersed by a Si_3N_4 transmission grating with 100 nm period. The harmonic spectrum is recorded by a back-illuminated CCD camera with an acquisition time of 100 ms. Twenty harmonic spectra are recorded per CEP offset value.

For the CEP-scanning experiment[17], both the 730 nm driving pulse and the x-ray pulses are reflected from a multilayer Mo/Si mirror. The mirror has a reflectivity band in the x-ray region centered at 93 eV with 4 eV FWHM and about 70% peak reflectivity, as well as $\simeq$50% reflectivity across the entire visible and near-IR range. The mirror diameter is 3 mm, with a 12.5 cm focal length. The x-ray pulses ionize neon atoms introduced from an effusive nozzle. Photoelectrons are accelerated by the intense laser field according to the instantaneous value of the vector potential at the time of their release[128].

The kinetic energy spectrum of the electrons is recorded using a linear time-of-flight spectrometer. The spectrometer consists of a 1 mm hole in an entrance cone, a 60 cm field-free flight tube, and a 25 mm diameter MCP detector. The energy resolution of the TOF is limited by the multichannel scaler used to count electron hits, which has 1 ns bin times. Typical flight times for the fastest electrons are around 150 ns. The solid angle of detection for the TOF spectrometer is determined by the MCP.

For the time-resolved optical streaking measurement, the 730 nm light is filtered out of the central portion of the beam path by a 200 nm thick zirconium filter. The harmonic radiation continues to the inner multilayer mirror while the 730 nm pulse is reflected by an outer annular mirror of 1 inch diameter with a 3.5 mm hole, also coated with the Mo:Si multilayer structure. The temporal delay between the two pulses can be adjusted by moving the inner mirror along the beam axis using a feedback-controlled piezoelectric actuator.

6.3 HCO Analysis

A typical HHG spectrum for the CEP-locked driver pulse is shown in Figure 6.3. When the spectrum is Fourier filtered to remove the modulation at twice the laser frequency ($2\omega_L$), broad maxima become discernible. The energies of these maxima correspond to the cutoff energies of the individual half-cycle harmonic emission events[144]. Since the cutoff energy E_{HCO} scales linearly with the time-dependent intensity $I(t)$ of the driving laser (and the target gas ionization potential I_P) via the cutoff law[150, 151],

$$E_{HCO} = 3.17U_p + I_P \tag{6.1}$$

$$U_p = \frac{I(t)}{4\omega_L^2}, \tag{6.2}$$

the maxima in the harmonic spectrum also yield information about the time-dependent intensity of the driving pulse during the HHG emission time. Equations 6.1 and 6.2 are in atomic units.

Collecting many such spectra as a function of the CEP yields the results in Figure 6.4. The HCO positions as a function of CEP are marked by black dots. Unfolding the π ambi-

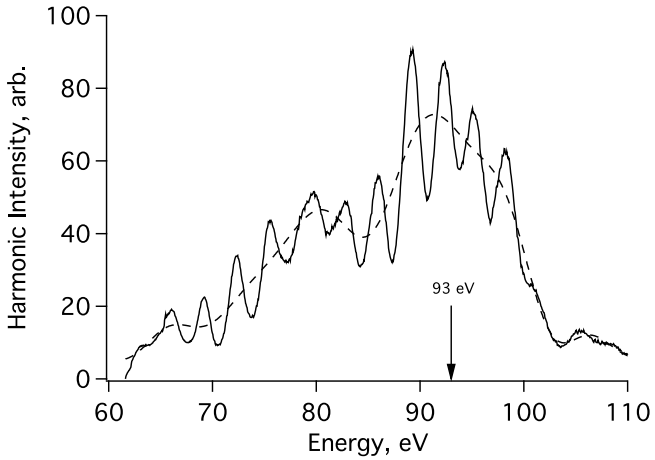

Figure 6.3: **Harmonic spectrum** (solid line) and Fourier filtered spectrum (dashed line) at a CEP offset of 0.4 π rad showing HCOs at 93 eV and 80 eV.

guity in the data and converting the CEP to a relative time value using the carrier frequency of the laser pulse, the time-dependent intensity of the driver pulse during the harmonic emission is recovered. In Figure 6.5, the HCO positions are least-squares fit by an 8 fs half-width Gaussian function with a peak intensity $5.25 \pm 0.10 \times 10^{14}$ W/cm^2. The error estimate on the intensity value is not derived from the least-squares fitting procedure (which yields an artificially small error), but is generated using the ionization gate closure time, as discussed below.

Using the cycle-averaged Ammosov-Delone-Krainov (ADK) ionization rate[120] one can compute the ionization fraction as a function of time. The rate, with all quantities in atomic units, is[119]

$$\eta(t) = \omega_A C_{n^*}^2 f(l,m) I_p \left(\frac{3\epsilon(t)}{\pi(2I_p)^{3/2}}\right)^{1/2} \times \left(\frac{2(2I_p)^{3/2}}{\epsilon(t)}\right)^{2n^*-|m|-1} exp\left(-\frac{2(2I_p)^{3/2}}{3\epsilon(t)}\right) \tag{6.3}$$

with ω_A the atomic unit of frequency, $\epsilon(t)$ the electric field amplitude, and I_p the ionization potential. The ionization proceeds from states with $l = 1$, $m = 0, \pm 1$ and $n^* = Z \times (2I_p)^{-1/2}$ ($Z = 1$ being the final charge of the ion core). The factors f and C are:

$$f(l,m) = \frac{(2l+1)(l+|m|)!}{2^{|m|}(|m|)!(l-|m|)!} \tag{6.4}$$

and

$$C_{n^*} = \left(\frac{2e}{n^*}\right)^{n^*} \frac{1}{\sqrt{2\pi n^*}} \tag{6.5}$$

with e the base of the natural logarithm.

The extent of ionization, determined as a function of time according to equation 6.3, is

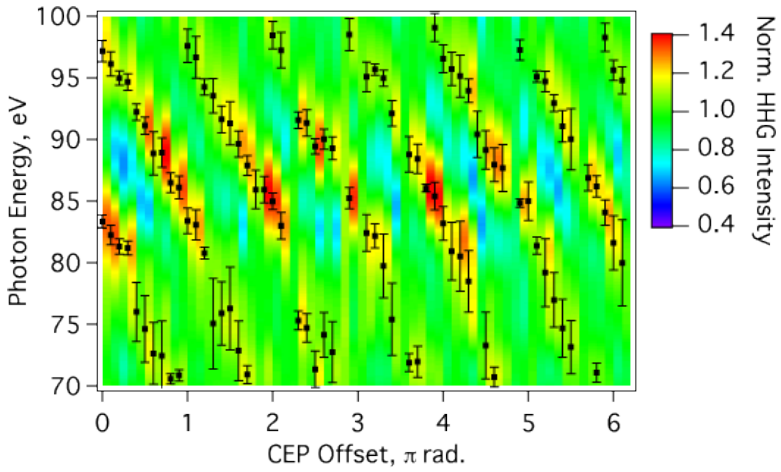

Figure 6.4: **Normalized harmonic intensity** versus energy and CEP offset. The $2\omega_L$ modulation is removed by Fourier filtering. Black dots indicate maxima in the spectrum with error bars corresponding to the standard deviation of the HCO positions in the 20 spectra recorded per CEP offset. The linear dependence of the HCO position on CEP is indicative of ionization gating of HHG on the leading edge of the driving pulse.

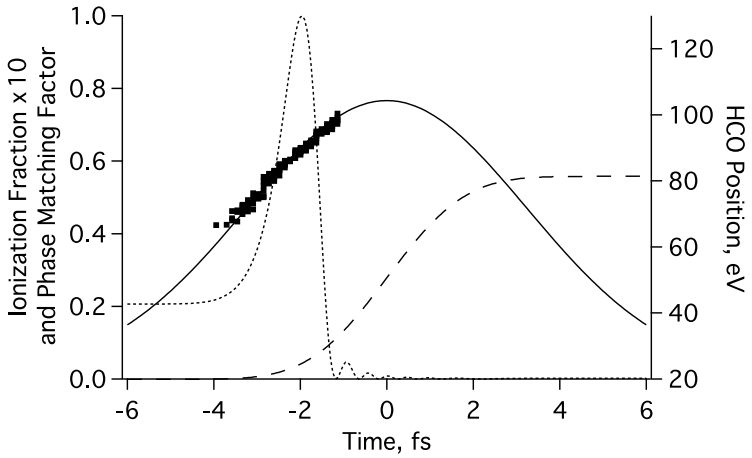

Figure 6.5: **HCO positions** (black squares) are fit to an 8 fs Gaussian pulse (solid line) with $5.25 \pm 0.10 \times 10^{14}$ W/cm^2 peak intensity. The ionization fraction (dashed line) calculated by the ADK formula grows to approximately 5% by the end of the pulse. The phase matching factor (dotted line) initially grows then suddenly drops to zero as the ionization fraction exceeds ∼1%.

used to calculate the phase slip between the harmonics and the driving field. This phase slip Δk consists of three terms accounting for the plasma dispersion, the linear dispersion of the generating medium, and the Gouy phase respectively[143]:

$$\begin{aligned}\Delta k &= qk_\omega - k_{q\omega} \\ &= P\eta(t)N_{atm}r_e\left(q\lambda - \frac{\lambda}{q}\right) \\ &\quad -P\frac{2\pi(1-\eta(t))q}{\lambda}\Delta\delta \\ &\quad -(q-1)\frac{\partial}{\partial z}\arctan\left(\frac{z}{z_R}\right)\end{aligned} \tag{6.6}$$

Here, P is the pressure in atmospheres, $\eta(t)$ is the time-dependent ionization fraction, N_{atm} is the number density of one atmosphere, $r_e = 2.82 \times 10^{-15}$ m is the classical electron radius, and λ is the driving field wavelength. The harmonic order is given by q; $\Delta\delta$ is the difference in refractive indices for the driver and harmonic at one atmosphere; z is the gas cell distance from the focus; and z_R is the Rayleigh range, which is the focal spot area divided by the wavelength. The atomic dipole phase [143, 152] was neglected for this calculation because its effect on the calculated gate closure time is less than the temporal resolution of the HCO experiment (0.2π rad $\simeq$ 270 as).

Comparing the time resolution of the HCO experiment to the change of t_g with intensity, where t_g is the calculated ionization gate closure time, yields the previously-quoted error estimate of $\pm 0.10 \times 10^{14}$ W/cm^2

Using equation 6.6, the coherence length is $L_c = \pi/\Delta k$ and the phase matching factor is $F = sinc^2(\pi L/2L_c)$ with L the effective harmonic generation medium length. Here, an effective cell thickness of 3 mm accounting for gas leaking from the holes in the cell, a pressure of 100 mbar, a distance of 11 mm from the focus to the cell, and a Rayleigh range of 9 mm, corresponding to the actual HHG geometry, are employed. As can be seen in Figure 6.5, a very rapid loss of phase matching occurs near -1.2 fs, curtailing HHG on the leading edge of the pulse.

At such high intensities and gas densities, both spatial and temporal pulse reshaping are expected to occur. Because the HCO analysis is sensitive to the leading edge of the driving pulse, it cannot reveal distortions that occur later in time.

By tuning the CEP it is possible to spectrally overlap one HCO with the multilayer mirror reflectivity band centered at 93 eV. The HCO energy dependence indicates that this would be possible near a CEP offset of 0.4 π rad. However, whether the x-ray emission actually comprises an IAP at this CEP offset is unclear since the recorded raw x-ray spectra are modulated by the spectral overlap of neighboring HCOs (Figure 6.3) and do not show a smooth continuum. Nevertheless, an IAP could be anticipated in light of the fact that a hypothetical 10% intensity harmonic pre-pulse would cause nearly a 40% modulation depth in the spectrum. Techniques to unravel and evaluate temporally separated HCO emission occurring at the same photon energy are presented in the next sections.

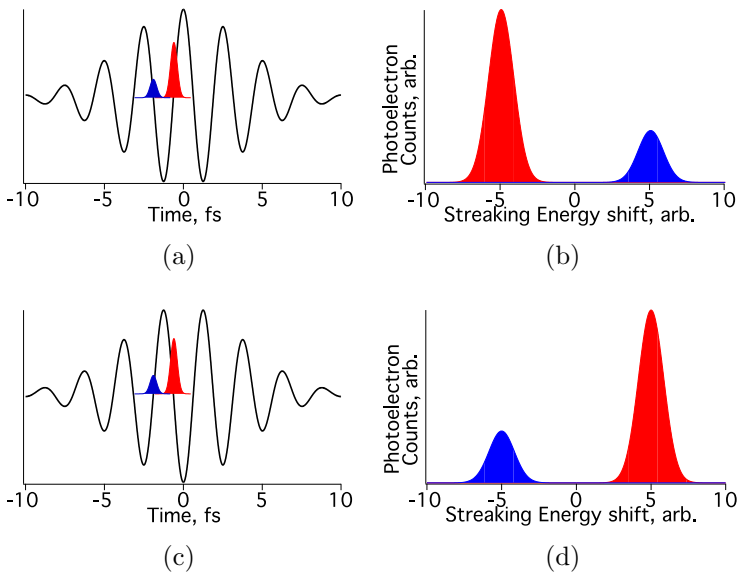

Figure 6.6: **Principle of the CEP-scanning method** for attosecond pulse contrast retrieval. Using the vector potential of the driving laser to alter the photoelectron momentum enables separation of ionization events in the main x-ray pulse from satellites spaced half an optical cycle earlier or later. Comparing the "up-streaked" (or "down-streaked") photoelectron signal before (panels a–b) and after (panels c–d) changing the CEP by π enables direct contrast retrieval. Alternatively, the up-streaked and down-streaked peaks may be compared directly at fixed CEP.

6.4 CEP-Scanning

To assess the degree of isolated attosecond pulse production, we employ the technique of CEP scanning recently introduced by our group in Ref. [17]. CEP scanning works in the following way. The HCO emission events described in Section 6.3 come at the zero-crossing times of the driving electric field[153], because they are composed of cutoff harmonics. Since the zero-crossing of the field is a maximum in the vector potential, electrons ionized by the cutoff harmonics (HCOs) receive a large momentum kick in either the upward or downward direction, if the time delay between the harmonic light and the intense streaking field is held at zero (e.g., when both pulses are refocused into the interaction region by the same mirror). Electrons born into the continuum during consecutive half-cycles will receive momentum kicks in opposite directions and therefore the attosecond electron emission from neighboring half-cycles can be observed and compared. This allows measurement of the attosecond pulse contrast as a function of CEP, as illustrated in Figure 6.6. Not only can neighboring half-cycle harmonic bursts be compared, but the IAP contrast in the interaction region can be mapped in this way as a function of CEP.

Figure 6.7 shows the experimental photoelectron spectrum of neon gas as a function of CEP. The photoelectron signal, which would come near 70 eV in the absence of a streaking field, splits into two components, one higher and one lower in energy. With only two CEP-dependent peaks in the photoelectron spectrum, the contrast can be measured between a

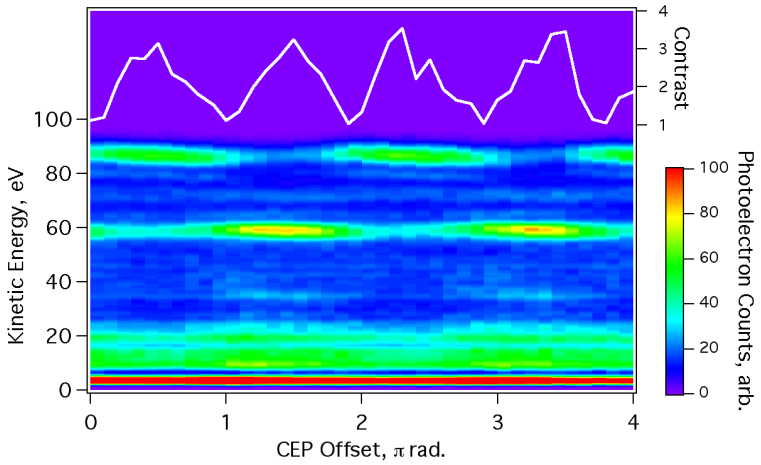

Figure 6.7: **CEP-dependent photoelectron spectrum** of Ne at zero time delay between the x-ray bursts and the streaking field. The attosecond pulse contrast (white line) is retrieved from the CEP-dependent intensity of the peaks near 60 eV and 90 eV.

central pulse and up to two satellite pulses spaced single half-cycles away in time. Subtracting a linear background over the analyzed energy range and then comparing the up-streaked peak area between CEP values separated by π yields $c = 3.3 \pm 0.2$ (average $\pm$ standard deviation of the four contrast maxima shown in the white line in Figure 6.7) for the optimal CEP offset value of 0.5π radians. The same result is obtained by comparing the two peak areas at fixed CEP offset. The CEP offset value maximizing c is slightly different from the value anticipated from the HCO analysis because some harmonic flux from multiple half-cycles of the driving pulse, not just the one producing an HCO centered at 93 eV, reflects off the multilayer mirror and needs to be accounted for.

We emphasize that although this contrast measurement scheme is limited to comparing one main IAP to neighboring pulses that are offset by half an optical cycle, it is general to all methods of IAP generation that depend on the CEP.

6.5 Optical Streaking

Finally, we use time-resolved-optical streaking[128] with the split-mirror configuration described in Section 6.2 to confirm that ionization gating produces isolated attosecond pulses. A sufficiently well-resolved spectrogram (photoelectron spectrum versus time delay) contains enough information for the full determination of both the HHG and driver pulse shapes[108]. The experimental time-resolved photoelectron spectrum of neon atoms is shown in Figure 6.8 as a function of infrared pulse time delay. Visually, one can observe the individual half-cycles of the driving electric field, which alternately accelerate the attosecond photoelectron wavepacket upwards and downwards. The white arrows separated by the optical period (2.4 fs) mark the full-optical-cycle periodicity in the photoelectron streaking, which would be averaged over in the case of an x-ray pulse longer than the half-cycle time.

The spectrogram can be fit using a Monte Carlo method in which suitably parametrized

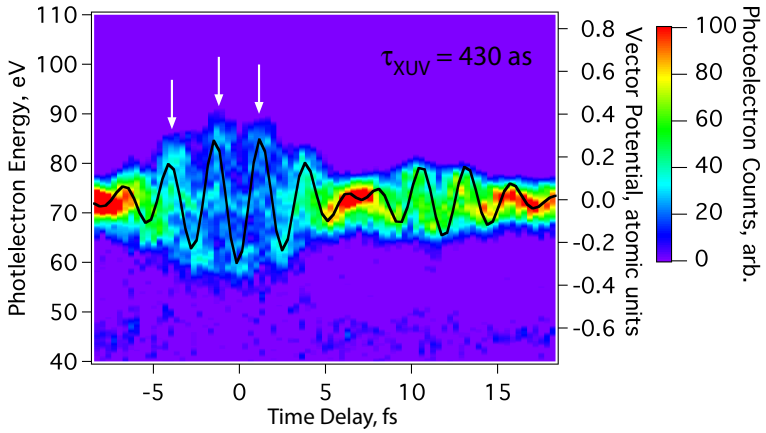

Figure 6.8: **Streaking spectrogram** Streaking spectrogram showing the isolated nature of the attosecond pulse. The streaked phoeoelectron spectrum, shown versus infrared pulse delay time, reveals the duration of the XUV pulse to be 430 ± 15 as. It also reveals the vector potential of the infrared pulse, shown by the black line, which is a 7 fs Gaussian shape with a prepulse.

XUV and infrared pulses are chosen at random, a trial spectrogram is calculated and blurred according to the instrumental resolution, and the result compared to the experiment. If the mean squared error (MSE) is reduced with respect to the previous best fit, the current guess is taken as the new best fit. An adjustable numerical "temperature" enables the best fit to be updated (with Boltzmann probability) to a guess with a larger value of MSE. The initial parameters are chosen by hand in an effort to minimize the starting MSE, and the step size in any direction in parameter space is limited to be less than $\pm 5\%$ the initial parameter value corresponding to that direction.

There are drawbacks to the Monte Carlo method, including significantly slower convergence than FROG-CRAB[108, 109]. Further, the method can be very insensitive to a certain pulse parameter if the gradient of the MSE function in that direction of parameter space is small. In this case, a different parameterization of the pulses is required. However, for noisy data sets our technique has the advantage over the FROG-CRAB method that the number of parameters is reduced from hundreds to a handful (on the order of 10). This strongly restrains the program from attempting to match noise by guessing an extremely complicated vector potential, a common problem we have experienced using FROG-CRAB on noisy data sets.

The attosecond pulse contrast is fixed at the previously-measured value of 3.3, and the carrier frequency is fixed at 2.35 fs^{-1}. The retrieved attosecond pulse duration is 430 ± 15 as, roughly consistent with the 450 as bandwidth limit for reflection off the 4 eV bandwidth XUV mirror. That the pulses delivered to the interaction region are nearly transform limited is a result of their position at the cutoff of the HHG spectrum, where the temporal phase has (to a first approximation) no quadratic component[153].

The vector potential of the driving pulse is also retrieved, which corresponds to a 7 fs Gaussian intensity profile with a small prepulse, consistent with the HCO measurement. Pre-

and postpulses commonly accompany ultrashort pulses because of the difficulty in producing and phase-compensating ultra-broad-bandwidth laser sources, but the measured prepulse is not intense enough to ionize the harmonic generation medium and so it does not produce harmonics or contribute toward the critical ionization threshold discussed in Section 6.3.

The time-dependent streaking results not only confirm the conclusions of the previous sections, but also illustrate some interesting points about the ionization-gating regime of HHG. The closure of the ionization gate relies on an ultrafast loss of phase matching. Isolated attosecond pulse production is an indication that the index of refraction of the target gas can change on the attosecond timescale, a surprisingly fast time for changes in a *macroscopic* property. Furthermore, the results demonstrate that the idea of an unmodulated x-ray continuum being required for useful isolated attosecond pulses is overly cautious. In fact, a very small x-ray satellite pulse can lead to a large modulation depth in the spectrum, and this fact speaks to the need for temporal characterization techniques to determine the structure of attosecond x-ray fields. Besides the time-resolved streaking shown in this section, the CEP-scan is an extremely useful and fast way to accomplish this.

6.6 Conclusion

Ionization gating of HHG emission is shown to produce isolated attosecond pulses with variable, CEP-dependent contrast. The ionization gate is perhaps the most explicit example so far of the *selection* (rather than simply *generation*) of an attosecond pulse by a combination of microscopic and macroscopic factors, as discussed by Gaarde and co-workers[154].

The isolated nature of the pulse is characterized with the newly developed method of CEP-scanning and confirmed by time-resolved optical streaking. Since the ionization gating scheme is scalable to longer, multicycle driver pulses, we anticipate that IAP production using the ionization gating method is also achievable using long pulses. Indeed, an interesting step in that direction has recently been achieved in Ref. [155], where subfemtosecond pulses were demonstrated using 15 fs drivers without carrier–envelope phase stabilization. By implementing ionization gating with such driver pulses with CEP stabilization, isolated tunable attosecond pulses with no timing jitter with respect to the driver laser intensity envelope (as occurs without CEP stabilization) can be generated without the need to resort to more complicated schemes involving multiple colors or polarization control.

The implementation of isolated pulse production will enable probing of ultrafast attosecond electron dynamics in atoms and molecules. Experimental access to highly excited molecules and atoms, interatomic electron decay mechanisms, couplings between core levels in molecules and atoms, and many other applications discussed in chapter 1 is now available. Considering the rapid advancement of attosecond sources, the future of attosecond science in physics, chemistry, and biology seems bright.

Bibliography

[1] A. H. Zewail. *Angew. Chem. Int. Ed.*, **39** (15), 2587 (2000).

[2] C. Rulliére (editor). *Femtosecond Laser Pulses: Principles and Experiments*. Springer, New York, USA, 2nd edition (2005).

[3] Z.-H. Loh, M. Khalil, R. E. Correa, R. Santra, C. Buth, and S. R. Leone. *Phys. Rev. Lett.*, **98** (14), 143601 (2007).

[4] Z.-H. Loh and S. R. Leone. *J. Chem. Phys.*, **128** (20), 204302 (2008).

[5] Z.-H. Loh, M. Khalil, R. E. Correa, and S. R. Leone. *Rev. Sci. Instrum.*, **79** (7), 073101 (2008).

[6] L. Nugent-Glandorf, M. Scheer, D. Samuels, V. Bierbaum, and S. Leone. *Rev. Sci. Instrum.*, **73** (4), 1875 (2002).

[7] M. Protopapas, C. H. Keitel, and P. L. Knight. *Rep.Prog. Phys.*, **60** (4), 389 (1997).

[8] F. Krausz and M. Ivanov. *Rev. Mod. Phys.*, **81** (1), 163 (2009).

[9] T. Shintake, H. Tanaka, T. Hara, T. Tanaka, K. Togawa, M. Yabashi, Y. Otake, Y. Asano, T. Bizen, T. Fukui, S. Goto, A. Higashiya, T. Hirono, N. Hosoda, T. Inagaki, S. Inoue, M. Ishii, Y. Kim, H. Kimura, M. Kitamura, T. Kobayashi, H. Maesaka, T. Masuda, S. Matsui, T. Matsushita, X. Marechal, M. Nagasono, H. Ohashi, T. Ohata, T. Ohshima, K. Onoe, K. Shirasawa, T. Takagi, S. Takahashi, M. Takeuchi, K. Tamasaku, R. Tanaka, Y. Tanaka, T. Tanikawa, T. Togashi, S. Wu, A. Yamashita, K. Yanagida, C. Zhang, H. Kitamura, and T. Ishikawa. *Nat. Photonics*, **2** (9), 555 (2008).

[10] G. Lambert, T. Hara, D. Garzella, T. Tanikawa, M. Labat, B. Carre, H. Kitamura, T. Shintake, M. Bougeard, S. Inoue, Y. Tanaka, P. Salieres, H. Merdji, O. Chubar, O. Gobert, K. Tahara, and M. E. Couprie. *Nat. Phys.*, **4** (4), 296 (2008).

[11] P. Tzallas, D. Charalambidis, N. Papadogiannis, K. Witte, and G. Tsakiris. *Nature*, **426** (6964), 267 (2003).

[12] T. Sekikawa, A. Kosuge, T. Kanai, and S. Watanabe. *Nature*, **432** (7017), 605 (2004).

[13] N. Papadogiannis, L. Nikolopoulos, D. Charalambidis, G. Tsakiris, P. Tzallas, and K. Witte. *Phys. Rev. Lett.*, **90** (13), 133902 (2003).

[14] E. P. Benis, P. Tzallas, L. A. A. Nikolopoulos, M. Kovacev, C. Kalpouzos, D. Charalambidis, and G. D. Tsakiris. *New J. Phys.*, **8**, 92 (2006).

[15] T. Okino, K. Yamanouchi, T. Shimizu, R. Ma, Y. Nabekawa, and K. Midorikawa. *J. Chem. Phys.*, **129** (16), 161103 (2008).

[16] E. Goulielmakis, V. S. Yakovlev, A. L. Cavalieri, M. Uiberacker, V. Pervak, A. Apolonski, R. Kienberger, U. Kleineberg, and F. Krausz. *Science*, **317** (5839), 769 (2007).

[17] T. Pfeifer, M. Abel, P. Nagel, and W. Boutu. *Opt. Lett.*, **34**, 1819 (2009).

[18] E. Constant, V. D. Taranukhin, A. Stolow, and P. B. Corkum. *Phys. Rev. A: At. Mol. Opt. Phys.*, **56** (5), 3870 (1997).

[19] M. Drescher, M. Hentschel, R. Kienberger, M. Uiberacker, V. Yakovlev, A. Scrinzi, T. Westerwalbesloh, U. Kleineberg, U. Heinzmann, and F. Krausz. *Nature*, **419** (6909), 803 (2002).

[20] J. A. D. Matthew and Y. Komninos. *Surf. Sci.*, **53**, 716 (1975).

[21] A. Cavalieri, N. Muller, T. Uphues, V. Yakovlev, A. Balthuska, B. Hovrath, B. Schmidt, L. Blumel, R. Holzwarth, S. Hendel, M. Drescher, U. Kleineberg, P. Echenique, R. Kienberger, F. Krausz, and U. Heinzmann. *Nature*, **449**, 1029 (2007).

[22] C.-H. Zhang and U. Thumm. *Phys. Rev. Lett.*, **102** (12), 1 (2009).

[23] A. Kazansky and P. Echenique. *Phys. Rev. Lett.*, **102** (17), 1 (2009).

[24] C. Lemell, B. Solleder, K. Tőkési, and J. Burgdörfer. *Phys. Rev. A*, **79** (6), 1 (2009).

[25] M. I. Stockman, M. F. Kling, U. Kleineberg, and F. Krausz. *Nat. Photonics*, **1** (9), 539 (2007).

[26] T. Pfeifer, M. J. Abel, P. M. Nagel, A. Jullien, Z.-H. Loh, M. J. Bell, D. M. Neumark, and S. R. Leone. *Chem. Phys. Lett.*, **463** (1-3), 11 (2008).

[27] Z.-H. Loh. *Nature* (Submitted).

[28] R. Santra, J. Zobeley, L. S. Cederbaum, and N. Moiseyev. *Phys. Rev. Lett.*, **85**, 4490 (2000).

[29] R. Santra, J. Zobeley, and L. S. Cederbaum. *Phys. Rev. B: Condens. Matter*, **64** (24), 10 (2001).

[30] N. Moiseyev, R. Santra, J. Zobeley, and L. S. Cederbaum. *J. Chem. Phys.*, **114** (17), 7351 (2001).

[31] S. Marburger, O. Kugeler, and U. Hergenhahn. *Phys. Rev. Lett.*, **90**, 203401 (2003).

[32] T. Jahnke, A. Czasch, M. S. Schoffler, S. Schossler, A. Knapp, M. Kasz, J. Titze, C. Wimmer, K. Kreidi, R. E. Grisenti, A. Staudte, O. Jagutzki, U. Hergenhahn, H. Schmidt-Bocking, and R. Dorner. *Phys. Rev. Lett.*, **93**, 163401 (2004).

[33] G. Ohrwall, M. Tchaplyguine, M. Ludwall, R. Feifel, H. Bergersen, T. Rander, A. Lindblad, J. Schultz, S. Peredkov, S. Barth, S. Marburger, U. Hergenhahn, S. Svensson, and O. Bjorneholm. *Phys. Rev. Lett.*, **93**, 173401 (2004).

[34] W. Domcke, L. S. Cederbaum, J. Schirmer, W. von Niessen, C. E. Brion, and K. H. Tan. *Chemical Physics*, **40** (1-2), 171 (1979).

[35] D. Strasser, L. H. Haber, B. Doughty, and S. R. Leone. *Mol. Phys.*, **106** (2-4), 275 (2008).

[36] A. Staudte, D. Pavicic, S. Chelkowski, D. Zeidler, M. Meckel, H. Niikura, M. Schoeffler, B. Ulrich, P. P. Rajeev, T. Weber, T. Jahnke, D. M. Villeneuve, A. D. Bandrauk, C. L. Cocke, P. B. Corkum, and R. Doerner. *Phys. Rev. Lett.*, **98** (7), 073003 (2007).

[37] M. F. Kling, C. Siedschlag, I. Znakovskaya, A. J. Verhoef, S. Zherebtsov, F. Krausz, M. Lezius, and M. J. J. Vrakking. *Mol. Phys.*, **106** (2-4), 455 (2008).

[38] K. P. Singh, F. He, P. Ranitovic, W. Cao, S. De, D. Ray, S. Chen, U. Thumm, A. Becker, M. M. Murnane, H. C. Kapteyn, I. V. Litvinyuk, and C. L. Cocke. *Phys. Rev. Lett.*, **104** (2), 023001 (2010).

[39] I. Znakovskaya, P. von den Hoff, S. Zherebtsov, A. Wirth, O. Herrwerth, M. J. J. Vrakking, R. de Vivie-Riedle, and M. F. Kling. *Phys. Rev. Lett.*, **103** (10), 103002 (2009).

[40] J. Breidbach and L. S. Cederbaum. *J. Chem. Phys.*, **118** (9), 3983 (2003).

[41] R. Weinkauf, P. Schanen, A. Metsala, E. Schlag, M. Burgle, and H. Kessler. *J. Phys. Chem.*, **100** (47), 18567 (1996).

[42] R. Weinkauf, E. Schlag, T. Martinez, and R. Levine. *J. Phys. Chem. A*, **101** (42), 7702 (1997).

[43] F. Remacle, M. Nest, and R. D. Levine. *Phys. Rev. Lett.*, **99** (18), 4 (2007).

[44] F. Remacle, R. Kienberger, F. Krausz, and R. Levine. *Chem. Phys.*, **338** (2-3), 342 (2007).

[45] J. P. Marangos, S. Baker, N. Kajumba, J. S. Robinson, J. W. G. Tisch, and R. Torres. *Phys. Chem. Chem. Phys.*, **10** (1), 35 (2008).

[46] M. Lein, N. Hay, R. Velotta, J. Marangos, and P. Knight. *Phys. Rev. A: At. Mol. Opt. Phys.*, **66** (2), 023805 (2002).

[47] M. Lein, P. Corso, J. Marangos, and P. Knight. *Phys. Rev. A: At. Mol. Opt. Phys.*, **67** (2) (2003).

[48] A. Le, X. Tong, and C. Lin. *Phys. Rev. A: At. Mol. Opt. Phys.*, **73** (4), 041402 (2006).

[49] C. Vozzi, F. Calegari, E. Benedetti, J. Caumes, G. Sansone, S. Stagira, M. Nisoli, R. Torres, E. Heesel, N. Kajumba, J. Marangos, C. Altucci, and R. Velotta. *Phys. Rev. Lett.*, **95** (15), 153902 (2005).

[50] J. Itatani, J. Levesque, D. Zeidler, H. Niikura, H. Pepin, J. Kieffer, P. Corkum, and D. Villeneuve. *Nature*, **432** (7019), 867 (2004).

[51] W. Li, X. Zhou, R. Lock, S. Patchkovskii, A. Stolow, H. C. Kapteyn, and M. M. Murnane. *Science*, **322** (5905), 1207 (2008).

[52] N. L. Wagner, A. Wuest, I. P. Christov, T. Popmintchev, X. Zhou, M. M. Murnane, and H. C. Kapteyn. *Proc. Nat. Acad. Sci. U.S.A.*, **103** (36), 13279 (2006).

[53] Z. B. Walters, S. Tonzani, and C. H. Greene. *J. Phys. B: At. Mol. Opt. Phys.*, **40**, F277 (2007).

[54] M. Lein. *Phys. Rev. Lett.*, **94** (5), 053004 (2005).

[55] D. Strasser, T. Pfeifer, B. Hom, A. Müller, J. Plenge, and S. Leone. *Phys. Rev. A*, **73** (2), 1 (2006).

[56] I. V. Schweigert and S. Mukamel. *Phys. Rev. A: At. Mol. Opt. Phys.*, **76** (1), 1 (2007).

[57] Z. Li, D. Abramavicius, W. Zhuang, and S. Mukamel. *Chem. Phys.*, **341** (1-3), 29 (2007).

[58] I. V. Schweigert and S. Mukamel. *Phys. Rev. Lett.*, **99** (16), 1 (2007).

[59] D. M. Healion, I. V. Schweigert, and S. Mukamel. *J. Phys. Chem.. A*, **112** (45), 11449 (2008).

[60] A. A. Zholents and W. M. Fawley. *Phys. Rev. Lett.*, **92** (22) (2005).

[61] R. Schoenlein, S. Chattopadhyay, H. Chong, T. Glover, P. Heimann, C. Shank, A. Zholents, and M. Zolotorev. *Science*, **287** (5461), 2237 (2000).

[62] P. B. Corkum and F. Krausz. *Nat. Phys.*, **3** (6), 381 (2007).

[63] J. Breidbach and L. S. Cederbaum. *Phys. Rev. Lett.*, **94**, 033901 (2005).

[64] A. McPherson, G. Gibson, H. Jara, U. Johann, T. S. Luk, I. A. McIntyre, K. Boyer, and C. K. Rhodes. *J. Opt. Soc. Am. B: Opt. Phys.*, **4** (4), 595 (1987).

[65] M. Ferray, A. L'Huillier, X. F. Li, L. A. Lompre, G. Mainfray, and C. Manus. *J. Phys. B: At. Mol. Opt. Phys.*, **21** (3), L31 (1988).

[66] X. F. Li, A. L'Huillier, M. Ferray, L. A. Lompre, and G. Mainfray. *Phys. Rev. A: At. Mol. Opt. Phys.*, **39** (11), 5751 (1989).

[67] L. A. Lompre, A. L'Huillier, M. Ferray, P. Monot, G. Mainfray, and C. Manus. *J. Opt. Soc. Am. B: Opt. Phys.*, **7** (5), 754 (1990).

[68] A. L'Huillier, X. F. Li, and L. A. Lompré. *J. Opt. Soc. Am. B: Opt. Phys.*, **7** (4), 527 (1990).

[69] N. Sarukura, K. Hata, T. Adachi, R. Nodomi, M. Watanabe, and S. Watanabe. *Phys. Rev. A: At. Mol. Opt. Phys.*, **43** (3), 1669 (1991).

[70] P. Balcou, C. Cornaggia, A. S. L. Gomes, L. A. Lompre, and A. L'Huillier. *J. Phys. B: At. Mol. Opt. Phys.*, **25** (21), 4467 (1992).

[71] K. Miyazaki and H. Sakai. *J. Phys. B: At. Mol. Opt. Phys.*, **25** (3), L83 (1992).

[72] J. K. Crane, M. D. Perry, D. Strickland, S. Herman, and R. W. Falcone. *IEEE Trans. Plasma Sci.*, **21** (1), 82 (1993).

[73] J. H. Eberly, Q. Su, and J. Javanainen. *Phys. Rev. Lett.*, **62** (8), 881 (1989).

[74] K. C. Kulander and B. Shore. *Phys. Rev. Lett.*, **62** (5), 524 (1989).

[75] J. L. Krause, K. J. Schafer, and K. C. Kulander. *Phys. Rev. A: At. Mol. Opt. Phys.*, **45** (7), 4998 (1992).

[76] P. B. Corkum. *Phys. Rev. Lett.*, **71** (13), 1994 (1993).

[77] G. Farkas and C. Toth. *Phys. Lett. A*, **168** (5-6), 447 (1992).

[78] S. E. Harris, J. J. Macklin, and T. W. Haensch. *Opt. Commun.*, **100** (5-6), 487 (1993).

[79] M. Lewenstein, P. Balcou, M. Y. Ivanov, A. L'Huillier, and P. B. Corkum. *Phys. Rev. A: At. Mol. Opt. Phys.*, **49** (3), 2117 (1994).

[80] I. Mercer, E. Mevel, R. Zerne, A. LHuillier, P. Antoine, and C. Wahlstrom. *Phys. Rev. Lett.*, **77** (9), 1731 (1996).

[81] T. Ditmire, E. Gumbrell, R. A. Smith, J. W. G. Tisch, D. D. Meyerhofer, and M. H. R. Hutchinson. *Phys. Rev. Lett.*, **77** (23), 4756 (1996).

[82] T. Ditmire, J. W. G. Tisch, E. T. Gumbrell, R. A. Smith, D. D. Meyerhofer, and M. H. R. Hutchinson. *Appl. Phys. B*, **65** (3), 313 (1997).

[83] L. L. Deroff, P. Salieres, B. Carre, D. Joyeux, and D. Phalippou. *Phys. Rev. A: At. Mol. Opt. Phys.*, **61** (4), 043802 (2000).

[84] R. Bartels, A. Paul, H. Green, H. Kapteyn, M. Murnane, S. Backus, I. Christov, Y. Liu, D. Attwood, and C. Jacobsen. *Science*, **297** (5580), 376 (2002).

[85] D. G. Lee, J. J. Park, J. H. Sung, and C. H. Nam. *Opt. Lett.*, **28** (6), 480 (2003).

[86] R. Trebino. *Frequency Resolved Optical Gating: The Measurement of Ultrashort Laser Pulses*. Kluwer Academic Publishers, Boston (2000).

[87] C. Iaconis and I. A. Walmsley. *Opt. Lett.*, **23** (10), 792 794 (1998).

[88] T. Glover, R. Schoenlein, A. Chin, and C. Shank. *Phys. Rev. Lett.*, **76** (14), 2468 (1996).

[89] N. Papadogiannis, B. Witzel, C. Kalpouzos, and D. Charalambidis. *Phys. Rev. Lett.*, **83** (21), 4289 (1999).

[90] P. Paul, E. Toma, P. Breger, G. Mullot, F. Auge, P. Balcou, H. Muller, and P. Agostini. *Science*, **292** (5522), 1689 (2001).

[91] R. Kienberger, E. Goulielmakis, M. Uiberacker, A. Baltuska, V. Yakovlev, F. Bammer, A. Scrinzi, T. Westerwalbesloh, U. Kleineberg, U. Heinzmann, M. Drescher, and F. Krausz. *Nature*, **427** (6977), 817 (2004).

[92] H. R. Telle, G. Steinmeyer, A. E. Dunlop, J. Stenger, D. H. Sutter, and U. Keller. *Appl. Phys. B*, **69** (4), 327 (1999).

[93] T. Pfeifer, L. Gallmann, M. Abel, D. Neumark, and S. Leone. *Opt. Lett.*, **31** (7), 975 (2006).

[94] T. Pfeifer, L. Gallmann, M. J. Abel, D. M. Neumark, and S. R. Leone. *Opt. Lett.*, **31** (7), 975 977 (2006).

[95] T. Pfeifer, L. Gallmann, M. J. Abel, P. M. Nagel, D. M. Neumark, and S. R. Leone. *Phys. Rev. Lett.*, **97** (16), 163901 (2006).

[96] H. Merdji, T. Auguste, W. Boutu, J. P. Caumes, B. Carre, T. Pfeifer, A. Jullien, D. M. Neumark, and S. R. Leone. *Opt. Lett.*, **32** (21), 3134 (2007).

[97] K. S. Budil, P. Salieres, A. L'Huillier, T. Ditmire, and M. D. Perry. *Phys. Rev. A: At. Mol. Opt. Phys.*, **48** (5), R3437 (1993).

[98] G. Sansone, E. Benedetti, F. Calegari, C. Vozzi, L. Avaldi, R. Flammini, L. Poletto, P. Villoresi, C. Altucci, R. Velotta, S. Stagira, S. D. Silvestri, and M. Nisoli. *Science*, **314** (5798), 443 446 (2006).

[99] H. Mashiko, S. Gilbertson, C. Li, S. D. Khan, M. M. Shakya, E. Moon, and Z. Chang. *Phys. Rev. Lett.*, **100** (10), 103906 (2008).

[100] H. Mashiko, S. Gilbertson, C. Li, E. Moon, and Z. Chang. *Phys. Rev. A: At. Mol. Opt. Phys.*, **77** (6), 063423 (2008).

[101] A. Jullien, T. Pfeifer, M. J. Abel, P. M. Nagel, M. J. Bell, D. M. Neumark, and S. R. Leone. *Appl. Phys. B*, **93** (2-3), 433 (2008).

[102] T. Pfeifer, A. Jullien, M. J. Abel, P. M. Nagel, L. Gallmann, D. M. Neumark, and S. R. Leone. *Opt. Express*, **15** (25), 17120 (2007).

[103] M. J. Abel, T. Pfeifer, P. M. Nagel, W. Boutu, M. J. Bell, C. P. Steiner, D. M. Neumark, and S. R. Leone. *Chem. Phys.*, **366** (1-3), 9 (2009).

[104] K. Yamanouchi, A. Becker, R. Li, and S. L. Chin (editors). *Progress in Ultrafast Intense Laser Science IV*. Springer, Berlin (2008).

[105] K. Varju, Y. Mairesse, B. Carre, M. B. Gaarde, P. Johnsson, S. Kazamias, R. Lopez-Martens, J. Mauritsson, K. J. Schafer, P. H. Balcou, A. P. L'Huillier, and P. Salieres. *J. Mod. Optic.*, **52** (2-3), 379 (2005).

[106] R. Lopez-Martens, K. Varju, P. Johnsson, J. Mauritsson, Y. Mairesse, P. Salieres, M. B. Gaarde, K. J. Schafer, A. Persson, S. Svanberg, C. G. Wahlstrom, and A. P. L'Huillier. *Phys. Rev. Lett.*, **94** (3), 033001 (2005).

[107] K. Moribayashi, T. Kagawa, and D. E. Kim. *J. Phys. B: At. Mol. Opt. Phys.*, **38** (13), 2187 (2005).

[108] Y. Mairesse and F. Quéré. *Phys. Rev. A: At. Mol. Opt. Phys.*, **71** (1), 1 (2005).

[109] J. Gagnon, E. Goulielmakis, and V. S. Yakovlev. *Appl. Phys. B*, **92** (1), 25 (2008).

[110] J. Gagnon and V. S. Yakovlev. *Opt. Express*, **17** (20), 17678 (2009).

[111] M. J. Abel, T. Pfeifer, A. Jullien, P. M. Nagel, M. J. Bell, D. M. Neumark, and S. R. Leone. *J. Phys. B: At. Mol. Opt. Phys.*, **42** (7), 075601 (2009).

[112] A. Baltuska, M. Uiberacker, E. Goulielmakis, R. Kieberger, V. Yakolev, T. Udem, T. Hansch, and F. Krausz. *IEEE J. Sel. Top. Quantum Electron.*, **9** (4), 972 (2003).

[113] G. G. Paulus, F. Lindner, H. Walther, A. Baltuska, E. Goulielmakis, M. Lezius, and F. Krausz. *Phys. Rev. Lett.*, **91**, 253004 (2003).

[114] M. F. Kling, C. Siedschlag, A. J. Verhoef, J. I. Khan, M. Schultze, T. Uphues, Y. Ni, M. Uiberacker, M. Drescher, F. Krausz, and M. J. J. Vrakking. *Science*, **312** (5771), 246 (2006).

[115] P. A. Roos, X. Li, R. P. Smith, J. A. Pipis, T. M. Fortier, and S. T. Cundiff. *Opt. Lett.*, **30** (7), 735 (2005).

[116] D. J. Jones, S. A. Diddams, J. K. Ranka, A. Stentz, R. S. Windeler, J. L. Hall, and S. T. Cundiff. *Science*, **288** (5466), 635 (2000).

[117] U. Keller. *Nature*, **424**, 831 (2003).

[118] M. Zimmernann, C. Gohle, R. Holzwarth, T. Udem, and T. Hansch. *Opt. Lett.*, **29** (3), 310 (2004).

[119] S. Augst, D. D. Meyerhofer, D. Strickland, and S. L. Chin. *J. Opt. Soc. Am. B: Opt. Phys.*, **8** (4), 858 (1991).

[120] M. V. Ammosov, N. B. Delone, and V. P. Krainov. *Sov. Phys. JETP*, **64**, 1191 (1986).

[121] G. Saathoff, L. Miaja-Avila, M. Aeschlimann, M. M. Murnane, and H. C. Kapteyn. *Phys. Rev. A: At. Mol. Opt. Phys.*, **77** (2), 022903 (2008).

[122] G. L. Yudin and M. Y. Ivanov. *Phys. Rev. A: At. Mol. Opt. Phys.*, **64** (1) (2001).

[123] S. Adachi and T. Kobayashi. *Phys. Rev. Lett.*, **94** (15), 153903 (2005).

[124] A. Baltuska, T. Fuji, and T. Kobayashi. *Phys. Rev. Lett.*, **88** (13), 133901 (2002).

[125] T. Nakajima and S. Watanabe. *Phys. Rev. Lett.*, **96** (06), 213001 (2006).

[126] V. Roudnev and B. D. Esry. *Phys. Rev. Lett.*, **99** (22), 220406 (2007).

[127] M. F. Kling, J. Rauschenberger, A. J. Verhoef, E. Hasovic, T. Uphues, D. B. Milosevic, H. G. Muller, and M. J. J. Vrakking. *New J. Phys.*, **10** (2), 025024 (2008).

[128] R. Kienberger, E. Goulielmakis, M. Uiberacker, A. Baltuska, V. Yakovlev, F. Bammer, A. Scrinzi, T. Westerwalbesloh, U. Kleineberg, U. Heinzmann, M. Drescher, and F. Krausz. *Nature*, **427**, 817 (2004).

[129] A. T. J. B. Eppink and D. H. Parker. *Rev. Sci. Instrum.*, **68** (9), 3477 (1997).

[130] D. H. Parker and A. T. J. B. Eppink. *J. Chem. Phys.*, **107** (7), 2357 (1997).

[131] V. Drbinski, A. Ossadtchi, V. A. Mandelshtam, and H. Reisler. *Rev. Sci. Instrum.*, **73** (7), 2634 (2002).

[132] M. Wegener. *Extreme Nonlinear Optics*. Springer, New York (2005).

[133] M. Drescher, M. Hentschel, R. Kienberger, M. Uiberacker, V. Yakovlev, A. Scrinzi, T. Westerwalbesloh, U. Kleineberg, U. Heinzmann, and F. Krausz. *Nature*, **419**, 803 (2002).

[134] E. Cormier and P. Lambropolous. *Eur. Phys. J. D*, **2** (1), 15 (1998).

[135] T. Nakajima and E. Cormier. *Opt. Lett.*, **32** (19), 2879 (2007).

[136] D. Lappas and A. L'Huillier. *Phys. Rev. A: At. Mol. Opt. Phys.*, **58** (5), 4140 (1998).

[137] T. Pfeifer, L. Gallmann, M. J. Abel, P. M. Nagel, D. M. Neumark, and S. R. Leone. *Phys. Rev. Lett.*, **97** (16), 163901 (2006).

[138] H. Xiong, R. Li, Z. Zeng, Y. Zheng, Y. Peng, X. Yang, X. Chen, H. Zeng, and Z. Xu. *Phys. Rev. A: At. Mol. Opt. Phys.*, **75** (5), 051802 (2007).

[139] Y. Zheng, Z. Zeng, X. Li, X. Chen, P. Liu, H. Xiong, H. Lu, S. Zhao, P. Wei, L. Zhang, Z. Wang, J. Liu, Y. Cheng, R. Li, and Z. Xu. *Opt. Lett.*, **33** (3), 234 (2008).

[140] L. Zheng, S. Tang, and X. Chen. *Opt. Express*, **17** (2), 538 (2009).

[141] Z. Chang. *Phys. Rev. A: At. Mol. Opt. Phys.*, **71** (2), 023813 (2005).

[142] Z. Chang. *Phys. Rev. A: At. Mol. Opt. Phys.*, **76** (5), 051403 (2007).

[143] A. Paul, E. Gibson, X. Zhang, A. Lytle, T. Popmintchev, X. Zhou, M. Murnane, I. Christov, and H. Kapteyn. *IEEE J. Quantum Elect.*, **42** (1-2), 14 (2006).

[144] C. A. Haworth, L. E. Chipperfield, J. S. Robinson, P. L. Knight, J. P. Marangos, and J. W. G. Tisch. *Nat. Phys.*, **3** (1), 52 (2007).

[145] J. Reichert, R. Holzwarth, T. Udem, and T. Hänsch. *Opt. Commun.*, **172** (1-6), 59 (1999).

[146] M. Nisoli, S. D. Silvestri, and O. Svelto. *Appl. Phys. Lett.*, **68**, 2793 (1996).

[147] M. Nisoli, S. D. Silvestri, O. Svelto, R. Szipöcs, K. Ferencz, C. Spielmann, S. Sartania, and F. Krausz. *Opt. Lett.*, **22** (8), 522 (1997).

[148] L. Gallmann, T. Pfeifer, P. M. Nagel, M. J. Abel, D. M. Neumark, and S. R. Leone. *Appl. Phys. B*, **86** (4), 561 (2007).

[149] A. Baltuska, M. Uiberacker, E. Goulielmakis, R. Kienberger, V. Yakovlev, T. Udem, T. Hansch, and F. Krausz. *IEEE J. Sel. Top. Quantum Electron.*, **9** (4), 972 (2003).

[150] J. Krause, K. Schafer, and K. Kulander. *Phys. Rev. Lett.*, **68** (24), 3535 (1992).

[151] P. B. Corkum. *Phys. Rev. Lett.*, **71** (13), 1994, 1997 (1993).

[152] M. Lewenstein, P. Salières, and A. L'huillier. *Phys. Rev. A: At. Mol. Opt. Phys.*, **52** (6), 4747 (1995).

[153] Y. Mairesse, A. de Bohan, L. Frasinski, H. Merdji, L. Dinu, P. Monchicourt, P. Breger, M. Kovacev, T. Auguste, and B. Carré. *Phys. Rev. Lett.*, **93**, 163901 (2004).

[154] M. B. Gaarde, J. L. Tate, and K. J. Schafer. *J. Phys. B: At. Mol. Opt. Phys.*, **41** (13), 132001 (2008).

[155] I. Thomann, A. Bahabad, X. Liu, R. Trebino, M. Murnane, and H. Kapteyn. *Opt. Express*, **17** (6), 4611 (2009).